

Light-induced Charge Carrier Dynamics in Metal Halide Perovskites

Guo, Dengyang

DOI

[10.4233/uuid:5d91d546-2b0b-401a-ac9a-de7dc60dd22d](https://doi.org/10.4233/uuid:5d91d546-2b0b-401a-ac9a-de7dc60dd22d)

Publication date

2019

Document Version

Final published version

Citation (APA)

Guo, D. (2019). *Light-induced Charge Carrier Dynamics in Metal Halide Perovskites*. [Dissertation (TU Delft), Delft University of Technology]. <https://doi.org/10.4233/uuid:5d91d546-2b0b-401a-ac9a-de7dc60dd22d>

Important note

To cite this publication, please use the final published version (if applicable).
Please check the document version above.

Copyright

Other than for strictly personal use, it is not permitted to download, forward or distribute the text or part of it, without the consent of the author(s) and/or copyright holder(s), unless the work is under an open content license such as Creative Commons.

Takedown policy

Please contact us and provide details if you believe this document breaches copyrights.
We will remove access to the work immediately and investigate your claim.

Light-induced Charge Carrier Dynamics in Metal Halide Perovskites



Dengyang Guo

Light-induced Charge Carrier Dynamics in Metal Halide Perovskites

Dissertation

for the purpose of obtaining the degree of doctor

at Delft University of Technology

by the authority of the Rector Magnificus, Prof.dr.ir. T.H.J.J. van der Hagen

chair of the Board for Doctorates

to be defended publicly on

Tuesday 8 October 2019 at 12:30 o'clock

by

Dengyang GUO

Master of Science in Condensed Matter Physics,

Chinese Academy of Sciences, China

born in Shanxi, China

This dissertation has been approved by the promoters:

Dr.ir. T.J. Savenije

Dr. A.J. Houtepen

Composition of the doctoral committee:

Rector Magnificus,	chairperson
Dr.ir. T.J. Savenije	Delft University of Technology, promotor
Dr. A.J. Houtepen	Delft University of Technology, promotor

Independent members:

Dr. B. Ehrler	AMOLF, Research Inst.
Prof.dr. M.A. Loi	RU Groningen
Prof.dr.ir. A.H.M. Smets	Delft University of Technology
Prof. dr. F.M. Mulder	Delft University of Technology

This work was financed by the China Scholarship Council (CSC).



ISBN/EAN: 978-94-028-1733-1

Copyright © 2019 Dengyang Guo

Cover by the author

Printed by Ipskamp Printing, Enschede, the Netherlands

An electronic version of this thesis is freely available at <http://repository.tudelft.nl>

It doesn't matter if a cat is black or white, as long as it catches mice.

Deng Xiaoping

Table of Contents

Chapter 1	Introduction	1
Chapter 2	Comparing the Calculated Fermi Level Splitting with the Open-Circuit Voltage in Various Perovskite Cells	15
Chapter 3	Reversible Removal of Intermixed Shallow States by Light Soaking Multi-Cation Mixed Halide Perovskite Films	43
Chapter 4	Photoluminescence from Radiative Surface States and Excitons in Methylammonium Lead Bromide Perovskites	77
Chapter 5	Sub-Bandgap Absorption in Hybrid Lead Halide Perovskites Comprises Non-linear Two-Photon Absorption and Linear sub-bandgap Absorption	105
	Summary	125
	Samenvatting	127
	Acknowledgement	131
	Curriculum Vitae	133
	List of publications	135

Chapter 1 Introduction

Over the past decade, both global photovoltaic production and installation have globally increased exponentially. The largest contribution is from Si-wafer based photovoltaics.¹ At present, the cost of electricity from Si photovoltaics, amounting to 0.1-0.36 USD/kWh is similar to that of the traditional energy sources such as burning fossil fuels.² Nevertheless, even for the best commercial crystalline Si photovoltaics the energy payback time is at least two years. The production of the Si wafers requires about 70% of the total energy input.¹ Aiming at high efficiency and low energy consumption for the production of photovoltaics, new materials and technologies are studied to replace Si such as CdTe, CIGS et al. Among these novel absorber materials, perovskite based solar cells have shown the fastest efficiency growth in the photovoltaic research history, increasing from 3.8% to up-to-date 24.2% within a decade.³ Such high efficiency has already out competed that of multi-crystalline Si and CIGS and is approaching that of mono-Si.³ Moreover, the current cost of perovskite panels is estimated to be 3 to 8 times less than that of Si panels.⁴ Therefore, perovskites are promising materials for producing high efficiency and low-cost photovoltaics.

1.1 What are perovskites?

Perovskites are a group of materials sharing the same crystal structure shown in **Figure 1.1**. The general formula is given by ABX_3 .⁵ In the centre of the crystal structure is cation A, which can be e.g. methylammonium (MA: $CH_3NH_3^+$), formamidinium (FA: $CH_2(NH_2)_2^+$) or caesium (Cs^+). The 8 corners of the cubic structure are taken by cation B, which is Pb^{2+} for the currently most successful perovskite in terms of solar cell efficiency. Each cation B is surrounded by an octahedral cage consisting of 6 halides, e.g. iodide (I^-) bromide (Br^-) or chloride (Cl^-). Figure 1.1 (a) shows the composition of the perovskite, methylammonium lead iodide ($MAPbI_3$ or in short MAPI) used in the first perovskite based solar cell.^{6,7} The orbital diagram of MAPI is

Chapter 1

shown in Figure 1.1 (b). According to DFT calculations, the lowest unoccupied states of the conduction band are formed by the Pb 6p-I 5p π -antibonding and Pb 6p-I 5s σ -antibonding orbitals, while the highest states in the valence band are formed by of Pb 6s-I 5p σ -antibonding orbitals.^{8,9} However, considering the energy levels, the majority of the conduction band is built up from Pb orbitals, while for the valence band both Pb and I orbitals are important.¹⁰ Therefore, changing the halide from I to Br or Cl leads to a substantial difference in the bandgap since in particular the position of valence band maximum changes.¹¹

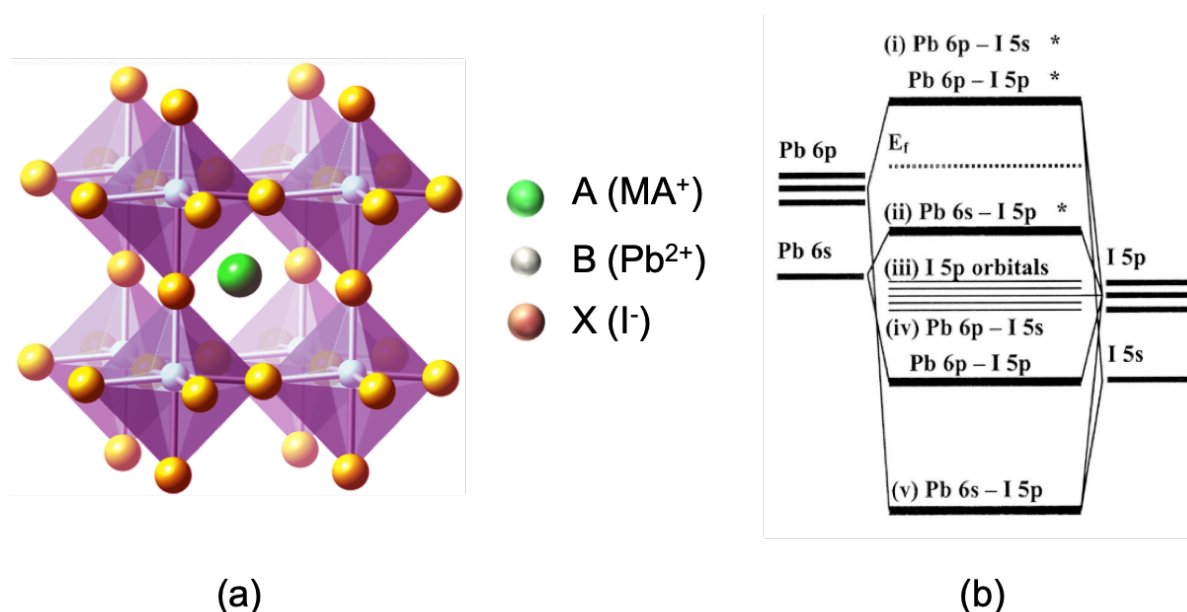


Figure 1.1 (a) Schematic crystal structure of perovskites, (b) Orbital diagram of MAPI, from Ref.⁸

1.2 Perovskite solar cells

The first metal halide perovskite (MHP) solar cell was introduced in a dye-sensitized solar cell architecture, which contains a mesoporous layer, as shown in **Figure 1.2** (a). This mesoporous titanium dioxide layer was expected to facilitate the electron extraction.¹² The required thickness of the perovskite layer to absorb the major part of the incident visible light is just a few hundreds of nanometres, which can be attributed to the high absorption coefficient of MHPs.⁵ This thin layer thickness is one of the merits of MHPs, especially in comparison with Si, which requires a thickness of at least 200 micrometres for full light absorption.¹

The structure of MHP solar cells can be either $n-i-p$ or $p-i-n$, where n and p represent n -type and p -type materials, respectively as shown in Figure 1.2.¹² The sequence ($n-i-p$ or $p-i-n$) is determined by the transport layer facing the incident illumination. These contact layers selectively transport electrons or holes, and are therefore also denoted as electron transport material (ETM) or hole transport material (HTM).

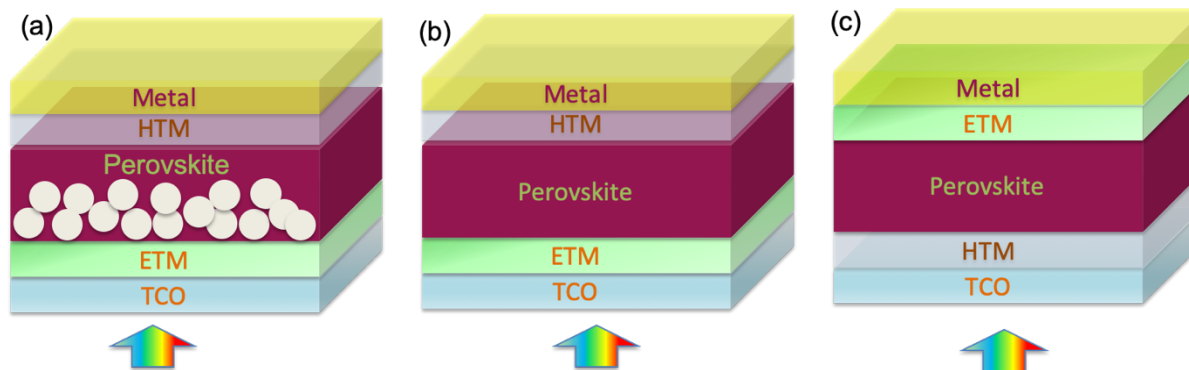


Figure 1.2 Structure of various perovskite solar cells. (a) mesoporous $n-i-p$ (b) planar $n-i-p$ (c) planar $p-i-n$.
TCO: transparent conducting oxide film.

The perovskites layers, as well as transport materials can be deposited from wet chemical processes including spin-coating or alternatively by thermal evaporation of the precursors.¹³ Over the last 5 years many MHP solar cells have been studied with hundreds of different HTMs and dozens of ETMs.^{14,15} The up-to-date published highest records are based on mixed cation and mixed halide perovskites¹⁶, *i.e.* (FA,MA,Cs)Pb(I,Br)₃.¹⁷

1.3 Opto-electronic properties of perovskites

For an efficient solar cell, the opto-electronic properties of MHPs are of prime importance. The charge carrier mobilities in MHPs are, however, two orders of magnitude lower than that in GaAs.¹⁸ Fortunately, the diffusion length of the charge carriers in MHPs is reported to be still much longer than the required thickness of the absorber layer of hundreds of nanometres.¹⁹ This long diffusion length can be attributed to the relatively long charge carrier lifetime, which is apart from the mobility determined by the recombination rate between opposite carriers and charge carrier trapping. Recombination of carriers can be classified into three types: first-order recombination (Shockley-Read-Hall), second-order recombination (band-to-band), and third-order recombination (Auger). The latter involves the presence of three carriers. Under one sun

Chapter 1

illumination (AM1.5), the charge carrier density is relatively low and therefore Auger recombination is negligible for MHPs as demonstrated by experimental and theoretical studies.^{20,21} Hence, since we limit our research to materials for solar cell applications, Auger recombination is not addressed in this thesis.

Second-order band-to-band recombination in semiconductors occurs by the decay of a CB electron and a VB hole. This type of recombination plays an important role in direct bandgap semiconductors under solar illumination. Since the band-to-band recombination is the reverse process of absorption in a direct-bandgap semiconductor, the band-to-band recombination rate is a constant, intrinsic property of the material. However, in practice, the effective value of the rate might be different due to additional non-radiative bimolecular processes.^{22,23}

First-order recombination is typically mediated by impurities or defects in the semiconductor. Those defects lead to energy states within the forbidden bandgap, forming trap states, which can capture charge carriers and act as recombination centers.²⁴ Under low injection conditions, trap-assisted recombination is described by the Shockley-Read-Hall theory, in which capture of both electrons and holes are involved. In practice, the trap-related processes can be simplified by a net trapping process of electrons in a p-type semiconductor shown in Figure 1.3.

Above discussed types of recombination are standard processes for excess carriers in semiconductors under illumination. For some of the MHPs studied in this thesis, additional decay pathways induced by structural heterogeneity or surface states need to be taken into account. As presented in Chapter 3, intermixed distributions of halides lead to shallow states and to a charge diffusional imbalance in (FA,MA,Cs)Pb(I,Br)₃ films; In Chapter 4, surface recombination is shown to dominate the decay of photon-excited free charge carriers in MAPbBr₃ single crystals.

To study the kinetics of charge carriers in MHPs, time-resolved techniques are used such as time-resolved PL (TRPL),¹⁹ time-resolved microwave photoconductivity (TRMC),²⁵ optical-pump-THz-probe photoconductivity (THzC),²⁶ or transient absorption (TA).²² TRPL relies on radiative recombination of opposite charge carriers, and thus charge carriers decaying by non-radiative recombination cannot be directly measured. The other three techniques can monitor

the concentration of charge carriers as a function of time no matter whether they recombine radiatively or non-radiatively. Therefore, a combination of TRPL with one of the other three techniques is very useful to monitor the kinetics of photo-excited free charge carriers.^{22,25,26} In this thesis we will mainly use combinations of TRPL and TRMC. The latter has been previously described, has the advantage that also the charge carrier mobilities can be obtained.^{23,25}

To extract kinetic parameters from time-resolved measurements, a general approach is fitting the time-resolved traces by a polynomial equation:

$$\frac{dn}{dt} = -k_1n - k_2n^2 - k_3n^3 \quad (11)$$

In this equation, all three types of recombination mentioned in section 1.3 are included. However, since the three recombination types dominate in different but overlaying carrier density regimes, revealing a precise set of all three rates by fitting via Equation (11) requires a wide range of excitation densities.²⁷

In 2015, Hutter *et al.* reported a versatile model to describe the charge carrier dynamics in MAPI. The same set of kinetic parameters from the model was shown to fit the recombination behaviour measured by both TRMC and TRPL. Since then, this model was successfully applied for a range of MHPs not only including MAPI^{23,25,28,29} but also mixed MHPs,^{17,30} inorganic MHPs,³¹ and lead-free perovskites.³² In this model, each arrow represents a specific process and thus a term in the differential equations describing the time-dependent concentration of excess carriers, as will be discussed in Chapters 2 and 3.

Chapter 1

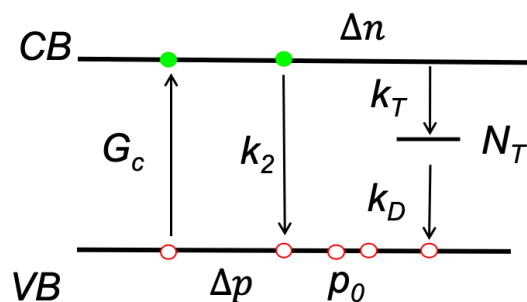


Figure 1.3 Diagram of the used kinetic model. This model includes the second-order process with rate k_2 and first-order process with trapping and trap depopulation rates k_T and k_D . (see for more details Chapter 2)

1.4 Photovoltaic performance

As like other semiconductor single-absorber solar cells, the ultimate limit of a perovskite solar cell can be obtained by the Shockley-Queisser limit, which considers inevitable losses including spectral mismatch and thermal radiation at a non-zero temperature.³³ The spectral mismatch comprises a fraction of the photons of the sunlight with energies below the bandgap that cannot be absorbed. Another contribution is from those photons that have excess energy which is released as heat into the lattice, denoted as thermal relaxation. As a result, the efficiency limit is around 30.7% for MAPI with a bandgap of 1.58 eV.³³

The standard equation to calculate the efficiency of a solar cell from a J/V curve is expressed as:

$$\eta = \frac{J_{sc}V_{oc}FF}{P_{in}} \quad (1)$$

where J_{sc} is the short circuit current density, V_{oc} is the open circuit voltage, FF is the fill factor and P_{in} is the standard power input from the sunlight (AM1.5: one sun at a zenith angle of 48.2°).²⁴ The maximum value of J_{sc} can be derived from the total photon flux from the sunlight and the optical absorption and reflection.¹² The maximum value of V_{oc} is determined by the Shockley-Queisser limit.³⁴ While the V_{oc} of MHP solar cells is still below the theoretical value, that of GaAs solar cells has almost reached the limit.¹² Therefore, improving the V_{oc} towards

the Shockley-Queisser limit is important to improve the efficiency of perovskite solar cells further.

A semiconductor is characterised by a forbidden bandgap with energies between 1 to 3 eV between the conduction band minimum (CB) and valance band maximum (VB). The density of allowed energy states in these bands is a function of the energy. The electron distribution over these states follows the Fermi-Dirac distribution function. The equilibrium concentration of CB electrons, n_0 and VB holes, p_0 are given by:

$$n_0 = n_i e^{\frac{E_F - E_{Fi}}{kT}} \quad (2)$$

$$p_0 = n_i e^{-\frac{E_F - E_{Fi}}{kT}} \quad (3)$$

where n_i is the intrinsic carrier concentration, E_F and E_{Fi} represent the Fermi energy and intrinsic Fermi energy, respectively. For non-doped semiconductors, $E_F = E_{Fi}$ thus $n_0 = p_0 = n_i$.

Under illumination, excess carriers are generated in the semiconductor. The Quasi-Fermi levels for electrons, E_{Fn} and holes, E_{Fp} designate the excess concentrations, Δn and Δp .²⁴

$$n_0 + \Delta n = n_i e^{\frac{E_{Fn} - E_{Fi}}{kT}} \quad (4)$$

$$p_0 + \Delta p = n_i e^{-\frac{E_{Fp} - E_{Fi}}{kT}} \quad (5)$$

By combining Equation (4) and (5), we obtain

$$E_{Fn} - E_{Fp} = kT \ln \frac{(n_0 + \Delta n)(p_0 + \Delta p)}{n_i^2} \quad (6)$$

This energy difference is the so-called Quasi-Fermi level splitting, μ_F and quantifies the ultimate V_{oc} value of a $p-i-n$ or $n-i-p$ solar cell. If there are no additional losses, μ_F can be calculated by the Shockley-Queisser detailed balance.³³ In practice, due to losses from non-radiative recombination, the value of μ_F is lower and thus limiting the V_{oc} .

When a voltage is applied over a photo-active junction, the current in the dark is given by the diode equation containing a Boltzmann term:

Chapter 1

$$J = J_0 e^{\frac{qV}{kT}} - J_0 \quad (7)$$

Where J_0 is the saturation current density.²⁴ Under illumination and open circuit conditions, the total current $J = J_{sc} - (J_0 e^{\frac{qV_{oc}}{kT}} - J_0) = 0$. Then,

$$V_{oc} = \frac{kT}{e} \ln \left(\frac{J_{sc}}{J_0} + 1 \right) \quad (8)$$

where J_{sc} is the short circuit current density. However, in a non-ideal cell there are additional losses of charge carriers apart from radiative recombination. This means that not all photons which are theoretically absorbed by the semiconductor contribute to the build-up of the V_{oc} . Therefore, an external quantum efficiency (EQE) is introduced leading to:³⁵

$$V_{oc} = \frac{kT}{e} \ln \left(EQE \frac{J_{sc}}{J_0} + 1 \right) \quad (9)$$

Which can be converted into:³⁶

$$V_{oc} \cong \frac{kT}{e} \ln \left(EQE \frac{J_{sc}}{J_0} \right) = V_{oc}^{SQ} + \frac{kT}{e} \ln (EQE) \quad (10)$$

Here, V_{oc}^{SQ} stands for the maximum value determined by the bandgap, solar spectrum and thermal radiation, *i.e.* the Shockley-Queisser limit and hence, V_{oc}^{SQ} can be calculated.³⁶ The last term quantifies the non-radiative losses and is used for direct and quantitative comparison between different solar cells.

From Equation (10), one can directly see that a high EQE leads to a high V_{oc} . The EQE can be measured by e.g. determining the electroluminescence quantum efficiency, EQE_{EL} . The factors that affect the EQE_{EL} are included in Equation (11):

$$EQE_{EL} = \frac{p_e IQE}{1 - IQE[1 - p_e - p_a]} \quad (11)$$

Here, p_a stands for the parasitical loss of emitted photons by the contact layers, p_e is the outcoupling efficiency, and IQE stands for internal luminescence quantum yield, which is the fraction of free charge carrier that decays radiatively.³⁸

For ideal contacts p_a is close to 0, which leads to,

$$EQE_{EL} = \frac{p_e IQE}{1 - IQE[1 - p_e]} = EQE_{PL} \quad (12)$$

In this case, the photoluminescence quantum efficiency, EQE_{PL} can also be used for Equation (10).^{22,23,37} Equation (12) shows that internal material properties can be related to external device parameters like to V_{oc} . In chapter 2 an alternative method for obtaining the V_{oc} is provided.

1.5 Thesis outline

While perovskites are intensively investigated for application in solar cells and other optoelectronic devices, fundamental research has contributed to reveal the intrinsic properties of this group of interesting materials. This thesis intends to show the relationship between the material properties, charge carrier dynamics and the performance of devices.

In **Chapter 2** TRMC traces are fitted via the kinetic model mentioned above, and the found rate constants are used to calculate the concentrations of charge carriers under steady state conditions. From these concentrations, the μ_F in the perovskite layer is determined and compared with the actual V_{oc} . Such comparison not only proves that the kinetic model reflects the actual charge carrier dynamics properly but also offers a versatile way to select which techniques and transport layers could be beneficial to improve the efficiency of perovskite solar cells.

The highest reported efficiencies of metal halide perovskite (MHP) solar cells are all based on mixed cation, mixed halide perovskites, such as $(FA,MA,Cs)Pb(I_{1-x}Br_x)_3$ ($x = 0 - 1$). In **Chapter 3**, various $(FA,MA,Cs)Pb(I_{1-x}Br_x)_3$ perovskite films are light-soaked in nitrogen and the change in properties are investigated by time-resolved microwave conductivity, optical and structural techniques. For this class of MHP apart from band-to-band recombination, and trap mediated decay, additional shallow states have to be included to describe the charge carrier dynamics properly.

Methylammonium lead bromide ($MAPbBr_3$) is a possible candidate to serve as a light absorber in a subcell of a multi-junction solar cell. In **Chapter 4** complementary temperature-dependent time-resolved microwave conductance and photoluminescence measurements, shows that the exciton yield increases with lower temperatures at the expense of the charge carrier generation

Chapter 1

yield. The low energy emission at around 580 nm in the cubic phase and the second broad emission peak at 622 nm in the orthorhombic phase originate from radiative recombination of charges trapped in defects with mobile counter charges. Knowledge of surface defects is of interest to reach higher open-circuit voltages in MAPbBr₃ based solar cells.

There has been intense research into the optoelectronic properties of perovskites, however, the sub-bandgap absorption in MHPs remains largely un-explored. In **Chapter 5** we recorded two photon absorption (2PA) spectra of polycrystalline MHP thin films using the time-resolved microwave conductivity technique over a wide wavelength regime. The 2PA coefficients, β have been calculated by taken into account the quadratic relationship between the number of induced charge carriers and the incident light intensity. These results give insight into the band structure of MHPs.

References

- (1) Philipps, S. *Photovoltaics Report, Updated: 27 August 2018*; 2018.
- (2) Renewable Energy Agency, I. *Renewable Power Generation Costs in 2017 ACKNOWLEDGEMENTS*; 2018.
- (3) NREL. Research Cell Efficiency Records, National Center for Photovoltaics http://www.nrel.gov/ncpv/images/efficiency_chart.jpg (accessed Jul 17, 2018).
- (4) Peter Diamandis. Disrupting Solar <https://medium.com/@PeterDiamandis/disrupting-solar-faf6a110b0a4> (accessed Feb 18, 2019).
- (5) Green, M. A.; Ho-Baillie, A.; Snaith, H. J. The Emergence of Perovskite Solar Cells. *Nat. Photonics* **2014**, *8*, 506–514.
- (6) Kojima, A.; Teshima, K.; Shirai, Y.; Miyasaka, T. Organometal Halide Perovskites as Visible-Light Sensitizers for Photovoltaic Cells. *J. Am. Chem. Soc.* **2009**, *131*, 6050–6051.
- (7) Lee, M. M.; Teuscher, J.; Miyasaka, T.; Murakami, T. N.; Snaith, H. J. Efficient

- Hybrid Solar Cells Based on Meso-Superstructured Organometal Halide Perovskites. *Science*. **2012**, *338*, 643–647.
- (8) Umebayashi, T.; Asai, K. Electronic Structures of Lead Iodide Based Low-Dimensional Crystals. **2003**, 2–7.
- (9) Wang, H.; Liu, Y.; Li, M.; Huang, H.; Xu, H. M.; Hong, R. J.; Shen, H. Halide Perovskite Materials for Solar Cells: A Theoretical Review. *J. Mater. Chem. A* **2015**, *4*, 1166–1169.
- (10) Brivio, F.; Walker, A. B.; Walsh, A. Structural and Electronic Properties of Hybrid Perovskites for High-Efficiency Thin-Film Photovoltaics from First-Principles. *APL Mater.* **2013**, *1*.
- (11) Jesper Jacobsson, T.; Correa-Baena, J.-P.; Pazoki, M.; Saliba, M.; Schenk, K.; Grätzel, M.; Hagfeldt, A. Exploration of the Compositional Space for Mixed Lead Halogen Perovskites for High Efficiency Solar Cells. *Energy Environ. Sci.* **2016**, *9*, 1706–1724.
- (12) Park, N.; Segawa, H. Research Direction toward Theoretical Efficiency in Perovskite Solar Cells. *ACS Photonics* **2018**, *5*, 2970–2977.
- (13) Hutter, E. M.; Gélvez-Rueda, M. C.; Osherov, A.; Bulović, V.; Grozema, F. C.; Stranks, S. D.; Savenije, T. J. Direct-Indirect Character of the Bandgap in Methylammonium Lead Iodide Perovskite. *Nat. Mater.* **2017**, *16*, 115–120.
- (14) Calió, L.; Kazim, S.; Grätzel, M.; Ahmad, S. Hole-Transport Materials for Perovskite Solar Cells. *Angew. Chemie - Int. Ed.* **2016**, *55*, 14522–14545.
- (15) Yang, G.; Tao, H.; Qin, P.; Ke, W.; Fang, G. Recent Progress in Electron Transport Layers for Efficient Perovskite Solar Cells. *J. Mater. Chem. A* **2016**, *4*, 3970–3990.
- (16) Ono, L. K.; Juarez-Perez, E. J.; Qi, Y. Progress on Perovskite Materials and Solar Cells with Mixed Cations and Halide Anions. *ACS Appl. Mater. Interfaces* **2017**, *9*, 30197–30246.
- (17) Abdi-Jalebi, M.; Andaji-Garmaroudi, Z.; Cacovich, S.; Stavrakas, C.; Philippe, B.; Richter, J. M.; Alsari, M.; Booker, E. P.; Hutter, E. M.; Pearson, A. J.; et al.

Chapter 1

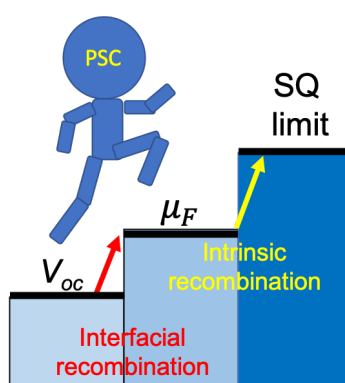
- Maximizing and Stabilizing Luminescence from Halide Perovskites with Potassium Passivation. *Nature* **2018**, *555*, 497–501.
- (18) Herz, L. M. Charge-Carrier Mobilities in Metal Halide Perovskites: Fundamental Mechanisms and Limits. *ACS Energy Lett.* **2017**, *2*, 1539–1548.
- (19) Stranks, S. D.; Eperon, G. E.; Grancini, G.; Menelaou, C.; Alcocer, M. J. P.; Leijtens, T.; Herz, L. M.; Petrozza, A.; Snaith, H. J. Electron-Hole Diffusion Lengths Exceeding 1 Micrometer in an Organometal Trihalide Perovskite Absorber. *Science*. **2013**, *342*, 341–344.
- (20) Milot, R. L.; Eperon, G. E.; Snaith, H. J.; Johnston, M. B.; Herz, L. M. Temperature-Dependent Charge-Carrier Dynamics in CH₃NH₃PbI₃ Perovskite Thin Films. *Adv. Funct. Mater.* **2015**, *25*, 6218–6227.
- (21) Shen, J. X.; Zhang, X.; Das, S.; Kioupakis, E.; Van de Walle, C. G.; Walle, C. G. Van De. Unexpectedly Strong Auger Recombination in Halide Perovskites. *Adv. Energy Mater.* **2018**, *8*, 1–7.
- (22) Richter, J. M.; Abdi-Jalebi, M.; Sadhanala, A.; Tabachnyk, M.; Rivett, J. P. H.; Pazos-Outón, L. M.; Gödel, K. C.; Price, M.; Deschler, F.; Friend, R. H. Enhancing Photoluminescence Yields in Lead Halide Perovskites by Photon Recycling and Light Out-Coupling. *Nat. Commun.* **2016**, *7*.
- (23) Brenes, R.; Guo, D.; Osherov, A.; Noel, N. K.; Eames, C.; Hutter, E. M.; Pathak, S. K.; Niroui, F.; Friend, R. H.; Islam, M. S.; et al. Metal Halide Perovskite Polycrystalline Films Exhibiting Properties of Single Crystals. *Joule* **2017**, *1*, 155–167.
- (24) Neamen, D. A. *Semiconductor Physics & Devices: Basic Principles*, Fourth Edi.; McGraw-Hill Education: New York, NY 10121, 2012.
- (25) Hutter, E. M.; Eperon, G. E.; Stranks, S. D.; Savenije, T. J. Charge Carriers in Planar and Meso-Structured Organic-Inorganic Perovskites: Mobilities, Lifetimes, and Concentrations of Trap States. *J. Phys. Chem. Lett.* **2015**, *6*, 3082–3090.
- (26) Milot, R. L.; Eperon, G. E.; Snaith, H. J.; Johnston, M. B.; Herz, L. M. Temperature-

- Dependent Charge-Carrier Dynamics in $\text{CH}_3\text{NH}_3\text{PbI}_3$ Perovskite Thin Films. *Adv. Funct. Mater.* **2015**, *25*, 6218–6227.
- (27) Levine, I.; Gupta, S.; Bera, A.; Ceratti, D.; Hodes, G.; Cahen, D.; Guo, D.; Savenije, T. J.; Ávila, J.; Bolink, H. J.; et al. Can We Use Time-Resolved Measurements to Get Steady-State Transport Data for Halide Perovskites? *J. Appl. Phys.* **2018**, *124*.
- (28) Momblona, C.; Gil-Escrig, L.; Bandiello, E.; Hutter, E. M.; Sessolo, M.; Lederer, K.; Blochwitz-Nimoth, J.; Bolink, H. J. Efficient Vacuum Deposited P-i-n and n-i-p Perovskite Solar Cells Employing Doped Charge Transport Layers. *Energy Environ. Sci.* **2016**, *9*, 3456–3463.
- (29) Pérez-del-Rey, D.; Forgács, D.; Hutter, E. M.; Savenije, T. J.; Nordlund, D.; Schulz, P.; Berry, J. J.; Sessolo, M.; Bolink, H. J. Strontium Insertion in Methylammonium Lead Iodide: Long Charge Carrier Lifetime and High Fill-Factor Solar Cells. *Adv. Mater.* **2016**, *28*, 9839–9845.
- (30) Hu, Y.; Hutter, E. M.; Rieder, P.; Grill, I.; Hanisch, J.; Aygüler, M. F.; Hufnagel, A. G.; Handloser, M.; Bein, T.; Hartschuh, A.; et al. Understanding the Role of Cesium and Rubidium Additives in Perovskite Solar Cells: Trap States, Charge Transport, and Recombination. *Adv. Energy Mater.* **2018**, *1703057*, 1703057.
- (31) Chandrashekar, S.; Abdi-Jalebi, M.; Sutton, R. J.; Hutter, E. M.; Savenije, T. J.; Stranks, S. D.; Snaith, H. J. Vapour-Deposited Cesium Lead Iodide Perovskites: Microsecond Charge Carrier Lifetimes and Enhanced Photovoltaic Performance. *ACS Energy Lett.* **2017**, *2*, 1901–1908.
- (32) Hutter, E. M.; Gélvez-Rueda, M. C.; Bartesaghi, D.; Grozema, F. C.; Savenije, T. J. Band-Like Charge Transport in $\text{Cs}_2\text{AgBiBr}_6$ and Mixed Antimony-Bismuth $\text{Cs}_2\text{AgBi}_{1-x}\text{Sb}_x\text{Br}_6$ Halide Double Perovskites. *ACS Omega* **2018**, *3*, 11655–11662.
- (33) Shockley, W.; Queisser, H. J. Detailed Balance Limit of Efficiency of P-n Junction Solar Cells. *J. Appl. Phys.* **1961**, *32*, 510–519.
- (34) Sha, W. E. I.; Ren, X.; Chen, L.; Choy, W. C. H. The Efficiency Limit of $\text{CH}_3\text{NH}_3\text{PbI}_3$ Perovskite Solar Cells. *Appl. Phys. Lett.* **2015**, *106*, 221104.

Chapter 1

- (35) Tress, W.; Marinova, N.; Inganäs, O.; Nazeeruddin, M. K.; Zakeeruddin, S. M.; Graetzel, M. Predicting the Open-Circuit Voltage of $\text{CH}_3\text{NH}_3\text{PbI}_3$ Perovskite Solar Cells Using Electroluminescence and Photovoltaic Quantum Efficiency Spectra: The Role of Radiative and Non-Radiative Recombination. *Adv. Energy Mater.* **2015**, *5*, 1400812.
- (36) Rau, U.; Blank, B.; Müller, T. C. M. M.; Kirchartz, T. Efficiency Potential of Photovoltaic Materials and Devices Unveiled by Detailed-Balance Analysis. *Phys. Rev. Appl.* **2017**, *7*, 44016.
- (37) Stranks, S. D.; Hoyer, R. L. Z.; Di, D.; Friend, R. H.; Deschler, F. The Physics of Light Emission in Halide Perovskite Devices. **2018**, *1803336*, 1–11.
- (38) Paetzold, U. W.; Hebig, J.-C.; Mock, J.; Kirchartz, T.; Hempel, H.; Staub, F.; Unold, T.; Rau, U. Beyond Bulk Lifetimes: Insights into Lead Halide Perovskite Films from Time-Resolved Photoluminescence. *Phys. Rev. Appl.* **2016**, *6*, 1–13.

Chapter 2 Comparing the Calculated Fermi Level Splitting with the Open Circuit Voltage in Various Perovskite Cells



This part has been published:

Guo, D.; Caselli, V.; Hutter, E. M.; Savenije, T. J. Comparing the Calculated Fermi Level Splitting with the Open Circuit Voltage in Various Perovskite Cells. *ACS Energy Lett.* **2019**, *4*, 855–860.

Chapter 2

ABSTRACT

While the power conversion efficiency of metal halide perovskite (MHP) solar cells has increased enormously, the open circuit voltage V_{oc} , is still below the conceivable limit. Here, we derive the Fermi-level splitting, μ_F for various types of non-contacted MHPs, which sets a limit for their achievable V_{oc} , using rate constants and mobilities obtained from time-resolved photoconductivity measurements. Interestingly, we find that for vacuum-evaporated MAPbI₃ and K⁺-doped (MA,FA,Cs)Pb(I/Br)₃, the μ_F/e values are close to the reported V_{oc} values. This implies that for an improvement of the V_{oc} , charge carrier recombination within the bare perovskite has to be reduced. On the other hand, for MHPs with Cs⁺ and/or Rb⁺ addition, the experimental V_{oc} is still below μ_F/e , suggesting that higher voltages are feasible by optimizing the transport layers. The presented approach will help to select which techniques and transport layers are beneficial to improve the efficiency of MHP solar cells.

INTRODUCTION

Since their first introduction in 2009,¹ perovskite solar cells (PSCs) have shown an unprecedented rise in energy conversion efficiency, surpassing that of CIGS and approaching the value of crystalline silicon solar cells.² Different optimisation approaches including bandgap utilisation,^{3,4} light management,^{5,6} interface engineering,⁷⁻⁹ and transport material optimisation,¹⁰⁻¹² have been used to improve the efficiency. Subsequently, the open circuit voltage, V_{oc} , of PSCs has increased from 0.61 V¹ to over 1.2 V¹³⁻¹⁶. However, this value is still below the V_{oc} determined by the bandgap and thermal radiation or so-called entropy losses (1.33 V for MAPbI₃).¹⁷⁻¹⁹ Hence, understanding the factors governing the V_{oc} and developing methodologies to improve this are essential to exploit the full potential of metal halide perovskites (MHPs). Since optimising PSCs is labour-intensive, determination of the upper limit of the V_{oc} on basis of the characteristics of a bare perovskite semiconductor layer is extremely useful.

The qV_{oc} is the Quasi-Fermi level splitting, μ_F under illumination at open circuit and is defined by:²⁰

$$\mu_F = \frac{kT}{q} \ln \frac{(n_0 + \Delta n)(p_0 + \Delta p)}{n_i^2} \quad (1)$$

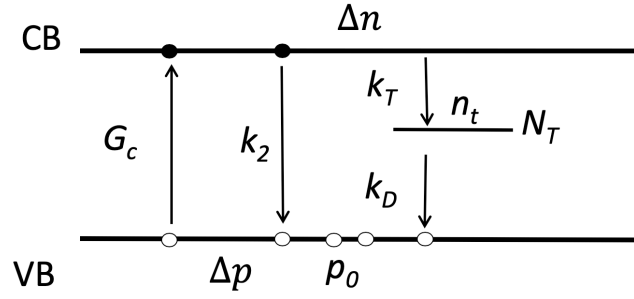
where the $\frac{kT}{q}$ is the thermal energy, n_i is the intrinsic carrier concentration, n_0 and p_0 are thermal-equilibrium concentrations of electrons and holes respectively, and Δn and Δp are the concentrations of photo-excited excess electrons and holes, respectively. From quasi-steady-state photoconductance data measured by making use of a coil, the effective lifetime of charges in a semiconductor layer can be extracted.²¹ In case the semiconductor properties are known including the charge carrier mobilities, the excess charge carrier densities under AM1.5 can then be calculated allowing to come to a value for the Fermi level splitting. We are not aware of any report using this technique for predicting the V_{oc} in perovskite cells, most likely due to the fact that the mobilities are varying with composition, morphology and post treatment.²¹

An alternative way to quantify μ_F is using photoluminescence (PL), by either fitting the absolute intensity PL spectrum including sub-gap tail states,²² or using the absolute PL quantum yield.²³⁻²⁵ However these methods require knowledge of the PL output coupling and reabsorption features of the MHP. Another approach to come to μ_F is probing the charge carrier dynamics by time-resolved measurements like time-resolved microwave photoconductance (TRMC), optical-pump-THz-probe spectroscopy (THz), or transient absorption spectroscopy (TAS). In this work we first present a method how to derive the μ_F under AM1.5 using the rate constants found by fitting time resolved photoconductance measurements on a spin-coated MAPbI₃ film. In the second part, we apply this approach on previously published TRMC data.²⁶⁻²⁸ Interestingly, we find that for vacuum-evaporated MAPbI₃ layers and for (MA,FA,Cs)Pb(I/Br)₃ doped with K⁺, the calculated μ_F is very close to the reported V_{oc} values. This implies that for an improvement of V_{oc} the charge carrier recombination within the native MHP has to be reduced. Additionally, we observe that the addition of Cs⁺ and/or Rb⁺ to (MA,FA)Pb(I/Br)₃ or light-soaking in humid air of MAPbI₃ leads to an increase of both the calculated μ_F and of the observed V_{oc} . However, for these cells the maximum attainable V_{oc} has not been reached yet. This means that the V_{oc} of these solar cells could be further improved by optimizing the interface with the transport layers. Comparing the calculated μ_F with the V_{oc} helps to select which deposition techniques, additives, post production treatments and transport layers are beneficial to improve the efficiency of MHP solar cells.

RESULTS AND DISCUSSION

Chapter 2

In the first part of this chapter a method to calculate μ_F under continuous illumination with the rate constants describing the charge decay kinetics is presented. To this end we recorded TRMC traces of MAPbI₃ using a nanosecond pulsed laser at 500 nm, while varying the incident intensity over four orders of magnitude shown in Figure 2. 1a. We make use of our kinetic model reported in 2015, which has been successfully applied to a range of MHP layers.^{28,29,30,31} Scheme 2.1 depicts all the processes included in the model, in which n_t , is the concentration of trapped electrons, p_0 the concentration of background holes, and N_T the density of available deep traps; k_2 , k_T , k_D are the rate constants representing band-to-band recombination, trapping and trap depopulation respectively, while G_c represents the optical excitation.



Scheme 2.1. The kinetic model describing the charge carrier dynamics in perovskites.

$$\frac{d\Delta n}{dt} = G_c - k_2\Delta n(\Delta p + p_0) - k_T\Delta n(N_T - n_t) \quad (2)$$

$$\frac{d\Delta p}{dt} = G_c - k_2\Delta n(\Delta p + p_0) - k_D n_t(\Delta p + p_0) \quad (3)$$

$$\frac{dn_t}{dt} = k_T\Delta n(N_T - n_t) - k_D n_t(\Delta p + p_0) \quad (4)$$

To obtain values for all kinetic parameters, we solved the coupled differential Equations 2 - 4 numerically with the same set of parameters except for the generation term, which equals the intensity of the laser pulses. From the resulting time-dependent Δn and Δp , we can determine the time dependent photoconductance, ΔG , by:

$$\Delta G = e(\mu_e\Delta n + \mu_p\Delta p)\beta L \quad (5)$$

where μ_e and μ_p are the mobilities of electrons and holes, respectively. βL is the geometrical constant and L the layer thickness. As shown in Figure 2. 1a, the fits match the experimental TRMC traces very well. Note that below a certain excitation density the traces start to overlap, which indicates that the recombination turns from higher order to first order. From this

threshold, starting at densities around $4 \times 10^{14} \text{ cm}^{-3}$ per pulse, we can accurately ascertain N_T . (see Figure 2.s S1a and S1b)

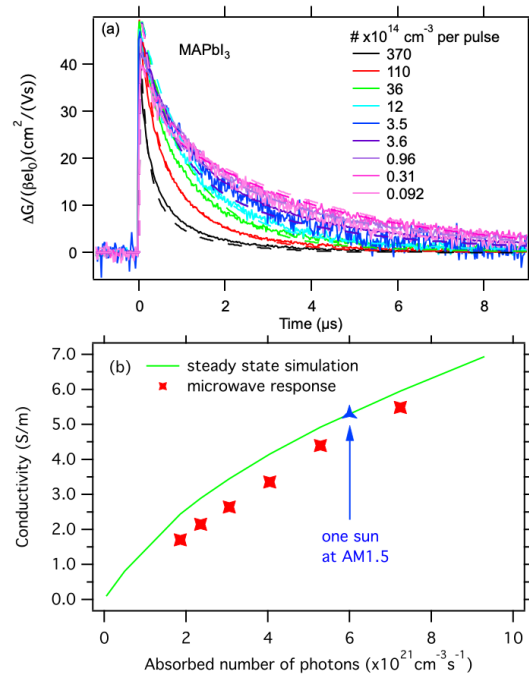


Figure 2. 1. (a) TRMC traces (solid) along with the fits (dashed) of the spin-coated MAPbI₃ thin film. The excitation density per laser pulse is presented by the number of absorbed photons divided by the thickness of the sample. (b) The red markers denote the conductivities obtained from the microwave signal induced by continuous illumination using a white light LED. The green line is the photoconductivity calculated using the charge carrier concentrations found by integration of equations 2 - 4 as function of G_c . The blue arrow corresponds to a G_c identical to the number of absorbed photons by this layer under one sun at AM1.5.

Figure 2. 1a shows that we can use our model shown in Scheme 2.1 to extract dynamic parameters and to calculate Δn , Δp , and n_t as a function of time. In case all the essential processes are captured by our kinetic model, it should be possible to switch from pulsed excitation to continuous excitation. Hence we calculated Δn , Δp , and n_t using Equations 2-4, with the previously obtained set of dynamics parameters but replacing the pulsed G_c by continuous excitation. In Figure 2.s S2a and S2b the time dependent concentrations are shown using intensities comparable to 1% and 100% of AM1.5 reaching constant values within 20.

To verify these calculated values for Δn and Δp , we compared the photo-conductivity, $\Delta\sigma$ derived from the calculated charge carrier concentrations with $\Delta\sigma$ measured under

Chapter 2

continuous excitation. In Figure 2. 1b, the red markers denote $\Delta\sigma$ as function of the absorbed number of photons generated by a white light LED. A more detailed explanation how we extract $\Delta\sigma$ from the microwave response is provided in the SI with Figure 2. S3-5. As shown in Figure 2. 1b, excellent agreement between the calculated and measured $\Delta\sigma$ is observed. This resemblance demonstrates that our kinetic model captures all the essential photophysical processes within intensities between 1 and 100% of AM1.5 and can be used for predicting the steady-state excess charge carriers concentrations. Hence, we can use our pulsed time-resolved measurements to evaluate the excess carrier concentration at open circuit in a solar cell.

In the next part, we will process previously published TRMC data in the same way as described as above to obtain Δn and Δp under excitation conditions similar to AM1.5, from which we will derive μ_F using equation 1. These μ_F values will be then compared with the V_{oc} values of the corresponding PSCs.²⁶⁻²⁸ These PSCs were made using different precursors and fabrication procedures (spin-coated and evaporated MAPbI₃, (MA,FA,Cs)Pb(I/Br)₃, (MA,FA)Pb(I/Br)₃), and comprise different device structures and transport materials. The effect of additives like K⁺, Cs⁺ and/or Rb⁺ and of post-production treatments such as light soaking were also investigated. The TRMC traces and fits are shown in Figure 2. S6. Note that these TRMC traces have been recorded on films identical to those used for the solar cell fabrication. The key fitting parameters are listed in Table 2. 1, and the full set of the parameters are collected in Table S2.1. In order to determine μ_F using equation 1, not only Δn and Δp are required, but also n_i , n_0 and p_0 . We calculated n_i of MAPbI₃ to be $12.6 \times 10^4 \text{ cm}^{-3}$ from previously published values of the effective masses³²⁻³⁸ and a bandgap of 1.58 eV (see equation S6-8). For (MA,FA,Cs)Pb(I/Br)₃, we assume the same effective masses as those of MAPbI₃ but used bandgaps of 1.56 and 1.59 eV for perovskite layers with and without K⁺ doping, respectively. p_0 is obtained from fitting the TRMC traces, and n_0 can be derived by $p_0 n_0 = n_i^2$. However, the values of n_0 and p_0 are negligibly small compared to Δn and Δp , as listed in Table S2.1. The calculated values of μ_F/e for different excitation intensities, along with the experimentally measured V_{oc} values are shown in Figure 2. 2.

Table 2. 1. Kinetic parameters derived from analysis of the TRMC traces, calculated excess concentrations and μ_F/e values for different PSCs.

	MAPbI ₃ evaporated ^a	(MA,FA)Pb (I/Br) ₃ Spin-coated ^b	(MA,FA)Pb (I/Br) ₃ with RbCs Spin-coated ^b	(MA,FA,Cs)Pb (I/Br) ₃ spin-coated ^c	(MA,FA,Cs) Pb(I/Br) ₃ with K spin-coated ^c	MAPbI ₃ spin- coated ^d	MAPbI ₃ spin- coated light soaking ^d
k_2 (10^{-10} cm^3s^{-1})	50	6	3	40	20	2.6	0.76
N_T (10^{13}cm^{-3})	30	250	80	30	30	6	5.5
Δn (10^{14}cm^{-3})	3.1	5.8	24	5.5	9	41	78
Δp (10^{14}cm^{-3})	5.5	17	28	6.8	11	42	78
n_t (10^{13}cm^{-3})	24	11	41	13	18	6.0	5.5
μ_F/e (V)	1.15	1.18	1.23	1.17	1.16	1.26	1.29
second-order ratio η_2 (%)	62	23	67	82	83	96	97

^a Evaporated MAPbI₃, data from Ref ²⁸

^b Spin-coated Mixed perovskite with and without rubidium and cesium, data from Ref.³⁹

^c Spin-coated Mixed perovskite with and without 10% potassium, data from Ref.²⁶

^d Spin-coated MAPbI₃, treated by light soaking in humid air, data from Ref. ²⁷

Chapter 2

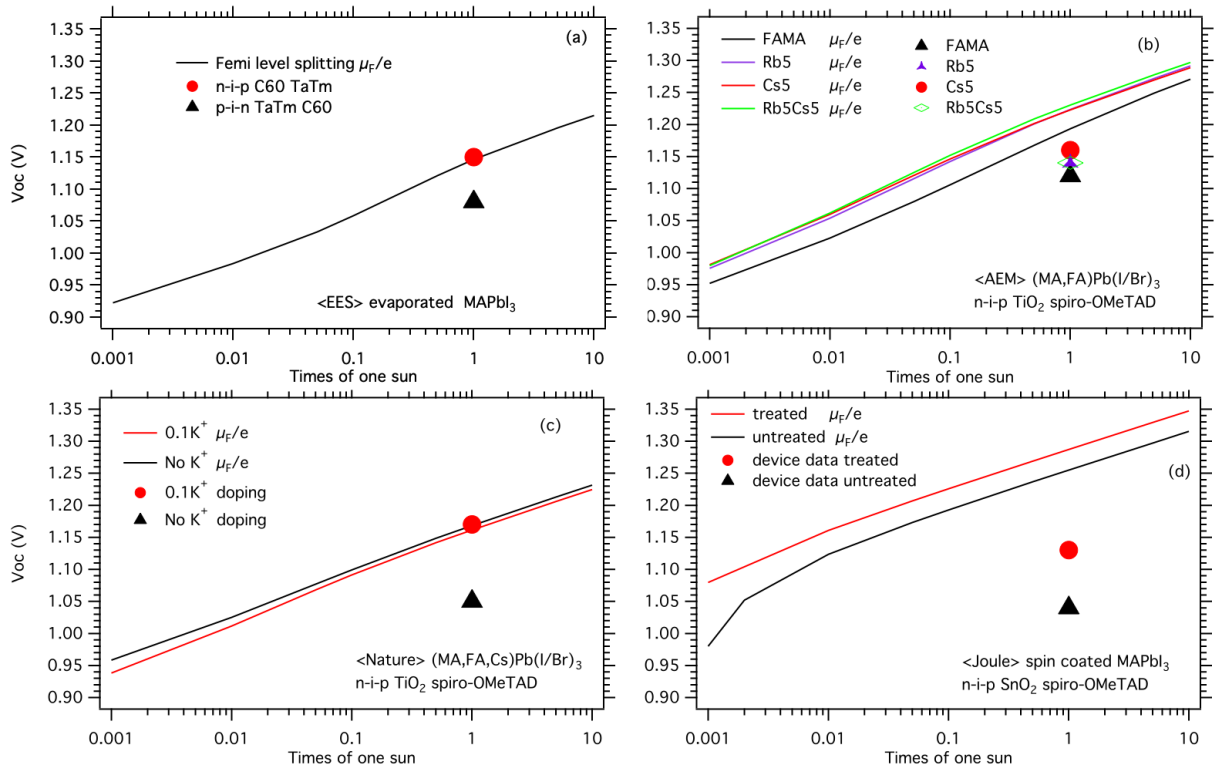


Figure 2. 2. Comparison between the calculated Quasi-Fermi level splitting (full lines), μ_F/e , and the corresponding experimental V_{oc} (markers). The data shown in (a), (b), (c) and (d) are taken from references 28, 39, 26 and 27 respectively.^{26–28,39} The deposition method of the MHP layers, device structures and treatments are given in the annotations.

Figure 2. 2a shows that although both solar cells are fabricated using the same evaporated MAPbI₃, the V_{oc} for the n(C60)-i-p(TaTm) structure is 1.15 V, while for the inverted stack the V_{oc} is 1.08 V. The former value is actually very close to our calculated value of 1.15 V, which supports the idea that our model can accurately determine μ_F/e and that this value is close to the V_{oc} .^{40,41} This is in agreement with recent studies from Nazeeruddin et al.⁴⁰ and Dänekamp et al.⁴¹ claiming that the Fermi levels of both transport materials sandwiching the MHP have little effect on the V_{oc} of a PSC. Hence additional increase of the V_{oc} requires improvement of the MAPbI₃, leading to larger excess charge carrier concentrations.²⁸ The lower value for the p-i-n solar cell structure might be related to changes in opto-electronic properties obtained by deposition on different bottom layers.

In Figure 2. 2b the impact of Cs⁺ and/or Rb⁺ addition to (MA,FA)Pb(I/Br)₃ on μ_F/e and V_{oc} is shown. Cells containing 5% of Cs⁺ and/or 5% Rb⁺ ³⁹ all exhibit a higher V_{oc} , following the same trend as our modelled results. Although other groups have found higher V_{oc} values up to 1.19V,^{42,43} all V_{oc} values are still smaller than the calculated μ_F/e , which implies that deposition of the transport layers results in additional decay pathways and that higher V_{oc} values are feasible by optimising the transport layers. Interestingly, from our calculations it is important to note that μ_F/e for (MA,FA)Pb(I/Br)₃ is equal to that of the evaporated MAPbI₃ samples (having the same bandgap), implying that both fabrication methods are capable of producing similar quality MHPs.

For (MA,FA,Cs)Pb(I/Br)₃ with and without K⁺ passivation, the dependencies of μ_F/e with intensity are very similar, while the measured V_{oc} values differ significantly as shown in Figure 2. 2c. This increase in V_{oc} is attributed to the passivation by K of surface states formed by the deposition of the HTM layer.²⁶ Hence, we suggest that the K-doping retards the interfacial recombination between the MHP and spiro-OMeTAD. Again, by either optimizing the device structure and/or by effectively passivating the interfaces, considerable rise of the V_{oc} can be realized. However, additional increase of the V_{oc} requires improvement of the (MA,FA,Cs)Pb(I/Br)₃ leading to higher excess charge carrier concentrations.

An efficient way to improve the μ_F/e of a MAPbI₃ layer is light soaking in humid air.²⁷ As shown in Figure 2. 2d, a μ_F/e value of 1.29 V at 1 sun is observed, which is very close to the theoretical maximum of 1.33 V predicted for MAPbI₃.¹⁷⁻¹⁹ Despite this great potential, this value has not been realised, although very recent work proved that a V_{oc} of 1.26 V can be obtained by optimising the transport layers and light soaking.¹⁶

The above presented methodology enables us to evaluate the ratio of second-order recombination over the total decay processes, η_2 , defined by:

$$\eta_2 = \frac{R_2}{R_2 + R_T} \quad (6)$$

Here $R_2 = k_2 \Delta n (\Delta p + p_0)$ and $R_T = k_T \Delta n (N_T - n_t)$, representing the decay of excess electrons by second-order and by trap mediated processes under steady-state excitation, respectively. Ideally $\eta_2 = 1$, meaning all excess carriers decay by band-to-band recombination.

As can be observed by the results presented in Table 2. 1, all the additions or treatments lead to a substantial reduction of k_2 , and the highest η_2 values were obtained by the light soaking treatment.²⁷ The small value of N_T is attributed to the improved bulk quality of the MAPbI₃ film mainly by the addition of hypophosphorous acid in combination with PbAc₂ to the perovskite precursor solution.⁴⁴ The light soaking treatment, which is shown to affect the

Chapter 2

surface rather than the bulk, only slightly decreases N_T , but leads to a substantial elongation of the apparent charge carrier lifetime.²⁶ Note, that the k_2 is the apparent rate constant, as previously discussed by Brenes et al,²⁶ which means that the value of k_2 might be substantially reduced by e.g. reabsorption of emitted photons. However, for determination of μ_F/e the apparent rates are of importance as these also apply in a complete device. The apparent values of k_2 obtained by other techniques, e.g. 8.1×10^{-11} from transient absorption (TA)²¹ or 4.5×10^{-10} from optical-pump-THz-probe spectroscopy (THZ)⁴⁵ are in the same range as our data, which supports the idea that the present approach can also be used for kinetic parameters obtained by these other time-resolved measurements.

In summary, in this chapter we present how to derive μ_F/e from pulsed excitation experiments on bare, non-contacted perovskite films. We show that the obtained values correspond to the measured V_{oc} for a number of MHP solar cells, indicating that decay processes occurring within the perovskite layer are limiting the V_{oc} for those cells, rather than interfacial recombination processes. From our modelling we conclude that the addition of Cs^+ and Rb^+ and even more effectively light soaking in air of MHPs leads to substantial increase of the μ_F/e . Although these additions or treatments have resulted in improved V_{oc} values, these methods bear the promise that higher voltages are still feasible by improving the transport layers and preventing recombination at the interface with these contact layers. This work helps to select which steps can help to improve the efficiency of MHP solar cells.

REFERENCES

- (1) Kojima, A.; Teshima, K.; Shirai, Y.; Miyasaka, T. Organometal Halide Perovskites as Visible-Light Sensitizers for Photovoltaic Cells. *J. Am. Chem. Soc.* **2009**, *131*, 6050–6051.
- (2) National Renewable Energy Laboratory. Research Cell Record Efficiency Chart <https://www.nrel.gov/pv/assets/images/efficiency-chart.png> (accessed Jan 30, 2019).
- (3) Ono, L. K.; Juarez-Perez, E. J.; Qi, Y. Progress on Perovskite Materials and Solar Cells with Mixed Cations and Halide Anions. *ACS Appl. Mater. Interfaces* **2017**, *9*, 30197–

- 30246.
- (4) Jesper Jacobsson, T.; Correa-Baena, J.-P.; Pazoki, M.; Saliba, M.; Schenk, K.; Grätzel, M.; Hagfeldt, A. Exploration of the Compositional Space for Mixed Lead Halogen Perovskites for High Efficiency Solar Cells. *Energy Environ. Sci.* **2016**, *9*, 1706–1724.
 - (5) Peer, A.; Biswas, R.; Park, J.-M.; Shinar, R.; Shinar, J. Light Management in Perovskite Solar Cells and Organic LEDs with Microlens Arrays. *Opt. Express* **2017**, *25*, 10704.
 - (6) Manzoor, S.; Yu, Z. J.; Ali, A.; Ali, W.; Bush, K. A.; Palmstrom, A. F.; Bent, S. F.; McGehee, M. D.; Holman, Z. C. Improved Light Management in Planar Silicon and Perovskite Solar Cells Using PDMS Scattering Layer. *Sol. Energy Mater. Sol. Cells* **2017**, *173*, 59–65.
 - (7) Hou, Y.; Du, X.; Scheiner, S.; McMeekin, D. P.; Wang, Z.; Li, N.; Killian, M. S.; Chen, H.; Richter, M.; Levchuk, I. A Generic Interface to Reduce the Efficiency-Stability-Cost Gap of Perovskite Solar Cells. *Science* **2017**, *358*, 1192–1197.
 - (8) Christians, J. A.; Schulz, P.; Tinkham, J. S.; Schloemer, T. H.; Harvey, S. P.; Tremolet De Villers, B. J.; Sellinger, A.; Berry, J. J.; Luther, J. M. Tailored Interfaces of Unencapsulated Perovskite Solar Cells for >1,000 Hour Operational Stability. *Nat. Energy* **2018**, *3*, 68–74.
 - (9) Hou, Y.; Scheiner, S.; Tang, X.; Gasparini, N.; Richter, M.; Li, N.; Schweizer, P.; Chen, S.; Chen, H.; Quiroz, C. O. R.; et al. Suppression of Hysteresis Effects in Organohalide Perovskite Solar Cells. *Adv. Mater. Interfaces* **2017**, *4*, 1–9.
 - (10) Shin, S. S.; Yeom, E. J.; Yang, W. S.; Hur, S.; Kim, M. G.; Im, J.; Seo, J.; Noh, J. H.; Seok, S. Il. Colloidally Prepared La-Doped BaSnO₃ Electrodes for Efficient, Photostable Perovskite Solar Cells. *Science* **2017**, *356*, 167–171.

Chapter 2

- (11) Calió, L.; Kazim, S.; Grätzel, M.; Ahmad, S. Hole-Transport Materials for Perovskite Solar Cells. *Angew. Chemie - Int. Ed.* **2016**, *55*, 14522–14545.
- (12) Petrus, M. L.; Schutt, K.; Sirtl, M. T.; Hutter, E. M.; Closs, A. C.; Ball, J. M.; Bijleveld, J. C.; Petrozza, A.; Bein, T.; Dingemans, T. J.; et al. New Generation Hole Transporting Materials for Perovskite Solar Cells: Amide-Based Small-Molecules with Nonconjugated Backbones. *Adv. Energy Mater.* **2018**, *1801605*, 1801605.
- (13) Li, Y.; Ding, B.; Chu, Q. Q.; Yang, G. J.; Wang, M.; Li, C. X.; Li, C. J. Ultra-High Open-Circuit Voltage of Perovskite Solar Cells Induced by Nucleation Thermodynamics on Rough Substrates. *Sci. Rep.* **2017**, *7*, 1–10.
- (14) Saygili, Y.; Turren-Cruz, S. H.; Olthof, S.; Saes, B. W. H.; Pehlivan, I. B.; Saliba, M.; Meerholz, K.; Edvinsson, T.; Zakeeruddin, S. M.; Grätzel, M.; et al. Planar Perovskite Solar Cells with High Open-Circuit Voltage Containing a Supramolecular Iron Complex as Hole Transport Material Dopant. *ChemPhysChem* **2018**, *19*, 1363–1370.
- (15) Anaraki, E. H.; Kermanpur, A.; Steier, L.; Domanski, K.; Matsui, T.; Tress, W.; Saliba, M.; Abate, A.; Grätzel, M.; Hagfeldt, A.; et al. Highly Efficient and Stable Planar Perovskite Solar Cells by Solution-Processed Tin Oxide. *Energy Environ. Sci.* **2016**, *9*, 3128–3134.
- (16) Liu, Z.; Krückemeier, L.; Krogmeier, B.; Klingebiel, B.; Márquez, J. A.; Levchenko, S.; Öz, S.; Mathur, S.; Rau, U.; Unold, T.; et al. Open-Circuit Voltages Exceeding 1.26 V in Planar Methylammonium Lead Iodide Perovskite Solar Cells. *ACS Energy Lett.* **2018**, 110–117.
- (17) Sha, W. E. I.; Ren, X.; Chen, L.; Choy, W. C. H. The Efficiency Limit of $\text{CH}_3\text{NH}_3\text{PbI}_3$

- Perovskite Solar Cells. *Appl. Phys. Lett.* **2015**, *106*, 221104.
- (18) Tress, W.; Yavari, M.; Domanski, K.; Yadav, P.; Niesen, B.; Correa Baena, J. P.; Hagfeldt, A.; Graetzel, M. Interpretation and Evolution of Open-Circuit Voltage, Recombination, Ideality Factor and Subgap Defect States during Reversible Light-Soaking and Irreversible Degradation of Perovskite Solar Cells. *Energy Environ. Sci.* **2018**, *11*, 151–165.
- (19) Tress, W.; Marinova, N.; Inganäs, O.; Nazeeruddin, M. K.; Zakeeruddin, S. M.; Graetzel, M. Predicting the Open-Circuit Voltage of $\text{CH}_3\text{NH}_3\text{PbI}_3$ Perovskite Solar Cells Using Electroluminescence and Photovoltaic Quantum Efficiency Spectra: The Role of Radiative and Non-Radiative Recombination. *Adv. Energy Mater.* **2015**, *5*, 1400812.
- (20) Neamen, D. A. *Semiconductor Physics & Devices: Basic Principles*, Fourth Edi.; McGraw-Hill Education: New York, NY 10121, 2012.
- (21) Sinton, R. A.; Cuevas, A. Contactless Determination of Current-Voltage Characteristics and Minority-Carrier Lifetimes in Semiconductors from Quasi-Steady-State Photoconductance Data. *Appl. Phys. Lett.* **1996**, *69*, 2510–2512.
- (22) Braly, I. L.; Dequilettes, D. W.; Pazos-Outón, L. M.; Burke, S.; Ziffer, M. E.; Ginger, D. S.; Hillhouse, H. W. Hybrid Perovskite Films Approaching the Radiative Limit with over 90% Photoluminescence Quantum Efficiency. *Nat. Photonics* **2018**, *12*, 355–361.
- (23) Kirchartz, T.; Krückemeier, L.; Unger, E. L. Research Update: Recombination and Open-Circuit Voltage in Lead-Halide Perovskites. *APL Mater.* **2018**, *6*, 100702.
- (24) Stolterfoht, M.; Caprioglio, P.; Wolff, C. M.; Márquez, J. A.; Nordmann, J.; Zhang, S.; Rothhardt, D.; Hörmann, U.; Redinger, A.; Kegelmann, L.; et al. The Perovskite/Transport Layer Interfaces Dominate Non-Radiative Recombination in

Chapter 2

- Efficient Perovskite Solar Cells. *arXiv Prepr. arXiv1810.01333* **2018**.
- (25) Paetzold, U. W.; Hebig, J.-C.; Mock, J.; Kirchartz, T.; Hempel, H.; Staub, F.; Unold, T.; Rau, U. Beyond Bulk Lifetimes: Insights into Lead Halide Perovskite Films from Time-Resolved Photoluminescence. *Phys. Rev. Appl.* **2016**, *6*, 1–13.
- (26) Abdi-Jalebi, M.; Andaji-Garmaroudi, Z.; Cacovich, S.; Stavrakas, C.; Philippe, B.; Richter, J. M.; Alsari, M.; Booker, E. P.; Hutter, E. M.; Pearson, A. J.; et al. Maximizing and Stabilizing Luminescence from Halide Perovskites with Potassium Passivation. *Nature* **2018**, *555*, 497–501.
- (27) Brenes, R.; Guo, D.; Osherov, A.; Noel, N. K.; Eames, C.; Hutter, E. M.; Pathak, S. K.; Niroui, F.; Friend, R. H.; Islam, M. S.; et al. Metal Halide Perovskite Polycrystalline Films Exhibiting Properties of Single Crystals. *Joule* **2017**, *1*, 155–167.
- (28) Momblona, C.; Gil-Escrig, L.; Bandiello, E.; Hutter, E. M.; Sessolo, M.; Lederer, K.; Blochwitz-Nimoth, J.; Bolink, H. J. Efficient Vacuum Deposited P-i-n and n-i-p Perovskite Solar Cells Employing Doped Charge Transport Layers. *Energy Environ. Sci.* **2016**, *9*, 3456–3463.
- (29) Hutter, E. M.; Eperon, G. E.; Stranks, S. D.; Savenije, T. J. Charge Carriers in Planar and Meso-Structured Organic-Inorganic Perovskites: Mobilities, Lifetimes, and Concentrations of Trap States. *J. Phys. Chem. Lett.* **2015**, *6*, 3082–3090.
- (30) Chandrashekar, S.; Abdi-Jalebi, M.; Sutton, R. J.; Hutter, E. M.; Savenije, T. J.; Stranks, S. D.; Snaith, H. J. Vapour-Deposited Cesium Lead Iodide Perovskites: Microsecond Charge Carrier Lifetimes and Enhanced Photovoltaic Performance. *ACS Energy Lett.* **2017**, *2*, 1901–1908.

- (31) Hutter, E. M.; Gélvez-Rueda, M. C.; Bartesaghi, D.; Grozema, F. C.; Savenije, T. J. Band-Like Charge Transport in $\text{Cs}_2\text{AgBiBr}_6$ and Mixed Antimony-Bismuth $\text{Cs}_2\text{AgBi}_{1-x}\text{Sb}_x\text{Br}_6$ Halide Double Perovskites. *ACS Omega* **2018**, *3*, 11655–11662.
- (32) Yang, J.-P.; Meissner, M.; Yamaguchi, T.; Zhang, X.-Y.; Ueba, T.; Cheng, L.-W.; Ideta, S.; Tanaka, K.; Zeng, X.-H.; Ueno, N.; et al. Band Dispersion and Hole Effective Mass of Methylammonium Lead Iodide Perovskite. *Sol. RRL* **2018**, *1800132*, 1800132.
- (33) Umari, P.; Mosconi, E.; De Angelis, F. Relativistic GW Calculations on $\text{CH}_3\text{NH}_3\text{PbI}_3$ and $\text{CH}_3\text{NH}_3\text{SnI}_3$ Perovskites for Solar Cell Applications. *Sci. Rep.* **2014**, *4*, 4467.
- (34) Egger, D. A.; Bera, A.; Cahen, D.; Hodes, G.; Kirchartz, T.; Kronik, L.; Lovrincic, R.; Rappe, A. M.; Reichman, D. R.; Yaffe, O. What Remains Unexplained about the Properties of Halide Perovskites? *Adv. Mater.* **2018**, *30*, 1–11.
- (35) Giorgi, G.; Fujisawa, J. I.; Segawa, H.; Yamashita, K. Small Photocarrier Effective Masses Featuring Ambipolar Transport in Methylammonium Lead Iodide Perovskite: A Density Functional Analysis. *J. Phys. Chem. Lett.* **2013**, *4*, 4213–4216.
- (36) Quarti, C.; Mosconi, E.; De Angelis, F. Interplay of Orientational Order and Electronic Structure in Methylammonium Lead Iodide: Implications for Solar Cell Operation. *Chem. Mater.* **2014**, *26*, 6557–6569.
- (37) Davies, C. L.; Filip, M. R.; Patel, J. B.; Crothers, T. W.; Verdi, C.; Wright, A. D.; Milot, R. L.; Giustino, F.; Johnston, M. B.; Herz, L. M. Bimolecular Recombination in Methylammonium Lead Triiodide Perovskite Is an Inverse Absorption Process. *Nat. Commun.* **2018**, *9*, 1–9.
- (38) Brenner, T. M.; Egger, D. A.; Kronik, L.; Hodes, G.; Cahen, D. Hybrid Organic—Inorganic Perovskites: Low-Cost Semiconductors with Intriguing Charge-Transport

Chapter 2

- Properties. *Nat. Rev. Mater.* **2016**, *1*, 16011.
- (39) Hu, Y.; Hutter, E. M.; Rieder, P.; Grill, I.; Hanisch, J.; Aygüler, M. F.; Hufnagel, A. G.; Handloser, M.; Bein, T.; Hartschuh, A.; et al. Understanding the Role of Cesium and Rubidium Additives in Perovskite Solar Cells: Trap States, Charge Transport, and Recombination. *Adv. Energy Mater.* **2018**, *1703057*, 1703057.
- (40) Ravishankar, S.; Gharibzadeh, S.; Roldán-Carmona, C.; Grancini, G.; Lee, Y.; Ralaiarisoa, M.; Asiri, A. M.; Koch, N.; Bisquert, J.; Nazeeruddin, M. K. Influence of Charge Transport Layers on Open-Circuit Voltage and Hysteresis in Perovskite Solar Cells. *Joule* **2018**, 1–11.
- (41) Dänekamp, B.; Droseros, N.; Tsokkou, D.; Brehm, V.; Boix, P. P.; Sessolo, M.; Banerji, N.; Bolink, H. J. Influence of Hole Transport Material Ionization Energy on the Performance of Perovskite Solar Cells. *J. Mater. Chem. C* **2019**, *7*, 523–527.
- (42) Abate, A.; Hagfeldt, A.; Gratzel, M.; Correa-Baena, J.-P.; Saliba, M.; Ummadisingu, A.; Seo, J.-Y.; Matsui, T.; Zakeeruddin, S. M.; Tress, W. R.; et al. Incorporation of Rubidium Cations into Perovskite Solar Cells Improves Photovoltaic Performance. *Science*. **2016**, *354*, 206–209.
- (43) Fu, R.; Zhao, Y.; Zhou, W.; Li, Q.; Zhao, Y.; Zhao, Q. Ultrahigh Open-Circuit Voltage for High Performance Mixed-Cation Perovskite Solar Cells Using Acetate Anions. *J. Mater. Chem. A* **2018**, *6*, 14387–14391.
- (44) Zhang, W.; Pathak, S.; Sakai, N.; Stergiopoulos, T.; Nayak, P. K.; Noel, N. K.; Haghighirad, A. A.; Burlakov, V. M.; deQuilettes, D. W.; Sadhanala, A.; et al. Enhanced Optoelectronic Quality of Perovskite Thin Films with Hypophosphorous Acid for Planar

Heterojunction Solar Cells. *Nat. Commun.* **2015**, *6*, 10030.

- (45) Milot, R. L.; Eperon, G. E.; Snaith, H. J.; Johnston, M. B.; Herz, L. M. Temperature-Dependent Charge-Carrier Dynamics in CH₃NH₃PbI₃ Perovskite Thin Films. *Adv. Funct. Mater.* **2015**, *25*, 6218–6227.

Appendices

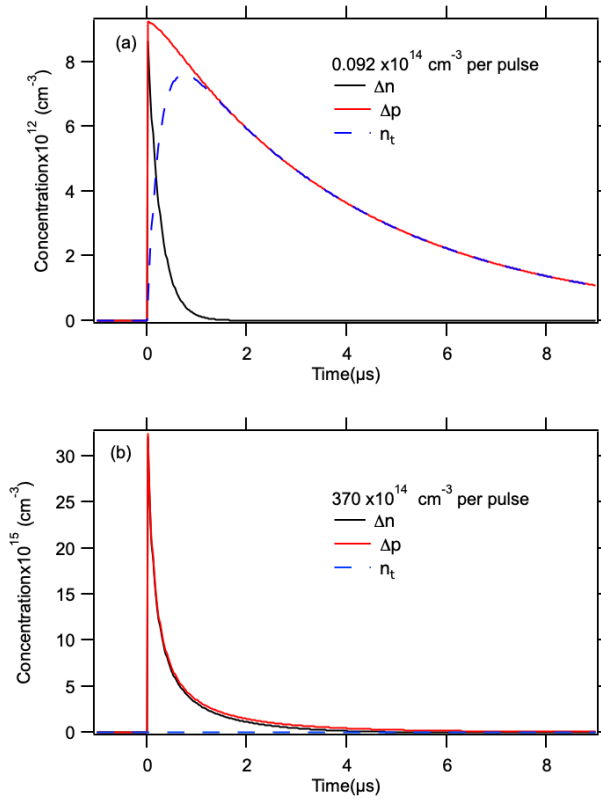


Figure S2.1: (a and b) Decay profiles of Δn (black), Δp (red), and n_t (dashed blue), under the lowest and highest used excitation densities, respectively.

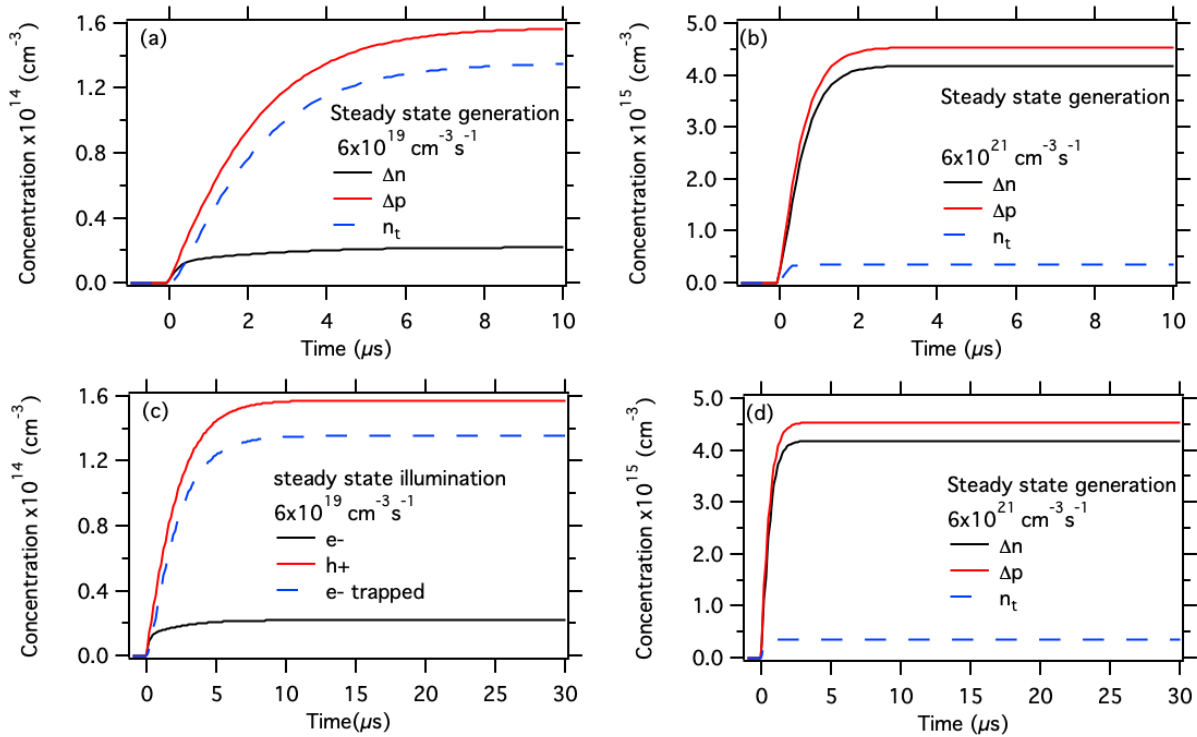


Figure S2.2: Calculated Δn (black), Δp (red), and n_t (blue) under continuous excitation using parameters determined from the pulsed photoconductance measurements. The steady state

excitation densities correspond to (a) 1% and (b) 100% of the number of photons that the MAPI layer would absorb under AM1.5. (c and d) the densities in (a) and (b) shown on longer timescales.

Time-resolved microwave photo-conductivity (TRMC)

The working principle of TRMC is based on the interaction of microwaves and a conductive medium. Upon photoexcitation charge carriers are generated within the material analysed. As a result, a reduction of microwave power is observed. The change in microwave power ($\Delta P/P$) is proportional to the change in photoconductivity (ΔG) of the sample, as expressed by:

$$\frac{\Delta P(t)}{P} = -K\Delta G(t) \quad (\text{Eq. S1})$$

where, K is a pre-determined sensitivity factor.

In order to maximise the interactions, the sample is placed within a resonant cavity cell, at $\frac{3}{4}\Lambda$ (Λ being the total length of the cavity) from the front quartz window. This position corresponds to one of the maxima of the microwave field. By sweeping the frequencies in the range 8.2-12.2 GHz it is possible to locate the resonance frequency at which the interaction is maximized. At this point, the reflected microwave power goes through a minimum, from now on called the “dip”. All the measurements are then conducted at the resonance frequency.

Steady-State Microwave Conductance (SSMC)

The same set-up described above can be used to measure the conductance (σ) of a sample in steady state conditions. In order to do so, the dip in the frequency scans is analysed. The reduction of microwave power in steady state condition is proportional to the change in conductivity of the sample, as:

$$\frac{\Delta P}{P} = \Delta\sigma\beta L \quad (\text{Eq. S2})$$

Where β is a geometrical factor and L is the sample's thickness. The change in conductivity can be determined from the microwave scans by analysing the data considering the field

Chapter 2 Appendices

characteristics, geometrical factors and properties of the media inside the cavity (quartz and perovskite film in this study). In order to be able to compare different samples in different conditions, all the traces are first normalized with a scan recorded placing a fully reflective end-plate instead of a cavity. Geometrical factors and cavity related losses are then accurately determined by analysing the dips of the empty cavity and then loaded with a clean quartz plate only.

The electrical conductivity of a material is defined as:

$$\sigma = e(\mu_n \Delta n + \mu_p \Delta p) \quad (\text{Eq. S3})$$

Where μ_n and μ_p represent the electron and hole mobilities, respectively. Their values can be determined from the results of TRMC measurements.

By comparing dark and under illumination conditions, it is possible to calculate the changes in conductivity and hence charge carrier concentration caused by steady state photo-excitation of the sample. The fitting results are shown in Figure S2.3:

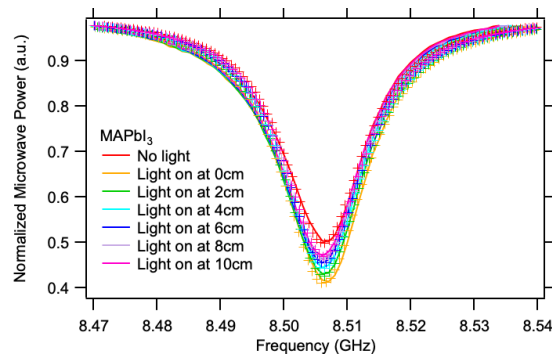


Figure S2.3. The dip of the frequency scans (markers) along with the fits (solid lines)

LED output

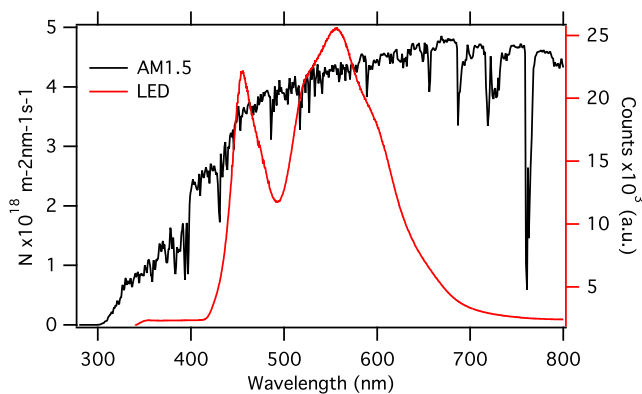


Figure S2.4: Comparison of the AM1.5 and the LED emission spectra.

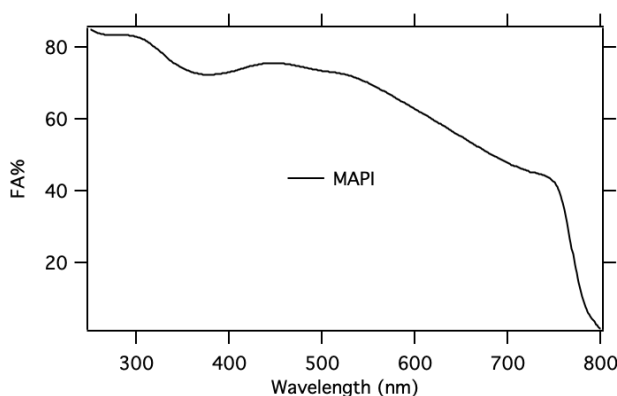


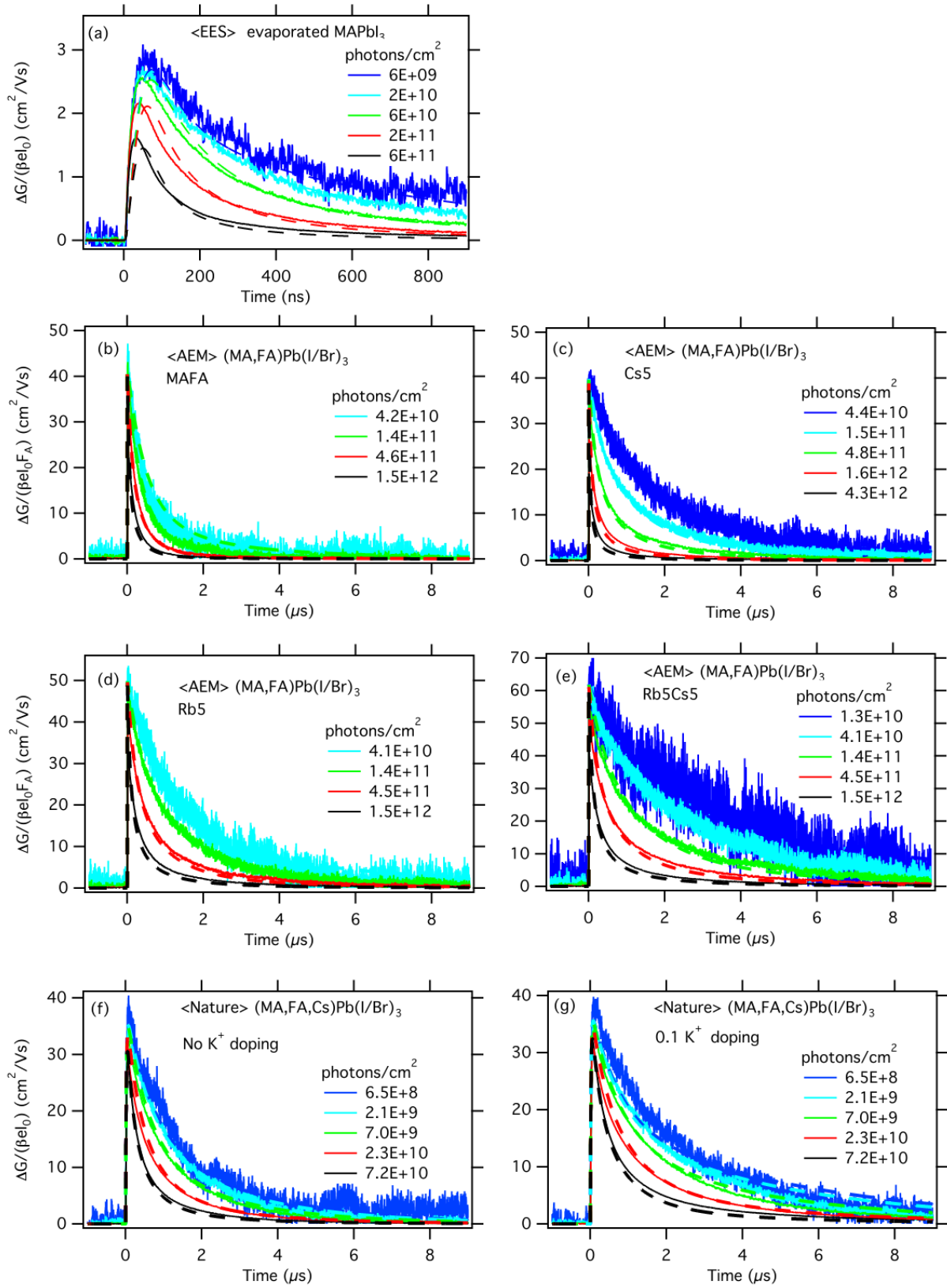
Figure S2.5: The fraction of absorbed light (FA) in MAPbI₃.

We use the following method for calculation of the excitation density per second, G_C in the MHP induced by the white light LED of which the emission spectrum is shown in Figure S2.4. We measured the light intensity at the position of the MHP layer by replacing the sample by a silicon reference cell (Model #RC-02-Si-K7-KT-4D-00-00, Serial #PVM1096, Monocrystalline Silicon). We set the distance of the LED to the TRMC cell to obtain a series of the incident number of photons. The distances were 0 cm, 2 cm, 4 cm, 6 cm, 8 cm and 10 cm, yielding currents of 63 mA, 46 mA, 35.2 mA, 26.6 mA, 20.5 mA, 16.2 mA, respectively on the silicon reference cell with area 2.3 cm².

The reference cell generates a current of 35.275 mA/cm² when AM1.5 is applied. In the range of 280 nm to 1100 nm, the integrated number of photons is $2.71 \cdot 10^{17}$ (cm²s)⁻¹. With these numbers, we can calculate the number of photons for each LED intensity. For example, at a

Chapter 2 Appendices

distance of 10 cm the current is 7.04 mA/cm² then the number of photons is $2.71 \cdot 10^{17} / 35.275 \times 7.04 = 0.54 \cdot 10^{17} \text{ (cm}^2\text{s)}^{-1}$. Considering the F_A shown in Figure S2.5, the excitation density per second is $0.54 \cdot 10^{17} \times 0.686 = 0.37 \cdot 10^{17} \text{ (cm}^2\text{s)}^{-1}$. The linearity of our reference cell is confirmed by another calibrated silicon photodetector (COHERENT, 2303 Lindbergh ST. Ser. UN59, Auburn CA95602-9595) and a pyranometer (Kip&Zonen, Article #3303008, Serial #00990).



Chapter 2 Appendices

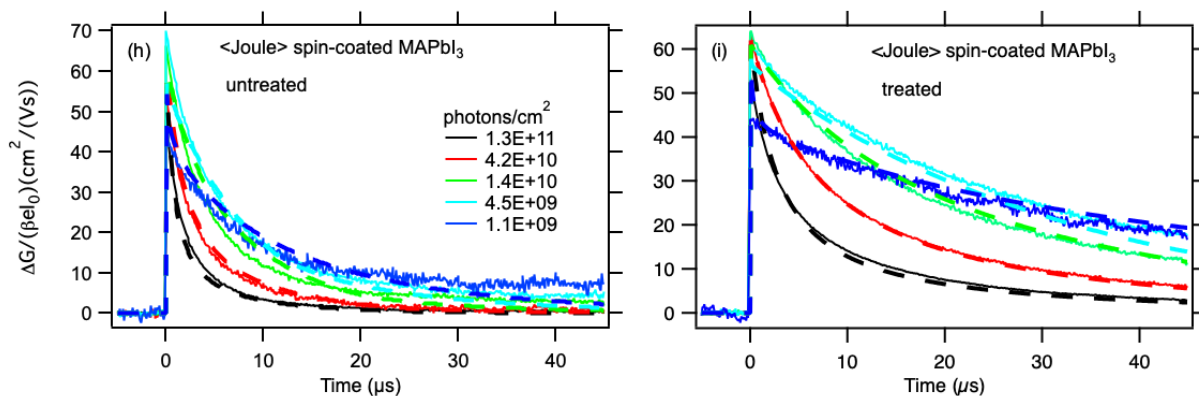


Figure S2.6: The TRMC traces (solid lines) and fits (dash lines) for each published paper discussed in Figure 2 in the main text. (a) Evaporated MAPbI₃, data from Ref. ¹; (b,c,d,e) Spin-coated Mixed perovskite with and without rubidium and cesium, data from Ref. ²; (f,g) Spin-coated Mixed perovskite with and without 10% potassium, data from Ref. ³; (h,i) Spin-coated MAPbI₃, treated by light soaking in humid air, data from Ref. ⁴

Table S2.1: Full set of parameters from the model fitting for each paper. As n_0 is negligible from $n_0 \cdot p_0 = n_i^2$, we do not include it in this table.

	MAPbI ₃ evaporated ^a	(MA,FA)Pb (I/Br) ₃ Spin-coated ^b	(MA,FA)Pb (I/Br) ₃ with Rb Spin-coated ^b	(MA,FA)Pb (I/Br) ₃ with Cs Spin-coated ^b	(MA,FA)Pb (I/Br) ₃ with RbCs Spin-coated ^b
$\sum \mu$	6	6	40	40	6
E_G (eV)	1.58	1.58	1.58	1.58	1.58
n_i (cm ⁻³) same $N_c N_v$	126426	126426	126426	126426	126426
k_T (10 ⁻⁸ cm ³ s ⁻¹)	4	0.1	0.1	0.1	0.1
k_2 (10 ⁻¹⁰ cm ³ s ⁻¹)	50	6	3.5	4.1	3
N_T (10 ¹³ cm ⁻³)	30	250	100	80	80
k_D (10 ⁻¹⁰ cm ³ s ⁻¹)	40	20	9	9	8
p_0 (10 ¹³ cm ⁻³)	30	12	10	10	8
Δn (10 ¹⁴ cm ⁻³)	3.1	9.8	20	20	23.8
Δp (10 ¹⁴ cm ⁻³)	5.5	15.4	24.8	24.1	27.9
n_t (10 ¹³ cm ⁻³)	24	56.7	4.6	3.8	4.1

μ_F (eV)	1.15	1.19	1.22	1.22	1.23
second-order ratio η_2 (%)	62	34	63	71	67

	MAPbI ₃ evaporated ^a	(MA,FA,Cs)Pb (I/Br) ₃ spin-coated ^c	(MA,FA,Cs) Pb(I/Br) ₃ with K spin-coated ^c	MAPbI ₃ spin-coated ^d	MAPbI ₃ spin-coated light soaking ^d
$\Sigma\mu$	6	60	40	60	60
E_G (eV)	1.58	1.59	1.56	1.58	1.58
n_i (cm ⁻³) same N _c N _v	126426	104231	186002	126426	126426
k_T (10 ⁻⁸ cm ³ s ⁻¹)	4	0.4	0.4	12	12
k_2 (10 ⁻¹⁰ cm ³ s ⁻¹)	50	40	20	2.6	0.76
N_T (10 ¹³ cm ⁻³)	30	30	30	6	5.5
k_D (10 ⁻¹⁰ cm ³ s ⁻¹)	40	40	20	8	3.2
p_0 (10 ¹³ cm ⁻³)	30	9	9	6.5	2
Δn (10 ¹⁴ cm ⁻³)	3.1	5.5	9	41	78
Δp (10 ¹⁴ cm ⁻³)	5.5	6.8	11	42	78
n_t (10 ¹³ cm ⁻³)	24	13	18	6.0	5.5
μ_F (eV)	1.15	1.17	1.16	1.26	1.29
second-order ratio η_2 (%)	62	82	83	96	97

^a Evaporated MAPbI₃, data from Ref ¹

^b Spin-coated Mixed perovskite with and without rubidium and cesium, data from Ref.²

^c Spin-coated Mixed perovskite with and without 10% potassium, data from Ref.³

^d Spin-coated MAPbI₃, treated by light soaking in humid air, data from Ref. ⁴

Determination of intrinsic carrier concentration n_i

The equations are:

$$n_i = N_c N_v \exp\left(\frac{-E_g}{kT}\right) \quad (\text{Eq. S6})$$

$$N_c = 2\left(\frac{2\pi m_n^* kT}{h^2}\right)^{\frac{3}{2}} \quad (\text{Eq. S7})$$

$$N_v = 2\left(\frac{2\pi m_p^* kT}{h^2}\right)^{\frac{3}{2}} \quad (\text{Eq. S8})$$

Where m_n^* and m_p^* are the effective masses of electrons and holes, respectively.

The published m_n^* and m_p^* are listed below:

Chapter 2 Appendices

$$m_p^*/m_0=0.25, {}^5 0.25, {}^6 0.28, {}^6 0.36, {}^6 0.26, {}^7 0.29, {}^8 0.18-0.52, {}^9 0.23, {}^{10} 0.14. {}^{10}$$

$$m_n^*/m_0=0.19, {}^6 0.17, {}^6 0.73, {}^6 0.1-0.15, {}^{11} 0.23, {}^7 0.23, {}^8 0.14-0.20, {}^9 0.22, {}^{10} 0.12. {}^{10}$$

Hence the averages are $m_n^*=0.15m_0$ and $m_p^*=0.27m_0$, regardless of the extremely outstanding values, for instance 0.73 for m_n^* .

Then the $n_i = 126426$ based on the bandgap of 1.58 eV. This value is comparable to the published $8.08 \pm 0.39 \cdot 10^4$ calculated from absorption coefficient.

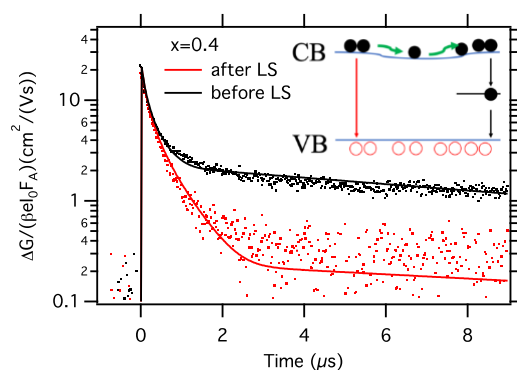
REFERENCES

- (1) Momblona, C.; Gil-Escrig, L.; Bandiello, E.; Hutter, E. M.; Sessolo, M.; Lederer, K.; Blochwitz-Nimoth, J.; Bolink, H. J. Efficient Vacuum Deposited P-i-n and n-i-p Perovskite Solar Cells Employing Doped Charge Transport Layers. *Energy Environ. Sci.* **2016**, *9*, 3456–3463.
- (2) Hu, Y.; Hutter, E. M.; Rieder, P.; Grill, I.; Hanisch, J.; Aygüler, M. F.; Hufnagel, A. G.; Handloser, M.; Bein, T.; Hartschuh, A.; et al. Understanding the Role of Cesium and Rubidium Additives in Perovskite Solar Cells: Trap States, Charge Transport, and Recombination. *Adv. Energy Mater.* **2018**, *1703057*, 1703057.
- (3) Abdi-Jalebi, M.; Andaji-Garmaroudi, Z.; Cacovich, S.; Stavrakas, C.; Philippe, B.; Richter, J. M.; Alsari, M.; Booker, E. P.; Hutter, E. M.; Pearson, A. J.; et al. Maximizing and Stabilizing Luminescence from Halide Perovskites with Potassium Passivation. *Nature* **2018**, *555*, 497–501.
- (4) Brenes, R.; Guo, D.; Osherov, A.; Noel, N. K.; Eames, C.; Hutter, E. M.; Pathak, S. K.; Niroui, F.; Friend, R. H.; Islam, M. S.; et al. Metal Halide Perovskite Polycrystalline Films Exhibiting Properties of Single Crystals. *Joule* **2017**, *1*, 155–167.

- (5) Yang, J.-P.; Meissner, M.; Yamaguchi, T.; Zhang, X.-Y.; Ueba, T.; Cheng, L.-W.; Ideta, S.; Tanaka, K.; Zeng, X.-H.; Ueno, N.; et al. Band Dispersion and Hole Effective Mass of Methylammonium Lead Iodide Perovskite. *Sol. RRL* **2018**, *1800132*, 1800132.
- (6) Umari, P.; Mosconi, E.; De Angelis, F. Relativistic GW Calculations on $\text{CH}_3\text{NH}_3\text{PbI}_3$ and $\text{CH}_3\text{NH}_3\text{SnI}_3$ Perovskites for Solar Cell Applications. *Sci. Rep.* **2014**, *4*, 4467.
- (7) Egger, D. A.; Bera, A.; Cahen, D.; Hodes, G.; Kirchartz, T.; Kronik, L.; Lovrincic, R.; Rappe, A. M.; Reichman, D. R.; Yaffe, O. What Remains Unexplained about the Properties of Halide Perovskites? *Adv. Mater.* **2018**, *30*, 1–11.
- (8) Giorgi, G.; Fujisawa, J. I.; Segawa, H.; Yamashita, K. Small Photocarrier Effective Masses Featuring Ambipolar Transport in Methylammonium Lead Iodide Perovskite: A Density Functional Analysis. *J. Phys. Chem. Lett.* **2013**, *4*, 4213–4216.
- (9) Quarti, C.; Mosconi, E.; De Angelis, F. Interplay of Orientational Order and Electronic Structure in Methylammonium Lead Iodide: Implications for Solar Cell Operation. *Chem. Mater.* **2014**, *26*, 6557–6569.
- (10) Davies, C. L.; Filip, M. R.; Patel, J. B.; Crothers, T. W.; Verdi, C.; Wright, A. D.; Milot, R. L.; Giustino, F.; Johnston, M. B.; Herz, L. M. Bimolecular Recombination in Methylammonium Lead Triiodide Perovskite Is an Inverse Absorption Process. *Nat. Commun.* **2018**, *9*, 1–9.
- (11) Brenner, T. M.; Egger, D. A.; Kronik, L.; Hodes, G.; Cahen, D. Hybrid Organic—Inorganic Perovskites: Low-Cost Semiconductors with Intriguing Charge-Transport Properties. *Nat. Rev. Mater.* **2016**, *1*, 16011.

Chapter 2 Appendices

Chapter 3 Reversible Removal of Intermixed Shallow States by Light Soaking in Multi-Cation Mixed Halide Perovskite Films



This part has been published:

Guo, D.; Garmaroudi, Z. A.; Abdi-jalebi, M.; Stranks, S. D.; Savenije, T. J. Reversible Removal of Intermixed Shallow States by Light Soaking in Multi-Cation Mixed Halide Perovskite Films. *ACS Energy Lett.* **2019**, *4*, 2360–2367.

Chapter 3

ABSTRACT

The highest reported efficiencies of metal halide perovskite (MHP) solar cells are all based on mixed perovskites, such as $(\text{FA,MA,Cs})\text{Pb}(\text{I}_{1-x}\text{Br}_x)_3$. Despite demonstrated structural changes induced by light soaking, it is unclear how the charge carrier dynamics are affected across this entire material family. Here, various $(\text{FA,MA,Cs})\text{Pb}(\text{I}_{1-x}\text{Br}_x)_3$ perovskite films are light-soaked in nitrogen and changes in opto-electronic properties are investigated through time-resolved microwave conductivity (TRMC), optical and structural techniques. To fit the TRMC decay kinetics obtained for pristine $(\text{FA,MA,Cs})\text{Pb}(\text{I}_{1-x}\text{Br}_x)_3$ for various excitation densities, additional shallow states have to be included, which are not required for describing TRMC traces of single cation MHPs. These shallow states can, independently of x , be removed by light soaking, which leads to a reduction in the imbalance between the diffusional motion of electrons and holes. We interpret the shallow states as a result of initially well-intermixed halide distributions, which on light soaking segregate into domains with distinct bandgaps.

Perovskite solar cells have achieved the fastest increase in power-conversion efficiencies (PCEs) in the solar cell research history, exceeding now 24%.^{1,2} The recent records of perovskite solar cells are all based on mixed cation mixed halide perovskites (MCMHPs).^{2,3} The advantages of MCMHPs in comparison with single cation perovskites are the tunable bandgaps and more stable, black phase,^{4,5} while the main drawback of these perovskites is related to light-induced phase segregation.^{6,7} Several light-soaking studies on MCMHPs solar cells have been carried out which reveal a variety of changes in V_{oc} , I_{sc} , and FF .^{4,8-14} To explain the changes in device performance, various groups studied structural and optical changes in bare MHP layers induced by light soaking. Initially phase segregation, which leads to I-rich and Br-rich domains, was reported in both $\text{MAPb}(\text{I}_{1-x}\text{Br}_x)_3$ and $\text{FAPb}(\text{I}_{1-x}\text{Br}_x)_3$ as determined by either photoluminescence (PL) emission,^{7,15-17} differential-absorption-spectra¹³ or by XRD.¹⁸⁻²⁰ The addition of Cs stabilizes $(\text{FA,MA})\text{Pb}(\text{I}_{1-x}\text{Br}_x)_3$ ⁴ and increases the PCE output.²¹ However, from the work by Tress et al.,⁸ phase segregation still occurs in $(\text{FA,MA,Cs})\text{Pb}(\text{I}_{1-x}\text{Br}_x)_3$ as concluded from a wavelength shift in PL on light soaking. Recent work using micro- and nano focus- XRD techniques from Jones *et al.* revealed structural inhomogeneity in both MCMHP and MAPbI_3 .²² Tsai *et al.* found local lattice distortion in $(\text{FA,MA,Cs})\text{PbI}_3$, and attributed the improvement in device performance on light soaking to interface modification and release of local distortion.²³

The studies above relate structural inhomogeneity to the device performance. However, how the charge carriers in MCMHPs are affected by this structural change is less well studied. In this work, we use optical and time-resolved microwave conductivity (TRMC)²⁴⁻²⁷ techniques to investigate the influence of light soaking on charge-carrier dynamics in various $(\text{FA}_{0.79}\text{MA}_{0.15}\text{Cs}_{0.06})\text{Pb}(\text{I}_{1-x}\text{Br}_x)_3$ with x ranging from 0 to 1. Surprisingly in contrast to most other studied MHPs, mathematical analysis of the decay kinetics of the pristine layers

Chapter 3

with $0.2 \leq x \leq 0.8$ require the presence of shallow states.²⁸ We link these states to a mostly well intermixed halide distribution, leading to a varying energy landscape in the bulk.

Interestingly, these shallow states are seemingly removed on light soaking which we attribute to the conversion of these states into distinct iodide rich, low bandgap domains. The fact that the layers return to their original structure after storage in the dark for over a week reveals that, for these MCMHPs, the presence of shallow states (*i.e.* well intermixed halide distributions) is thermodynamically the most stable conformation.

Throughout this work, we studied bare $(\text{FA}_{0.79}\text{MA}_{0.15}\text{CS}_{0.06})\text{Pb}(\text{I}_{1-x}\text{Br}_x)_3$ films with x varying between 0 and 1 deposited by spin-coating on quartz substrates without any exposure to air or moisture. SEM images of these layers are provided in Figures S1, showing similar grain sizes for all values of x , in agreement with the reported better crystallization of MCMHPs than single cation analogues.⁴ For a number of samples XRD spectra are provided in Figure S2, showing the specific features of the perovskite structure. Light soaking (LS) was accomplished by illumination for 30 minutes with a white light LED with an intensity equivalent to AM1.5 in N_2 . To study the structural reorganization in $(\text{FA}_{0.79}\text{MA}_{0.15}\text{CS}_{0.06})\text{Pb}(\text{I}_{1-x}\text{Br}_x)_3$ on LS, we first measured the absorbance spectra, as shown in **Figure 1**, and detailed band-edge information from photothermal deflection spectroscopy (PDS) (Figure S3a). In Figures 1b and 1c only a subtle shift of the band-edge to longer wavelengths for $x = 0.4$ and $x = 0.6$ on LS is visible, even if the LS treatment is prolonged to overnight exposure. The spectra of non-mixed halides $(\text{FA}_{0.79}\text{MA}_{0.16}\text{CS}_{0.05})\text{PbI}_3$ and $(\text{FA}_{0.79}\text{MA}_{0.16}\text{CS}_{0.05})\text{PbBr}_3$ (Figures 1a and 1d) do not show these optical changes, indicating no structural reorganization occurs on LS. In contrast, the substantial shift in absorption onset of the single cation $\text{MAPb}(\text{I}_{0.6}\text{Br}_{0.4})_3$ shown in Figure S3b, supports the idea that the structural reorganization in the triple cation perovskite on LS is significantly slower than in mono cation perovskites in line with previous observations.²⁹

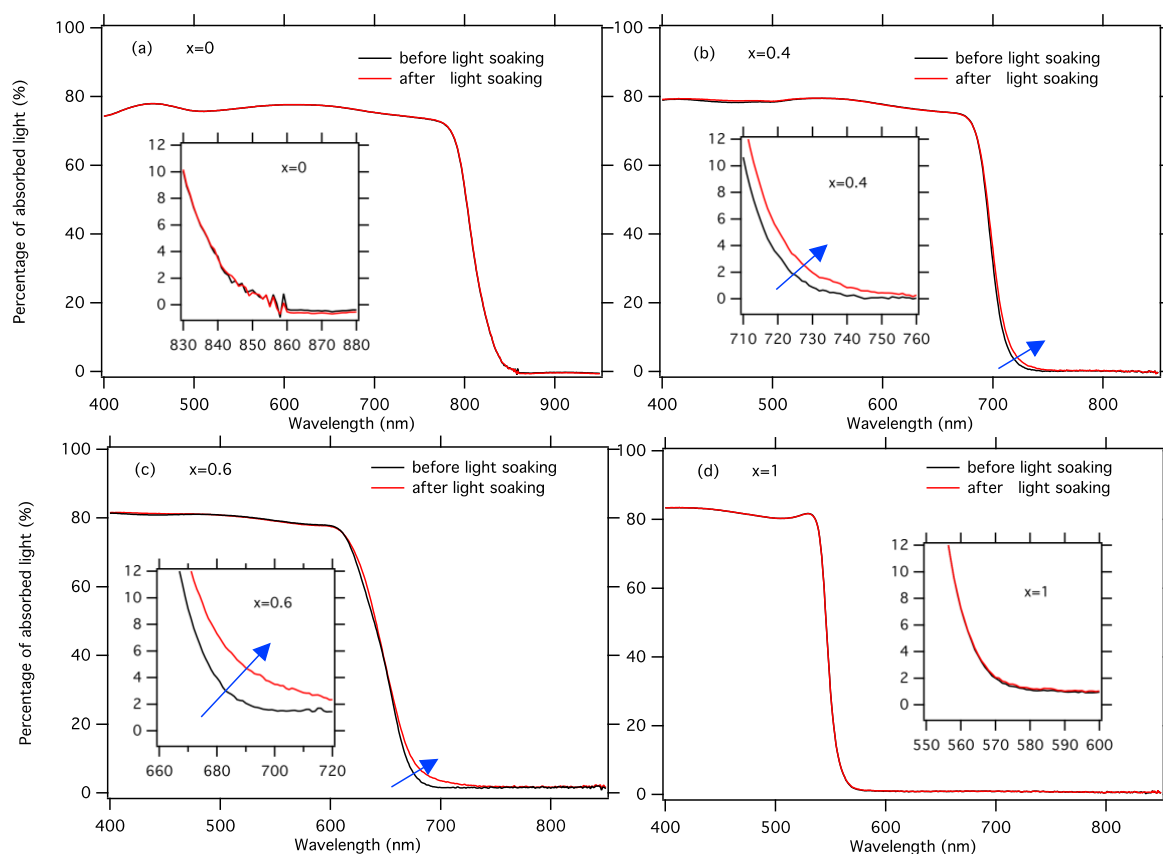


Figure 1. Absorbance spectra before and after light soaking in N_2 for $(FA_{0.79}MA_{0.15}Cs_{0.06})Pb(I_{1-x}Br_x)_3$ with $x = 0$, $x = 0.4$, $x = 0.6$, and $x = 1$. The blue arrows indicate the shift due to the LS. For comparison, the effect of LS on $MAPb(I_{0.6}Br_{0.4})_3$ is shown in Figure S3b. The insets are magnifications to show the subtle shift due to the LS.

Figure 2 collects the corresponding PL spectra on 532 nm CW laser excitation for the same set of MHPs. Figure 2b shows that the PL emission at 715 nm of $(FA_{0.79}MA_{0.16}Cs_{0.05})Pb(I_{0.6}Br_{0.4})_3$ gradually reduces and a second band appears at 760 nm on LS. In Figure 2c similar gradual PL changes for $x = 0.6$ on LS are observed. Despite significant differences in the initial band-gaps of $x = 0.4$, 0.6 and 0.8 (Figure S4a) the PL emission wavelengths on LS are all close to that of $x = 0.2$ (Shown in Figure S4b), in agreement with previous studies on similar mixed MHPs.^{16,17,30–33} Note, that this second PL emission wavelength is still ~ 50 nm blue shifted with respect to that of

Chapter 3

(FA_{0.79}MA_{0.16}CS_{0.05})PbI₃ excluding the formation of bromide free regions (see Figure 2a).

Interestingly, the total PL intensity of both PL bands remains within a factor two constant for $x = 0.4$ and $x = 0.6$, which is in large contrast with MHPs light soaked under humid conditions.^{25,34} The observed PL changes are different to those of single cation MHPs like MAPb(I_{1-x}Br_x)₃ and FAPb(I_{1-x}Br_x)₃. In MAPb(I_{1-x}Br_x)₃, with $x = 0.4$ or $x = 0.6$, a short illumination period leads to a clear PL shift in combination with formation of a shorter-wavelength peak,⁷ which are attributed to I-rich and Br-enriched domains, respectively as reported previously.^{18,33} In order to find out if our observed changes in MCMHP are driven by the presence of a mixture of iodide and bromide, we measured the PL of (FA_{0.79}MA_{0.16}CS_{0.05})PbI₃ and (FA_{0.79}MA_{0.16}CS_{0.05})PbBr₃ on LS, as shown in Figures 2a and 2d. The decrease in PL intensity is comparable to that observed in single cation MHPs.³⁵ However, since the maximum PL intensity for these mono cation MHPs remains at the same wavelength, we conclude that the structural reorganization is propelled by the halide mixture. However, from the profound changes between single cation and multi cation perovskite on LS, we conclude that the multi-cation system slows down the phase segregation tremendously in line with previous observations.³⁵

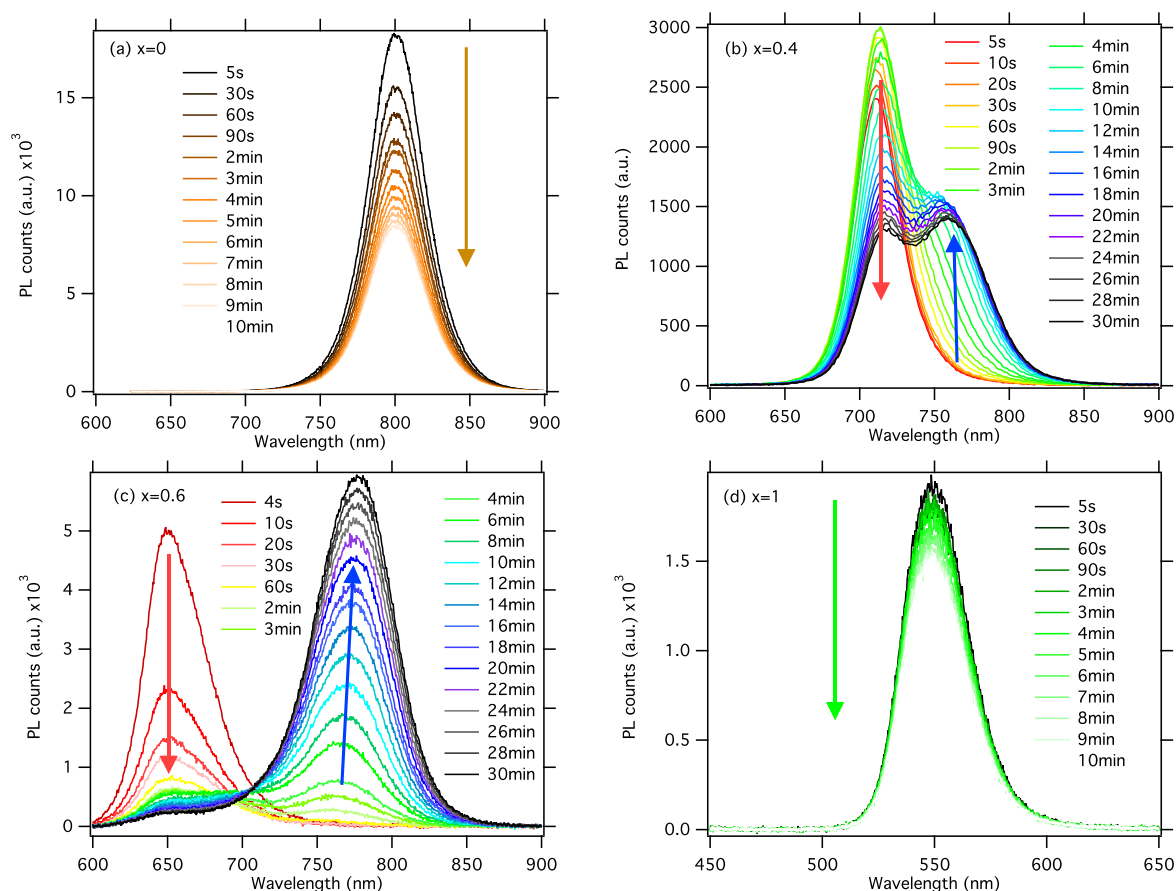
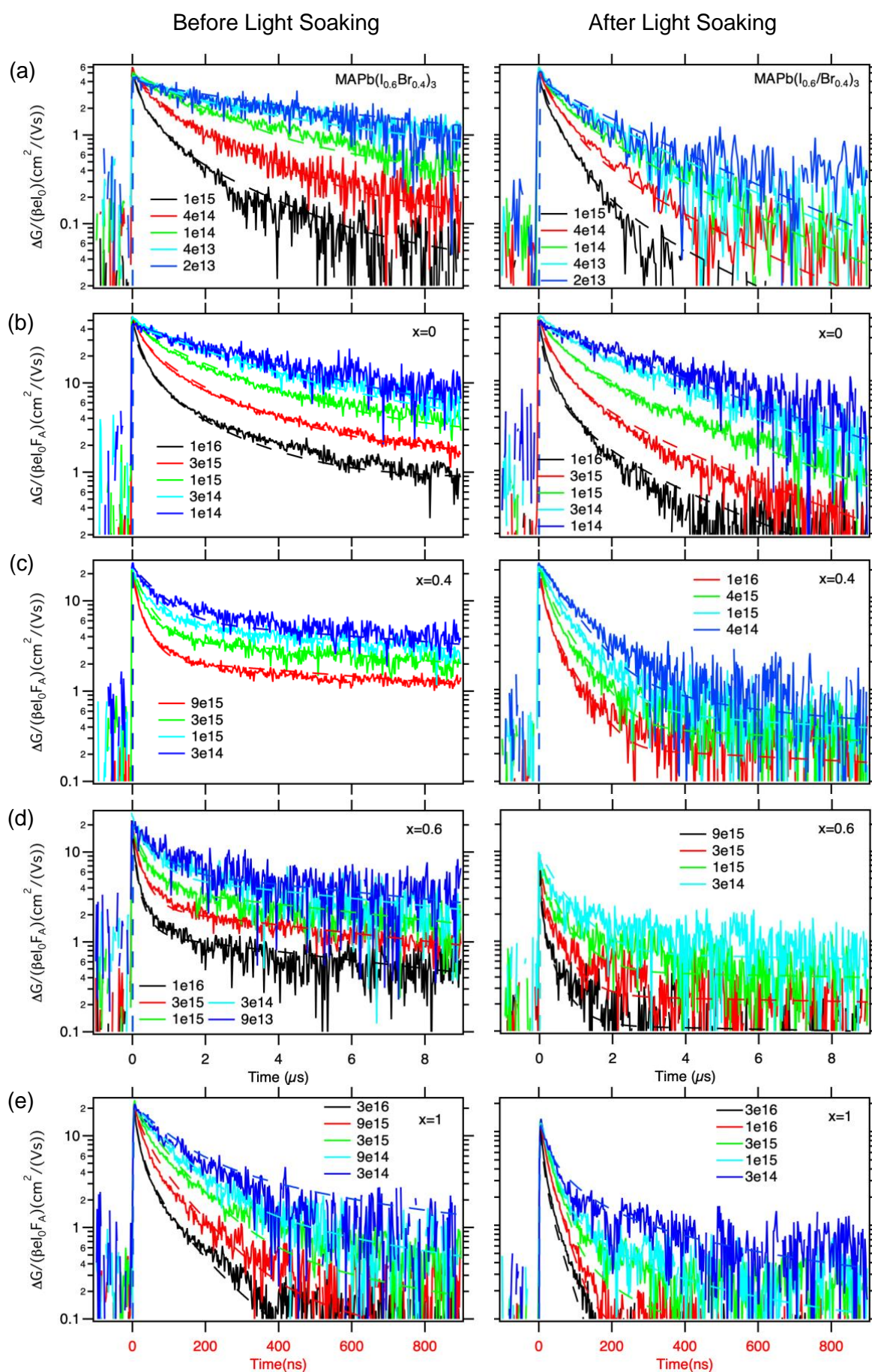


Figure 2. PL spectra of $(\text{FA}_{0.79}\text{MA}_{0.15}\text{CS}_{0.06})\text{Pb}(\text{I}_{1-x}\text{Br}_x)_3$ with $x = 0, 0.4, 0.6$ and 1 in time on light soaking in N_2 (532 nm laser, $\sim 60 \text{ mW/cm}^2$)

To find out whether the bulk crystalline structure is affected by LS, we performed XRD measurements before and after LS of the $x = 0.4$ sample, shown in Figure S2. There are no shifts or additional peaks visible in the XRD pattern on LS confirming that the bulk crystalline structure is not affected and that the size and/or proportion of the iodide enriched domains are far lower and not detectable in these experiments in comparison to the bulk. The amount of PbI_2 is not affected by the LS, as evidenced in Figure S2. The change in XRD patterns reported for single cation mixed halide perovskites supports that the MCMHPs are relatively more stable against LS. ^{33,36}

Chapter 3

To study the effect of LS on the charge carrier dynamics in $(\text{FA}_{0.79}\text{MA}_{0.15}\text{CS}_{0.06})\text{Pb}(\text{I}_{1-x}\text{Br}_x)_3$ with $0 \leq x \leq 1$, we carried out TRMC measurements and recorded traces before and after the LS treatment, as shown in **Figure 3**. For comparison TRMC traces for a single cation perovskite i.e. $\text{MAPb}(\text{I}_{0.6}\text{Br}_{0.4})_3$ are also included. TRMC results for $x = 0.2$ and $x = 0.8$ are provided in Figure S5. The transients show a rapid rise due to formation of excess charge carriers by the laser pulse, while the decay of the signal represents how mobile carriers get immobilized or undergo recombination. The excitation densities range from 10^{14} to 10^{16} cm^{-3} , calculated from the laser intensity, the sample thickness and the fraction of absorbed light at the excitation wavelength. To facilitate comparison of traces acquired using different intensities, the photoconductance signals are normalized to the number of absorbed photons. First important observation is that on LS the charge carrier lifetimes become shorter for in particular the samples with $0.4 \leq x \leq 0.6$. For the latter samples and to a lesser extend $x = 0.2$ and $x = 0.8$ the TRMC tails exhibit the same slope independent of the laser intensity in this log lin representation. This feature is not observed for MHPs with only a single halide, *i.e.* $(\text{FA}_{0.79}\text{MA}_{0.16}\text{CS}_{0.05})\text{PbI}_3$ and $(\text{FA}_{0.79}\text{MA}_{0.16}\text{CS}_{0.05})\text{PbBr}_3$ (Figures 3b and e, left panels), and also for MHPs with only a single cation, $\text{MAPb}(\text{I}_{0.6}\text{Br}_{0.4})_3$ (Figure 3a, left panel). This implies that the occurrence of these TRMC tails is somehow linked to the presence of both mixed cations and mixed halides. Interestingly, this behavior is absent after 30 minutes of LS as clearly visible in the right panels of Figure 3. Much longer LS treatments (17 hours) show essentially the same effect, as shown in Figure S6. The samples show almost complete recovery after storage in the glovebox in the dark for over a week, especially regarding the tails, as shown in Figure S7.



Chapter 3

Figure 3. TRMC traces of MAPb(I_{0.6}Br_{0.4})₃, (a) and (FA_{0.79}MA_{0.15}CS_{0.06})Pb(I_{1-x}Br_x)₃ for (b) $x = 0$, (c) $x = 0.4$ and (d) $x = 0.6$ and (e) $x = 1$, respectively before (left panels) and after (right) light soaking. The analogues $x = 0.2$ and $x = 0.8$ are shown for comparison in Figure S5. Solid lines are the experimental traces and dashed lines are the results of the fits. Note that Figure (e) has a different timescale of 1 μ s. The samples were all excited by laser pulses at 500nm with excitation intensities leading to charge carrier densities ranging from 10^{14} to 10^{16} cm⁻³, and specific densities are given in the annotations.

In order to extract kinetic parameters from the TRMC results we apply a kinetic model recently reported by Hutter et al.²⁶ which successfully described the formation and decay of the light induced charge carriers in MAPbI₃ and other MHPs.^{37–41} In that model two decay pathways for charge-carriers were included: band-to-band recombination, with rate constant k_2 and trap mediated recombination. However, that model was not capable to describe the kinetics of the pristine MHMCPs adequately, implying that at least one additional or different decay pathway is required. Previously, a similar transient behavior was observed for charge carriers in FAPbI₃ at low temperatures.⁴² Moreover, Azulay and coworkers recently evoked the presence of shallow states to explain their scanning tunneling results.²⁸ Therefore, we included in our kinetic model an additional pathway, in which mobile charges are temporarily immobilized with a first order rate constant k_s , and thermally released with k_r as is depicted in **Figure 4a**. Note that, immobilized carriers³⁶ do not contribute to the conductance during the period they reside in these states. This additional pathway could be substantiated by shallow defect states but also by e.g. low crystalline domains in which carriers have a reduced mobility. The corresponding set of differential equations and a more complete description of our fitting procedure are provided in the supporting information (Equations S1-4). The occupancy of these shallow states is expected to be heavily temperature dependent. The lower the temperature the more charges will reside in these shallow states preventing them from

recombining, which would translate into longer charge carrier lifetimes. Note that with TRMC we probe both electrons and holes, weighed with their respective mobility. We measured $x = 0.4$ at different temperatures as shown in **Figure 4b**, showing a gradually smaller slope of the tails with lower temperatures. This is in line with the idea that with lower temperatures one of the carriers remains trapped for longer and longer periods and with that recombination to the ground state is reduced.

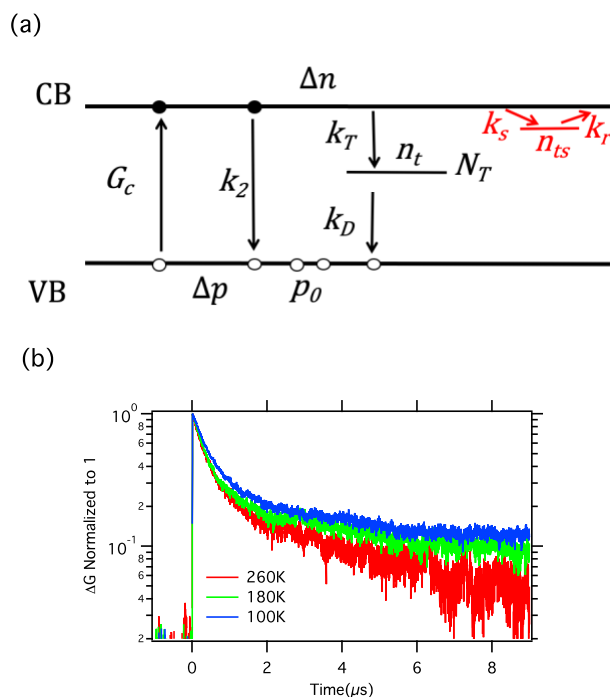


Figure 4. (a) The kinetic model describing the charge carrier dynamics in MHPs with following decay pathways: band-to-band recombination with rate k_2 ; Deep trap assisted recombination with trapping rate k_T and depopulation rate k_D ; Immobilization in shallow states with trapping rate k_s and thermal release rate k_r . (b) Temperature dependent TRMC traces of sample $x = 0.4$ recorded at an excitation density of $5.4 \times 10^{14} \text{cm}^{-3}$.

We applied the modified model to fit all the TRMC traces and results are added to Figure 3 and Figure S5, showing excellent agreement between model and data (see also

Chapter 3

Figure S8 for different representations). The extracted kinetic parameters are listed in Table S1, and are also presented in **Figure 5** and S9. Figure 5a shows the sum of mobilities, which reduces gradually from around 66 cm²/Vs for $x = 0$ to 33 cm²/Vs for $x = 1$. This reduction on increasing Br content in (FA_{0.79}MA_{0.15}CS_{0.06})Pb(I_{1-x}Br_x)₃ is in line with that reported for (FA_{0.83}CS_{0.17})Pb(I_{1-x}Br_x)₃.^{24,43} From Figure 5b, one can see that before LS, the band-to-band recombination rate, k_2 , increases gradually with Br content, which is similar to that reported for FAPb(I_{1-x}Br_x)₃ measurements.¹⁵ On LS, k_2 remains approximately the same for $x \leq 0.4$, while k_2 increases for $0.6 \leq x \leq 1$. Figure 5c shows a gradual increase in trapping and release rates by shallow states with higher Br content. Most importantly, on LS both these rates decrease substantially which implies that both carriers remain now in the valence and conduction band and can recombine. The overall effect is that the charge carrier lifetimes reduce especially for higher intensities in combination with the disappearance of the parallel tails. Important to note here is that the gradual change of the dynamic parameters with x cannot be explained by the morphology of the MCMHP layers since the grain sizes are rather similar as is clear from the SEM images shown in Figure S1.

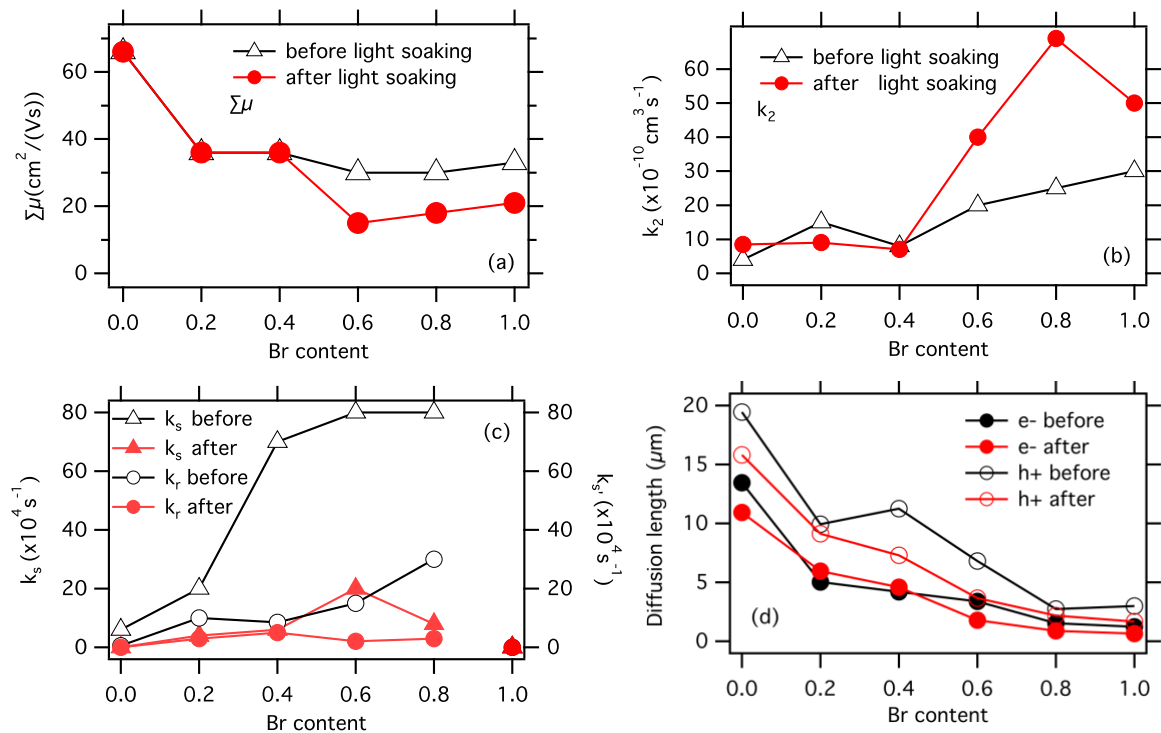


Figure 5. (a) The sum of charge carrier mobilities, $\Sigma\mu$ before (black hollow triangles) and after (red solid circles) light soaking versus Br fraction; (b) Band-to-band recombination rate, k_2 ; (c) Trapping and escaping rates, k_s and k_r of the shallow states; (d) Diffusion lengths of electrons and holes calculated from the lifetimes on excitation at 3×10^{14} cm⁻³ derived from Figure S10.

To picture the effect of the LS on the electronic properties of the MCMHPs, we calculated the charge carrier diffusion lengths before and after LS as shown in Figure 5d. We note here that we assume the material is unintentionally p-doped, however the opposite case is also possible.⁴⁴ These diffusion lengths are calculated on basis of the charge carrier mobilities given in Table S1 via the Einstein–Smoluchowski relation and the lifetimes derived from the rate constants as shown in Figure S10 using a laser intensity leading to an initial excitation density of 3×10^{14} cm⁻³. In particular for (FA,MA,Cs)Pb(I_{1-x}Br_x)₃, with $x = 0.4$ there is an imbalance between the diffusion of electrons and holes since one of the carriers is temporarily

Chapter 3

immobilized. It can be expected that in solar cells this imbalance gives rise to additional space charge fields blocking efficient collection, and in LEDs this imbalance would be detrimental to the charge injection. On LS the shallow states vanish and the decay of electrons and holes becomes almost identical (See Figure S10), and hence the imbalance in diffusion lengths is largely diminished. However, apart from this halide redistribution in a complete cell also ion migration might occur on LS affecting the internal electric field in the device and with that its performance.⁴⁵

To understand the origin of the shallow sub-bandgap states and the effect of the LS on the charge dynamics, we first consider the facts that those states require the presence of both mixed cations and mixed halides. We speculate that a non-uniform distribution of cations and halides leads to intermixed shallow states, in line with previous claims.²⁸ Consequently, a varying energy landscape is created with shallow levels close to the band edge. Correa-Baena *et al.* demonstrated recently that both cations and halides are not homogeneously spread over MCMHP films.⁴⁶ Furthermore, Rehman *et al.* reported that $\text{FAPb}(\text{I}_{1-x}\text{Br}_x)_3$ with x between 0.3 to 0.5 is amorphous in nature and mobilities in those materials are lower than $2 \text{ cm}^2\text{V}^{-1}\text{s}^{-1}$. Temporal localization of excess charge carriers in such intermixed shallow states is fully consistent with the kinetic model shown in Figure 4a, by realizing that the long-lived TRMC signals originate from the mobile counter charges.

As has been argued previously by Hoke *et al.* LS leads to reorganization of the halides resulting in local higher concentrations of iodide atoms.¹⁸ As suggested by Knight *et al.*³⁴ and Belisle *et al.*³⁶ the mechanism of this reorganization process is mediated by the localization of positive charges. Randomly moving iodide atoms cluster near the positive charges providing a thermodynamic driving force to form iodide rich domains. However, we conclude that for our $(\text{FA,MA,Cs})\text{Pb}(\text{I}_{1-x}\text{Br}_x)_3$ films this occurs at the intermixed shallow states. As a result, we suggest that the shallow states of intermixed halides convert into distinct iodide rich, low band-gap domains as is evident from our TRMC and optical data. Hence this process

is different than that for the single cation mixed halide perovskites: although the formation of iodide domains is accelerated by defects, these are appearing preferentially at the illuminated site.^{16,17} The conversion process induced by LS has different effects on the optoelectronic properties depending on x : While for $0.2 \leq x \leq 0.4$ found μ and k_2 values remain constant, for $0.6 \leq x \leq 0.8$ LS leads to a decrease of μ and increasing k_2 values. To explain these observations, we note that these fitting parameters are the results of treating the materials as homogenous media. This results in effective values for μ and k_2 . However, the low band-gap, iodide rich domains have a substantial energetic offset with respect to the bulk: close to 0.3 eV for $x = 0.6$ as deduced from the PL data. Hence on optical excitation of layers with $0.6 \leq x \leq 0.8$ the segregated domains may mediate fast, higher order charge carrier decay as excitations transfer to the lower gap iodide rich domains. Finally on prolonged storage in the dark, the MCMHPs regain their original thermodynamically most favorable structure probably due to entropic reasons.⁴⁷ Thus the shallow states corresponding to intermixed halides are reformed, suggesting that no motion of the cations is involved in the LS process.

In this work, we studied how the dynamics of charge-carriers change on light soaking in various (FA,MA,Cs)Pb(I_{1-x}Br_x)₃ films by PL, optical absorption, XRD and TRMC. Firstly, in such mixed cation and mixed halide perovskites, decay pathways of photo-excited charge-carriers not only include recombination via band-to-band and deep traps but also immobilizing in, and thermally escaping from shallow states independent of x . We speculate that a non-uniform distribution of cations and halides in the (FA,MA,Cs)Pb(I_{1-x}Br_x)₃ films could lead to these intermixed shallow states. The shallow states cause imbalanced electron and hole diffusion lengths. Secondly by light soaking, these states convert into distinct iodide rich, low band-gap domains. For LS samples with $0.2 \leq x \leq 0.4$ the shallow states are virtually absent, while the bulk properties including the mobility and band-to-band

Chapter 3

recombination remain the same. Only for samples with $0.6 \leq x \leq 0.8$ these low band-gap domains lead to enhanced higher order recombination, which will negatively affect the PV performance. Finally, we suggest that by optimizing the constituent ratios, is possible to further improve the mixed perovskite solar cells by making the MCMHP film free of shallow states, which induce the halide segregation.

REFERENCES

- (1) Kojima, A.; Teshima, K.; Shirai, Y.; Miyasaka, T. Organometal Halide Perovskites as Visible-Light Sensitizers for Photovoltaic Cells. *J. Am. Chem. Soc.* **2009**, *131*, 6050–6051.
- (2) NREL. Research Cell Efficiency Records, National Center for Photovoltaics http://www.nrel.gov/ncpv/images/efficiency_chart.jpg (accessed Jul 17, 2018).
- (3) Ono, L. K.; Juarez-Perez, E. J.; Qi, Y. Progress on Perovskite Materials and Solar Cells with Mixed Cations and Halide Anions. *ACS Appl. Mater. Interfaces* **2017**, *9*, 30197–30246.
- (4) Saliba, M.; Matsui, T.; Seo, J.-Y.; Domanski, K.; Correa-Baena, J.-P.; Nazeeruddin, M. K.; Zakeeruddin, S. M.; Tress, W.; Abate, A.; Hagfeldt, A.; et al. Cesium-Containing Triple Cation Perovskite Solar Cells: Improved Stability, Reproducibility and High Efficiency. *Energy Environ. Sci.* **2016**, *9*, 1989–1997.
- (5) Jesper Jacobsson, T.; Correa-Baena, J.-P.; Pazoki, M.; Saliba, M.; Schenk, K.; Grätzel, M.; Hagfeldt, A. Exploration of the Compositional Space for Mixed Lead Halogen Perovskites for High Efficiency Solar Cells. *Energy Environ. Sci.* **2016**, *9*, 1706–1724.
- (6) deQuilettes, D. W.; Zhang, W.; Burlakov, V. M.; Graham, D. J.; Leijtens, T.; Osherov, A.; Bulović, V.; Snaith, H. J.; Ginger, D. S.; Stranks, S. D. Photo-Induced Halide Redistribution in Organic–Inorganic Perovskite Films. *Nat. Commun.* **2016**, *7*, 11683.

- (7) Yoon, S. J.; Draguta, S.; Manser, J. S.; Sharia, O.; Schneider, W. F.; Kuno, M.; Kamat, P. V. Tracking Iodide and Bromide Ion Segregation in Mixed Halide Lead Perovskites during Photoirradiation. *ACS Energy Lett.* **2016**, *1*, 290–296.
- (8) Tress, W.; Yavari, M.; Domanski, K.; Yadav, P.; Niesen, B.; Correa Baena, J. P.; Hagfeldt, A.; Graetzel, M. Interpretation and Evolution of Open-Circuit Voltage, Recombination, Ideality Factor and Subgap Defect States during Reversible Light-Soaking and Irreversible Degradation of Perovskite Solar Cells. *Energy Environ. Sci.* **2018**, *11*, 151–165.
- (9) Hu, J.; Gottesman, R.; Gouda, L.; Kama, A.; Priel, M.; Tirosh, S.; Bisquert, J.; Zaban, A. Photovoltage Behavior in Perovskite Solar Cells under Light-Soaking Showing Photoinduced Interfacial Changes. *ACS Energy Lett.* **2017**, *2*, 950–956.
- (10) Gil-Escrig, L.; Momblona, C.; La-Placa, M. G.; Boix, P. P.; Sessolo, M.; Bolink, H. J. Vacuum Deposited Triple-Cation Mixed-Halide Perovskite Solar Cells. *Adv. Energy Mater.* **2018**, *8*, 1–6.
- (11) Duong, T.; Wu, Y. L.; Shen, H.; Peng, J.; Fu, X.; Jacobs, D.; Wang, E. C.; Kho, T. C.; Fong, K. C.; Stocks, M.; et al. Rubidium Multication Perovskite with Optimized Bandgap for Perovskite-Silicon Tandem with over 26% Efficiency. *Adv. Energy Mater.* **2017**, *1700228*, 1–11.
- (12) Jiang, Q.; Zhang, L.; Wang, H.; Yang, X.; Meng, J.; Liu, H.; Yin, Z.; Wu, J.; Zhang, X.; You, J. Enhanced Electron Extraction Using SnO₂ for High-Efficiency Planar-Structure HC(NH₂)₂PbI₃-Based Perovskite Solar Cells. *Nat. Energy* **2016**, *2*, 16177.
- (13) Samu, G. F.; Janáky, C.; Kamat, P. V. A Victim of Halide Ion Segregation. How Light Soaking Affects Solar Cell Performance of Mixed Halide Lead Perovskites. *ACS Energy Lett.* **2017**, *2*, 1860–1861.
- (14) Nie, W.; Blancon, J.-C.; Neukirch, A. J.; Appavoo, K.; Tsai, H.; Chhowalla, M.; Alam,

Chapter 3

- M. A.; Sfeir, M. Y.; Katan, C.; Even, J.; et al. Light-Activated Photocurrent Degradation and Self-Healing in Perovskite Solar Cells. *Nat. Commun.* **2016**, *7*, 11574.
- (15) Rehman, W.; Milot, R. L.; Eperon, G. E.; Wehrenfennig, C.; Boland, J. L.; Snaith, H. J.; Johnston, M. B.; Herz, L. M. Charge-Carrier Dynamics and Mobilities in Formamidinium Lead Mixed-Halide Perovskites. *Adv. Mater.* **2015**, *27*, 7938–7944.
- (16) Ruth, A.; Brennan, M. C.; Draguta, S.; Morozov, Y. V.; Zhukovskyi, M.; Janko, B.; Zapol, P.; Kuno, M. Vacancy-Mediated Anion Photo-segregation Kinetics in Mixed Halide Hybrid Perovskites: Coupled Kinetic Monte Carlo and Optical Measurements. *ACS Energy Lett.* **2018**, *3*, 2321–2328.
- (17) Barker, A. J.; Sadhanala, A.; Deschler, F.; Gandini, M.; Senanayak, S. P.; Pearce, P. M.; Mosconi, E.; Pearson, A. J.; Wu, Y.; Srimath Kandada, A. R.; et al. Defect-Assisted Photoinduced Halide Segregation in Mixed-Halide Perovskite Thin Films. *ACS Energy Lett.* **2017**, *2*, 1416–1424.
- (18) Hoke, E. T.; Slotcavage, D. J.; Dohner, E. R.; Bowring, A. R.; Karunadasa, H. I.; McGehee, M. D. Reversible Photo-Induced Trap Formation in Mixed-Halide Hybrid Perovskites for Photovoltaics. *Chem. Sci.* **2015**, *6*, 613–617.
- (19) Barker, A. J.; Sadhanala, A.; Deschler, F.; Gandini, M.; Senanayak, S. P.; Pearce, P. M.; Mosconi, E.; Pearson, A. J.; Wu, Y.; Srimath Kandada, A. R.; et al. Defect-Assisted Photoinduced Halide Segregation in Mixed-Halide Perovskite Thin Films. *ACS Energy Lett.* **2017**, *2*, 1416–1424.
- (20) Hu, M.; Bi, C.; Yuan, Y.; Bai, Y.; Huang, J. Stabilized Wide Bandgap MAPbBr_{1-x}I_{3-x} Perovskite by Enhanced Grain Size and Improved Crystallinity. *Adv. Sci.* **2015**, *3*, 6–11.
- (21) Zheng, X.; Wu, C.; Jha, S. K.; Li, Z.; Zhu, K.; Priya, S. Improved Phase Stability of Formamidinium Lead Triiodide Perovskite by Strain Relaxation. *ACS Energy Lett.* **2016**, *1*, 1014–1020.

- (22) Jones, T. W.; Osherov, A.; Alsari, M.; Sponseller, M.; Duck, B. C. Electronic Supplementary Information for : Lattice Strain Causes Non-Radiative Losses in Halide Perovskites. *Energy Environ. Sci.* **2019**, *12*, 1–25.
- (23) Tsai, H.; Asadpour, R.; Blancon, J. C.; Stoumpos, C. C.; Durand, O.; Strzalka, J. W.; Chen, B.; Verduzco, R.; Ajayan, P. M.; Tretiak, S.; et al. Light-Induced Lattice Expansion Leads to High-Efficiency Perovskite Solar Cells. *Science*. **2018**, *360*, 67–70.
- (24) Herz, L. M. Charge-Carrier Mobilities in Metal Halide Perovskites: Fundamental Mechanisms and Limits. *ACS Energy Lett.* **2017**, *2*, 1539–1548.
- (25) Brenes, R.; Guo, D.; Osherov, A.; Noel, N. K.; Eames, C.; Hutter, E. M.; Pathak, S. K.; Niroui, F.; Friend, R. H.; Islam, M. S.; et al. Metal Halide Perovskite Polycrystalline Films Exhibiting Properties of Single Crystals. *Joule* **2017**, *1*, 155–167.
- (26) Hutter, E. M.; Eperon, G. E.; Stranks, S. D.; Savenije, T. J. Charge Carriers in Planar and Meso-Structured Organic-Inorganic Perovskites: Mobilities, Lifetimes, and Concentrations of Trap States. *J. Phys. Chem. Lett.* **2015**, *6*, 3082–3090.
- (27) Wehrenfennig, C.; Eperon, G. E.; Johnston, M. B.; Snaith, H. J.; Herz, L. M. High Charge Carrier Mobilities and Lifetimes in Organolead Trihalide Perovskites. *Adv. Mater.* **2014**, *26*, 1584–1589.
- (28) Azulay, D.; Levine, I.; Gupta, S.; Barak-Kulbak, E.; Bera, A.; San, G.; Simha, S.; Cahen, D.; Millo, O.; Hodes, G.; et al. On the Influence of Multiple Cations on the In-Gap States and Phototransport Properties of Iodide-Based Halide Perovskites. *Phys. Chem. Chem. Phys.* **2018**, *20*, 24444–24452.
- (29) Braly, I. L.; Stoddard, R. J.; Rajagopal, A.; Uhl, A. R.; Katahara, J. K.; Jen, A. K. Y. K.; Hillhouse, H. W. Current Induced Phase Segregation in Mixed Halide Hybrid Perovskites and Its Impact on Two-Terminal Tandem Solar Cell Design. *ACS Energy Lett.* **2017**, *2*, acsenergylett.7b00525.

Chapter 3

- (30) Abdi-Jalebi, M.; Andaji-Garmaroudi, Z.; Cacovich, S.; Stavrakas, C.; Philippe, B.; Richter, J. M.; Alsari, M.; Booker, E. P.; Hutter, E. M.; Pearson, A. J.; et al. Maximizing and Stabilizing Luminescence from Halide Perovskites with Potassium Passivation. *Nature* **2018**, *555*, 497–501.
- (31) Slotcavage, D. J.; Karunadasa, H. I.; McGehee, M. D. Light-Induced Phase Segregation in Halide-Perovskite Absorbers. *ACS Energy Lett.* **2016**, *1*, 1199–1205.
- (32) Gualdrón-Reyes, A. F.; Yoon, S. J.; Barea, E. M.; Agouram, S.; Muñoz-Sanjosé, V.; Meléndez, Á. M.; Niño-Gómez, M. E.; Mora-Seró, I. Controlling the Phase Segregation in Mixed Halide Perovskites through Nanocrystal Size. *ACS Energy Lett.* **2019**, *4*, 54–62.
- (33) Brennan, M. C.; Draguta, S.; Kamat, P. V.; Kuno, M. Light-Induced Anion Phase Segregation in Mixed Halide Perovskites. *ACS Energy Lett.* **2018**, *3*, 204–213.
- (34) Knight, A. J.; Wright, A. D.; Patel, J. B.; Mcmeekin, D. P.; Snaith, H. J.; Johnston, M. B.; Herz, L. M.; Perovskite, H.; Snaith, J.; Johnston, M. B.; et al. Electronic Traps and Phase Segregation in Lead Mixed-Halide Perovskite. *ACS Energy Lett.* **2018**, *4*, 75–84.
- (35) Motti, S. G.; Meggiolaro, D.; Barker, A. J.; Mosconi, E.; Perini, C. A. R.; Ball, J. M.; Gandini, M.; Kim, M.; De Angelis, F.; Petrozza, A. Controlling Competing Photochemical Reactions Stabilizes Perovskite Solar Cells. *Nat. Photonics* **2019**, *13*, 532–539.
- (36) Belisle, R. A.; Bush, K. A.; Bertoluzzi, L.; Gold-Parker, A.; Toney, M. F.; McGehee, M. D. Impact of Surfaces on Photoinduced Halide Segregation in Mixed-Halide Perovskites. *ACS Energy Lett.* **2018**, *3*, 2694–2700.
- (37) Hutter, E. M.; Gélvez-Rueda, M. C.; Bartesaghi, D.; Grozema, F. C.; Savenije, T. J. Band-Like Charge Transport in Cs₂AgBiBr₆ and Mixed Antimony-Bismuth Cs₂AgBi_{1-x}Sb_xBr₆ Halide Double Perovskites. *ACS Omega* **2018**, *3*, 11655–11662.
- (38) Hu, Y.; Hutter, E. M.; Rieder, P.; Grill, I.; Hanisch, J.; Aygüler, M. F.; Hufnagel, A.

- G.; Handloser, M.; Bein, T.; Hartschuh, A.; et al. Understanding the Role of Cesium and Rubidium Additives in Perovskite Solar Cells: Trap States, Charge Transport, and Recombination. *Adv. Energy Mater.* **2018**, 1703057, 1703057.
- (39) Chandrashekar, S.; Abdi-Jalebi, M.; Sutton, R. J.; Hutter, E. M.; Savenije, T. J.; Stranks, S. D.; Snaith, H. J. Vapour-Deposited Cesium Lead Iodide Perovskites: Microsecond Charge Carrier Lifetimes and Enhanced Photovoltaic Performance. *ACS Energy Lett.* **2017**, 2, 1901–1908.
- (40) Pérez-del-Rey, D.; Forgács, D.; Hutter, E. M.; Savenije, T. J.; Nordlund, D.; Schulz, P.; Berry, J. J.; Sessolo, M.; Bolink, H. J. Strontium Insertion in Methylammonium Lead Iodide: Long Charge Carrier Lifetime and High Fill-Factor Solar Cells. *Adv. Mater.* **2016**, 28, 9839–9845.
- (41) Guo, D.; Bartesaghi, D.; Wei, H.; Hutter, E. M.; Huang, J.; Savenije, T. J. Photoluminescence from Radiative Surface States and Excitons in Methylammonium Lead Bromide Perovskites. *J. Phys. Chem. Lett.* **2017**, 8, 4258–4263.
- (42) Wright, A. D.; Milot, R. L.; Eperon, G. E.; Snaith, H. J.; Johnston, M. B.; Herz, L. M. Band-Tail Recombination in Hybrid Lead Iodide Perovskite. *Adv. Funct. Mater.* **2017**, 1700860, 1–8.
- (43) Wright, A. D.; Verdi, C.; Milot, R. L.; Eperon, G. E.; Pérez-Osorio, M. A.; Snaith, H. J.; Giustino, F.; Johnston, M. B.; Herz, L. M. Electron–Phonon Coupling in Hybrid Lead Halide Perovskites. *Nat. Commun.* **2016**, 7, 11755.
- (44) Miller, E. M.; Zhao, Y.; Mercado, C. C.; Saha, S. K.; Luther, J. M.; Zhu, K.; Stevanović, V.; Perkins, C. L.; Van De Lagemaat, J. Substrate-Controlled Band Positions in CH₃NH₃PbI₃perovskite Films. *Phys. Chem. Chem. Phys.* **2014**, 16, 22122–22130.
- (45) Domanski, K.; Roose, B.; Matsui, T.; Saliba, M.; Turren-Cruz, S. H.; Correa-Baena, J.

Chapter 3

- P.; Carmona, C. R.; Richardson, G.; Foster, J. M.; De Angelis, F.; et al. Migration of Cations Induces Reversible Performance Losses over Day/Night Cycling in Perovskite Solar Cells. *Energy Environ. Sci.* **2017**, *10*, 604–613.
- (46) Correa-Baena, J.-P.; Luo, Y.; Brenner, T. M.; Snaider, J.; Sun, S.; Li, X.; Jensen, M. A.; Hartono, N. T. P.; Nienhaus, L.; Wieghold, S.; et al. Homogenized Halides and Alkali Cation Segregation in Alloyed Organic-Inorganic Perovskites. *Science*. **2019**, *363*, 627–631.
- (47) Ball, J. M.; Petrozza, A. Defects in Perovskite-Halides and Their Effects in Solar Cells. *Nat. Energy* **2016**, *1*, 16149.

Appendices

Experimental Methods

Sample preparation.

Lead iodide and lead bromide were purchased from TCI, organic cations were purchased from Dyesol, and Cesium iodide were obtained from Alfa Aesar. Triple-cation pure iodide ($\text{Cs}_{0.06}\text{MA}_{0.15}\text{FA}_{0.79}\text{Pb}(\text{I})_3$) and pure bromide ($\text{Cs}_{0.06}\text{MA}_{0.15}\text{FA}_{0.79}\text{Pb}(\text{Br})_3$) perovskite precursor solutions were prepared by using PbI_2 (1.32 M), formamidinium iodide (1.00 M), and methylammonium iodide (0.20 M) for the pure iodide solution, and PbBr_2 (1.32 M), formamidinium bromide (1 M), and methylammonium bromide (0.20 M) for the pure bromide solution. The precursors were dissolved in a mixture of anhydrous DMF:DMSO (4:1 volume ratio, v:v) followed by addition of 5 vol% from CsI stock solution (1.5 M in DMSO) to each solution. The series of mixed halide compositions ($\text{Cs}_{0.06}\text{MA}_{0.15}\text{FA}_{0.79}\text{Pb}(\text{I}_{1-x}\text{Br}_x)_3$ $0 \leq x \leq 1$) were then made from mixing the pure iodide and pure bromide solutions in different volume fractions. Quartz substrates were cleaned by sonication in Acetone and Isopropyl Alcohol for 30 min, and further cleaning with oxygen plasma treatment for 10 min. For deposition of the perovskite solutions, we used a two-step spin-coating program at 1,000 and 4,000 rpm for 10 and 30 s respectively, and 110 μl of chlorobenzene was poured on the spinning substrate 30 s after the starting of the program. The substrates were then annealed for 1 hour at 100°C. Synthesis and deposition of perovskite solutions were performed inside a Nitrogen glove box under moisture- and oxygen-controlled conditions (H_2O level: <1 ppm and O_2 level: <10 ppm).

Chapter 3 Appendices

Time-Resolved Microwave Conductivity (TRMC).

The TRMC technique monitors the change in reflected microwave power by the excited free charge-carriers in the samples loaded in a microwave open cell upon pulsed laser excitation.

The illumination spot of the laser pulsed covers nearly the whole area of the sample (2 cm²).

The photo-conductance (ΔG) of the samples was deduced from the measured laser-induced change in normalized microwave power ($\Delta P/P$) by

$$-K\Delta G(t) = \frac{\Delta P(t)}{P} \quad (1)$$

where K is the sensitivity factor. The yield of generated free charges φ and mobility

$\sum \mu = (\mu_e + \mu_h)$ were obtained by:

$$\varphi \sum \mu = \frac{\Delta G}{I_0 \beta e F_A} \quad (2)$$

where, I_0 is the number of photons per pulse per unit area, β is a geometry constant of the microwave cell, e is the elementary charge, and F_A is the fraction of light absorbed by the sample at the excitation wavelength of 500 nm is 0.8.

Photoluminescence characterization.

Fluorescence spectra was measured in a Nitrogen filled chamber using a 532-nm continuous-wave laser at an illumination intensity of ~60 mW/cm². Light soaking of the samples was carried out by the same laser at the same intensity. We used an optical fiber coupled to an Ocean Optics Maya2000 Pro spectrometer to collect the emitted photoluminescence.

Absorption Spectra.

Absorption spectra were recorded with a Lambda 1050 UV/Vis/NIR (PerkinElmer, Inc., Shelton, CT USA) spectrophotometer, using an integrated sphere. The percentage of absorbed

light was determined from the percentage of reflected light and transmitted light by the MHP films.

Photothermal Deflection Spectroscopy (PDS).

PDS is a highly sensitive surface averaged optical absorption measurement technique. PDS is capable of measuring 5-6 orders of magnitude weaker absorbance than the band edge absorption. For the measurements, a monochromatic pump light beam is shined on the sample (film on quartz substrate), which on absorption produces a thermal gradient near the sample surface via non-radiative relaxation induced heating. This results in a refractive index gradient in the area surrounding the sample surface (the sample is immersed in a Fluorinert FC-72 high refractive index gradient inert liquid). A fixed wavelength CW laser probe beam is passed through this refractive index gradient producing a deflection proportional to the absorbed light at that particular wavelength, which is detected by a photo-diode and lock-in amplifier. Scanning through different wavelengths provides a complete absorption spectrum. For PDS measurements, the perovskite films were deposited on quartz substrates and measure before and after white light treatment with the intensity of approximately 1 sun in nitrogen.

TRMC fitting equations

$$\frac{d\Delta n}{dt} = G_c - k_2\Delta n(\Delta p + p_0) - k_T\Delta n(N_T - n_t) - k_s\Delta n + k_r n_{ts} \quad (\text{S1})$$

$$\frac{d\Delta p}{dt} = G_c - k_2\Delta n(\Delta p + p_0) - k_D n_t(\Delta p + p_0) \quad (\text{S2})$$

$$\frac{dn_t}{dt} = k_T\Delta n(N_T - n_t) - k_D n_t(\Delta p + p_0) \quad (\text{S3})$$

$$\frac{dn_{ts}}{dt} = k_s\Delta n - k_r n_{ts} \quad (\text{S4})$$

In this set of equations, the G_c is the optical generation of charge carriers; Δn , Δp , n_t and n_{ts} represent the concentrations of photo-excited electrons in the conduction band, holes in the

Chapter 3 Appendices

valence band, electrons trapped in the deep traps, and electrons stay in the shallow states, respectively; p_0 stands for the concentration of background holes, and N_T denotes the density of deep traps.

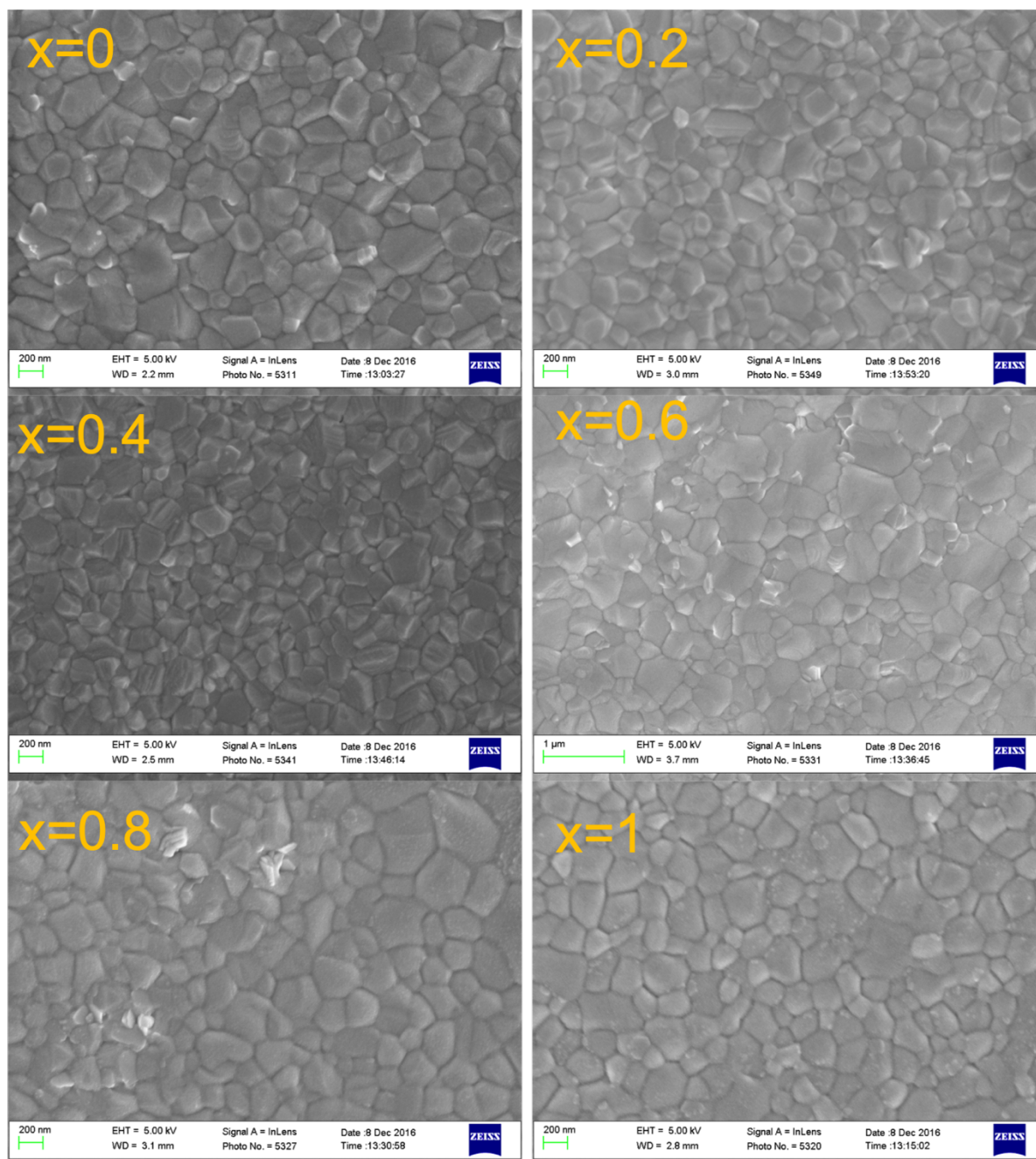


Figure S1. SEM images of $(\text{FA}_{0.79}\text{MA}_{0.16}\text{Cs}_{0.05})\text{Pb}(\text{I}_{1-x}\text{Br}_x)_3$ perovskites.

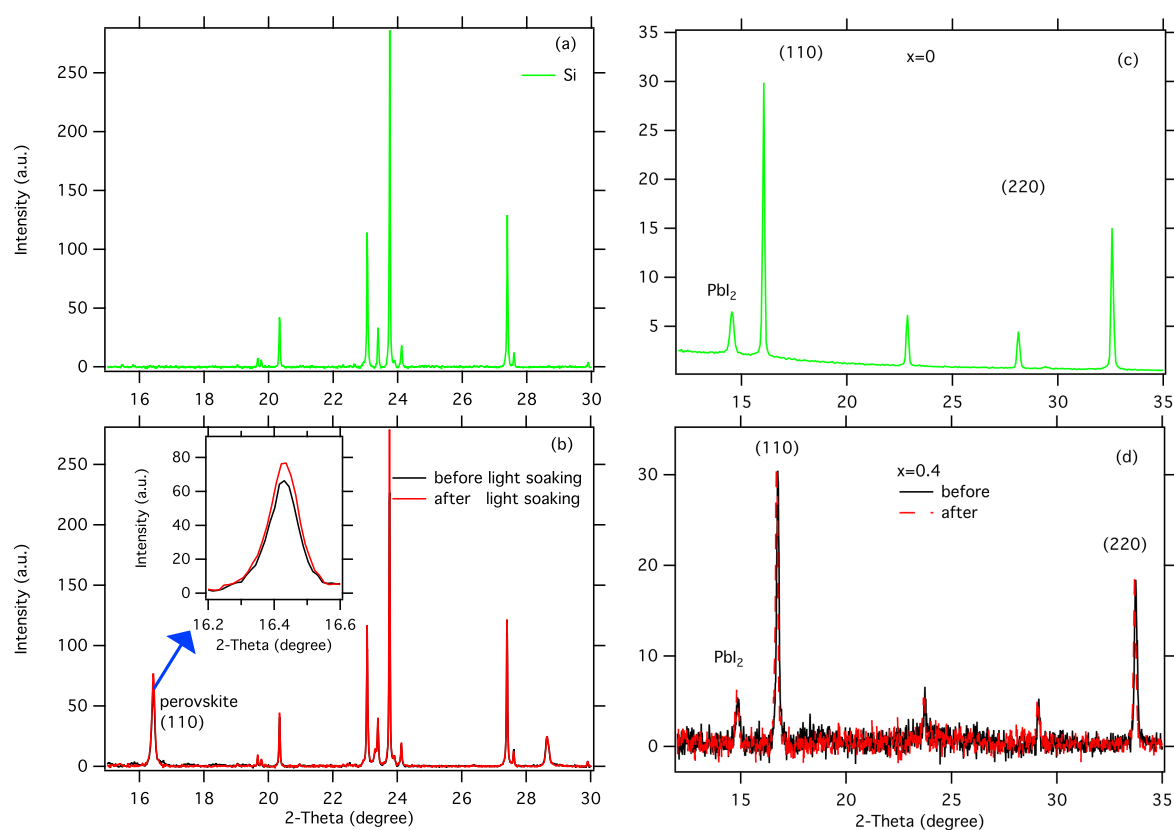


Figure S2. XRD patterns in normal 2θ plot. (a) Si (111) wafer as reference (b) $x=0.4$ before (black) and after (red) light soaking. The (110) of the perovskite is marked. Insert: zoom-in for the selected peaks. Note that the pattern after light soaking in (b) is offset to the bare Si pattern in (a) to eliminate artificial influence from the measurement. (c) and (d) were measured for $x=0$ and $x=0.4$ without reference of Si wafer. The peak of PbI_2 is also shown. Note that the XRD source for $x=0.4$ is $\text{Co K}\alpha$, $\lambda = 1.79\text{\AA}$. The $x=0$ was measured with $\text{Cu K}\alpha$, $\lambda = 1.54\text{\AA}$, hence the 2θ of graph c is recalculated by the Bragg's law.

Chapter 3 Appendices

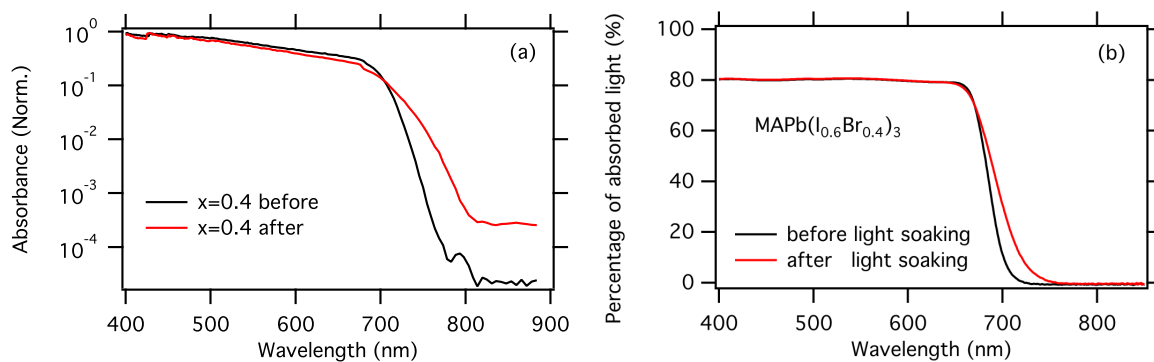


Figure S3. (a) PDS spectra of $(\text{FA}_{0.79}\text{MA}_{0.15}\text{Cs}_{0.06})\text{Pb}(\text{I}_{1-x}\text{Br}_x)_3$ with $x = 0.4$ before and after light soaking in N_2 (b)Percentage of absorbed light before and after light soaking in N_2 for $\text{MAPb}(\text{I}_{0.6}\text{Br}_{0.4})_3$.

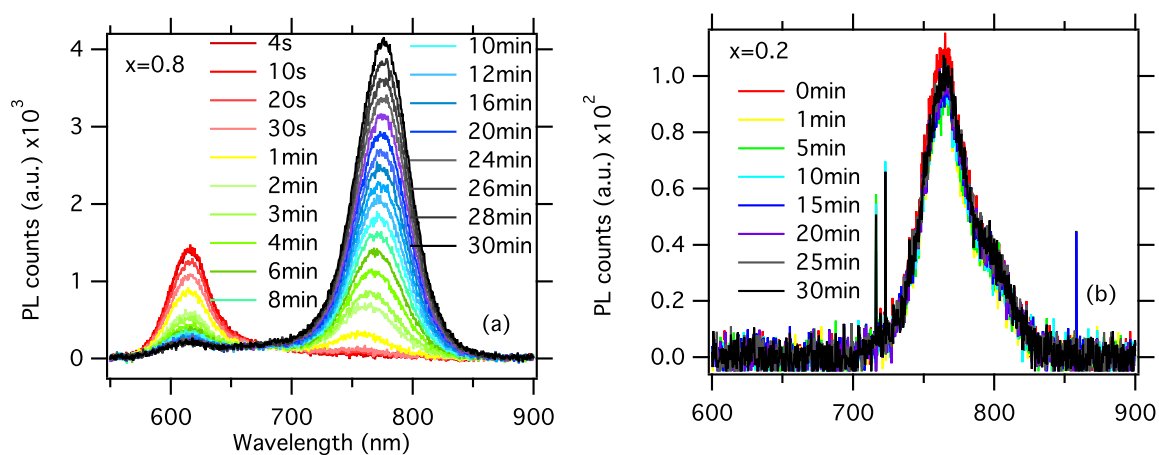


Figure S4. PL on light soaking in N_2 of the sample (a) $x=0.8$, and (d) $x=0.2$, respectively.

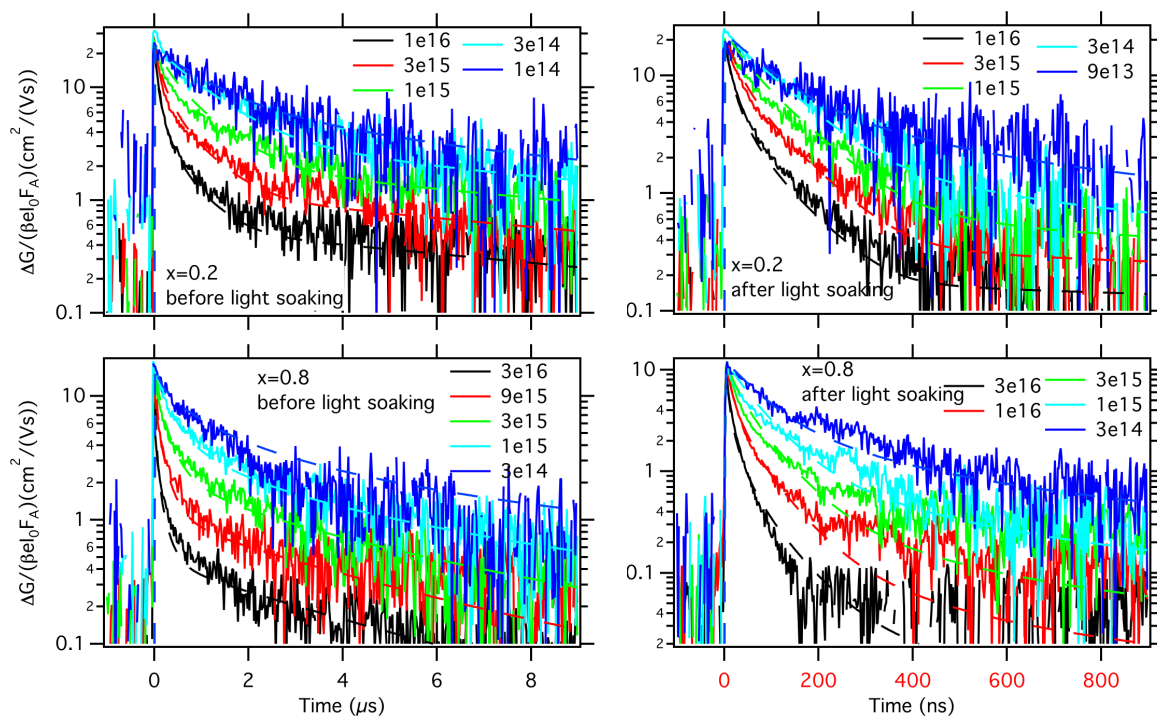


Figure S5. TRMC traces of $(\text{FA}_{0.79}\text{MA}_{0.16}\text{Cs}_{0.05})\text{Pb}(\text{I}_{1-x}\text{Br}_x)_3$ perovskites for $x=0.2$ and $x=0.8$, respectively before (left) and after (right) light soaking.

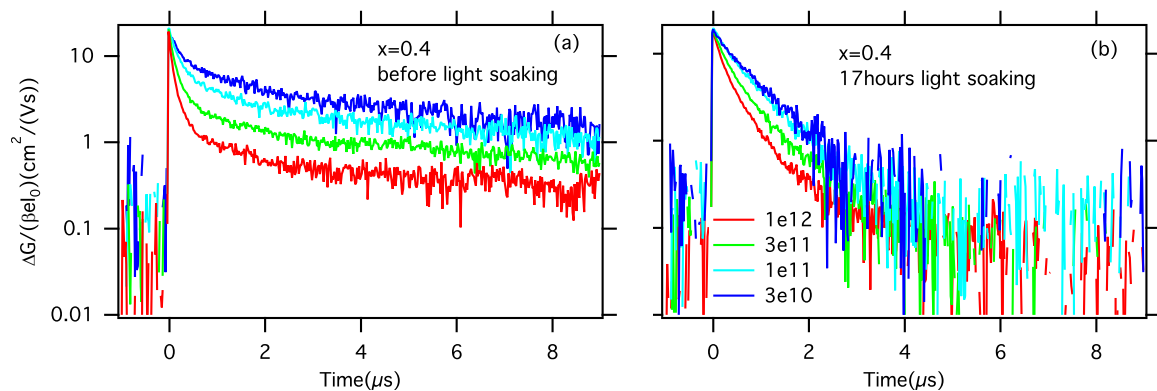


Figure S6. TRMC traces of $(\text{FA}_{0.79}\text{MA}_{0.16}\text{Cs}_{0.05})\text{Pb}(\text{I}_{0.6}\text{Br}_{0.4})_3$ before (a) and after (b) light soaking for overnight, 17 hours.

Chapter 3 Appendices

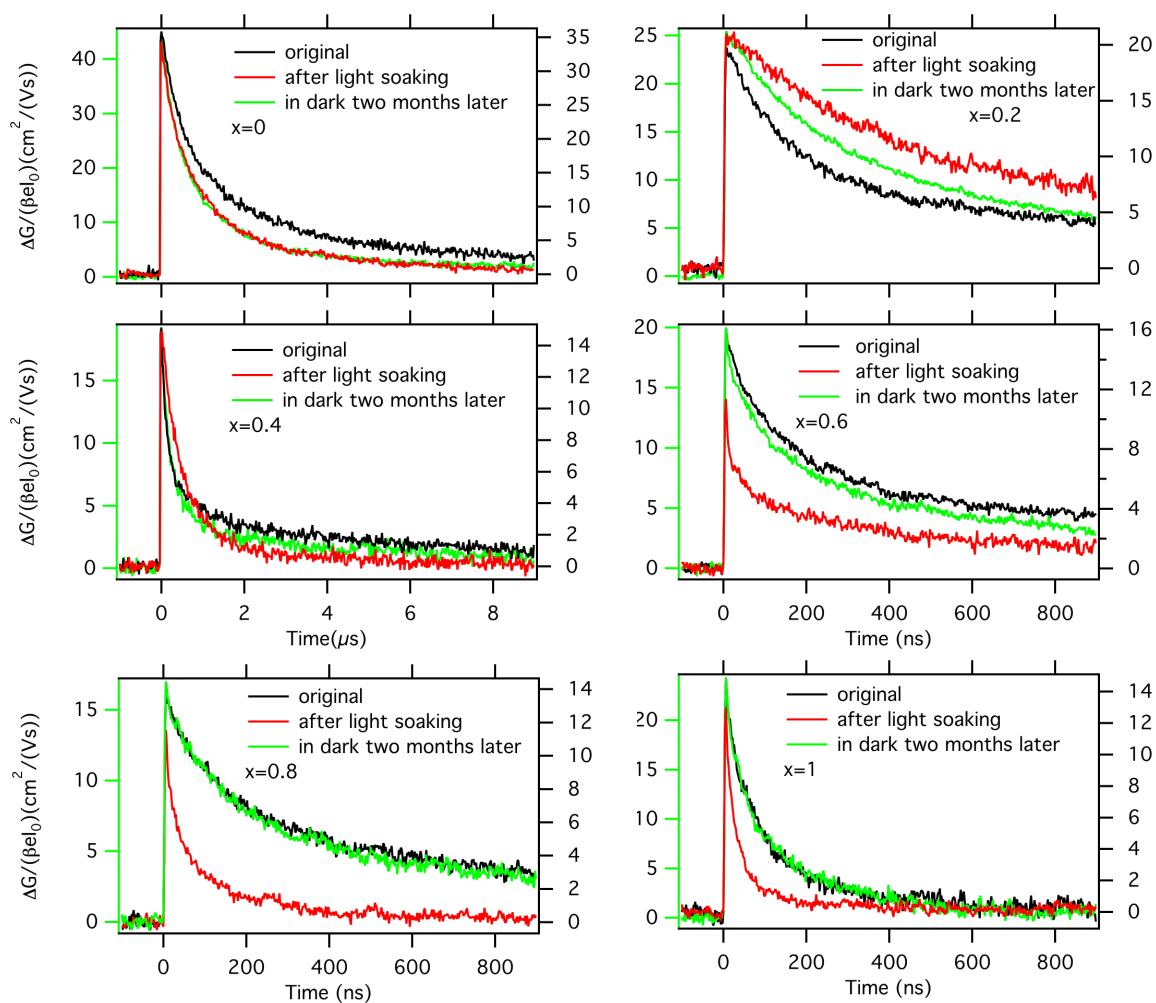


Figure S7. Recovery recorded two months later, on excitation density of $1 \times 10^{15} \text{ cm}^{-3}$. The samples were kept in a foil sealed box in a N_2 glovebox.

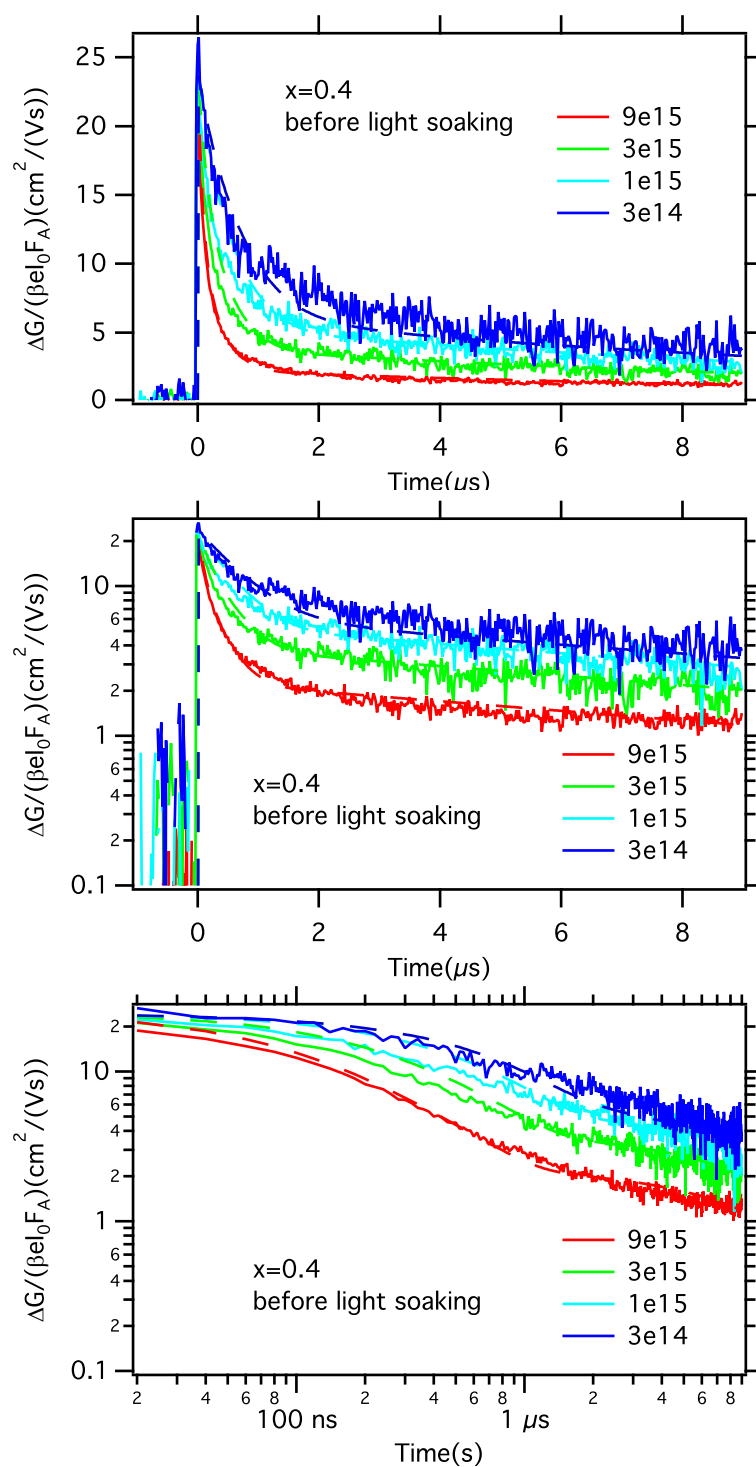


Figure S8. TRMC traces of $\text{FA}_{0.79}\text{MA}_{0.16}\text{CS}_{0.05}\text{Pb}(\text{I}_{1-0.6}\text{Br}_{0.4})_3$ on linear-linear, logarithm-linear, and logarithm-linear scale, respectively. The dashed lines are the fits from the model in Scheme 1.

Chapter 3 Appendices

Table S1. Dynamic parameters extracted from the fitting for the samples $\text{FA}_{0.79}\text{MA}_{0.16}\text{Cs}_{0.05}\text{Pb}(\text{I}_{1-0.6}\text{Br}_{0.4})_3$ from $x=0$ to $x=1$. Those of $\text{MAPb}(\text{I}_{0.6}\text{Br}_{0.4})_3$ are also included.

Head 1 [units]	x=0		x=0.2		x=0.4		x=0.6		x=0.8		x=1		MAPb(I _{0.6} Br _{0.4}) ₃	
	before	after	before	after										
$k_T^{\text{a)}$	1	1	1	1	1	1	1	1	1	1	1	1	1	1
$k_2^{\text{b)}$	4	8.5	15	9	8	7	20	40	25	69	30	30	35	30
$k_D^{\text{c)}$	3.8	4	1	1.5	1.5	3	12	16	0.4	6	4	9	0.8	0.8
$N_T^{\text{d)}$	8	11	50	50	45	48	15	15	300	300	300	300	30	120
$\rho_0^{\text{e)}$	1	1	1	1	1	1	1	1	1	1	1	1	5	50
$k_s^{\text{f)}$	6	no	20	4	70	6	80	20	80	8	no	no	no	no
$k_r^{\text{g)}$	0.6	no	10	3	8.5	5	15	2	30	3	no	no	no	no
$\mu_e^{\text{h)}$	22	22	12	12	12	12	10	5	10	6	11	7	2	2
$\mu_p^{\text{i)}$	44	44	24	24	24	24	20	10	20	12	22	14	5	5

^{a)}Deep trap filling rate ($\times 10^{-7} \text{ cm}^3\text{s}^{-1}$); ^{b)} band-to-band recombination rate ($\times 10^{-10} \text{ cm}^3\text{s}^{-1}$); ^{c)}

Deep trap depopulation rate ($\times 10^{-8} \text{ cm}^3\text{s}^{-1}$); ^{d)} Density of deep traps ($\times 10^{12} \text{ cm}^{-3}$); ^{e)} background

concentration of holes ($\times 10^{12} \text{ cm}^{-3}$); ^{f)} rate of trapping into the shallow states ($\times 10^4 \text{ s}^{-1}$); ^{g)} rate

of escaping from the shallow states ($\times 10^4 \text{ s}^{-1}$); ^{h)} mobility of electrons ($\text{cm}^2\text{V}^{-1}\text{s}^{-1}$); ⁱ⁾ mobility of

holes ($\text{cm}^2\text{V}^{-1}\text{s}^{-1}$).

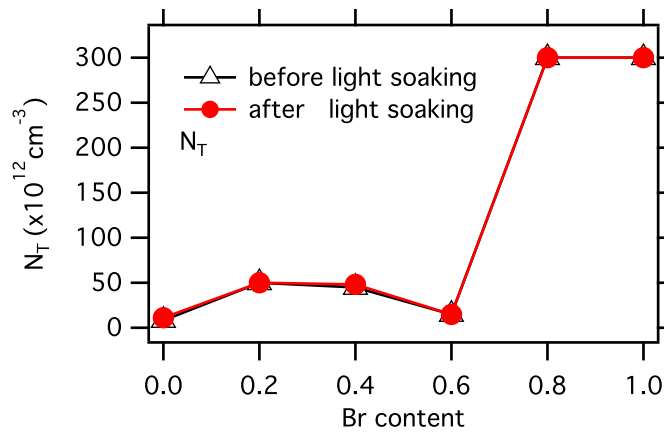


Figure S9. Density of deep trap states before (black) and after (red) light soaking, obtained from fitting.

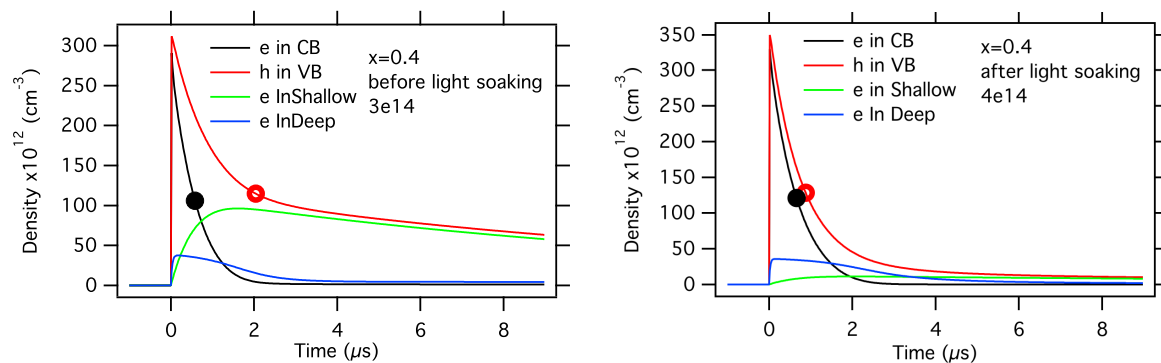
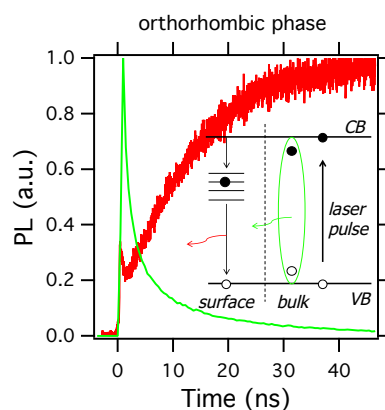


Figure S10. Decay of electrons and holes, respectively, before(left) and after(right) light soaking for $x=0.4$. The excitation density is $3 \times 10^{14} \text{ cm}^{-3}$. The green and blue lines represent how long electrons stay in shallow and deep states, respectively. The respective decay is obtained by plotting the equations (s1) and (s2) from the fitting model, and the equations (s3) and (s4) offer the staying information of the electrons in deep and shallow states, respectively. The black full dots are $1/e$ lifetime of electrons and red hollow circles are $1/e$ lifetime of holes.

Chapter 3 Appendices

Chapter 4 Photoluminescence from Radiative Surface States and Excitons in Methylammonium Lead Bromide Perovskites



This part has been published:

Guo, D.; Bartesaghi, D.; Wei, H.; Hutter, E. M.; Huang, J.; Savenije, T. J. Photoluminescence from Radiative Surface States and Excitons in Methylammonium Lead Bromide Perovskites. *J. Phys. Chem. Lett.* **2017**, *8*, 4258–4263.

Chapter 4

ABSTRACT

In view of its bandgap of 2.2 eV and its stability, methylammonium lead bromide (MAPbBr₃) is a possible candidate to serve as a light absorber in a subcell of a multi junction solar cell. Using complementary temperature-dependent time-resolved microwave conductance (TRMC) and photoluminescence (TRPL) measurements, we demonstrate that the exciton yield increases with lower temperature at the expense of the charge carrier generation yield. The low energy emission at around 580 nm in the cubic phase and the second broad emission peak at 622 nm in the orthorhombic phase originate from radiative recombination of charges trapped in defects with mobile countercharges. We present a kinetic model describing both the decay in conductance as well as the slow ingrowth of the TRPL. Knowledge of defect states at the surface of various crystal phases is of interest to reach higher open circuit voltages in MAPbBr₃ based cells.

INTRODUCTION

The past years have seen a huge increase in the power conversion efficiency of metal halide perovskite-based solar cells going from 3.8%¹ to 22.1%.² The 2.2 eV bandgap³ makes methylammonium lead bromide (MAPbBr₃) a possible candidate to serve as photoactive layer in a top cell of a multijunction solar cell.⁴ The present record efficiency of a perovskite/Si tandem cell amounts to 23.6%(monolithic tandem)⁵ and 26.4% (mechanically-stacked tandem)⁶, and is expected to reach efficiencies exceeding 30%. Open circuit voltages^{3,7-15} (V_{OC}) of 1.5 V^{8,15} have been demonstrated for single junction solar cells based on MAPbBr₃, and the best

efficiency reported amounts to 11.4%.¹⁰ However, this V_{OC} is still ca 0.3 V lower than possible on basis of its bandgap.

Therefore, to transform MAPbBr₃ into a valuable solar energy material for a multi-junction subcell, the photovoltaic properties should be improved. To this end more insight into the generation and recombination dynamics of free charges in MAPbBr₃ is essential. From absorption spectra recorded at different temperatures¹⁴, an excitonic contribution has been observed throughout the three different crystal phases¹⁶ of MAPbBr₃, for which an exciton binding energy (E_{ex}) of 40 meV was extracted.¹⁷ However, a smaller E_{ex} of 15 meV is reported by Tilchin et al. obtained by microphotoluminescence.¹⁸ In addition, MAPbBr₃ has also been studied by magneto-absorption¹⁹ yielding an E_{ex} of 25 meV.²⁰ Considering that these values are close to thermal energy at room temperature and somewhat larger than reported for MAPbI₃^{17,21} optical excitation might yield excitons at the cost of charge carriers. Temperature dependent current voltage characteristics show that for the performance of solar cells based on MAPbBr₃, not only Shockley-Read–Hall (SRH) recombination, but also surface recombination plays a crucial role.⁹ Transient reflectance spectroscopy has been used to obtain the surface recombination velocity of MAPbBr₃, and the results suggest that the minimum domain size required to avoid the influence of surface recombination is 30 μm .²² Hence, apart from losses due to exciton formation, Shockley-Read-Hall and surface recombination lead to rapid decay of charge carriers and are presumably the main reasons limiting the V_{OC} and hence the photovoltaic performance of MAPbBr₃ derived solar cells.^{9,23}

So far, no specific research on the dynamics of mobile carrier generation in the three phases of MAPbBr₃ is performed. In this work we carried out complementary temperature-dependent photo-induced time-resolved microwave

Chapter 4

conductance (TRMC) and time-resolved photoluminescence (TRPL) measurements. With TRMC, only excess free mobile charges are detected (see for more details SI), while TRPL yields information on both radiative recombination of free charges and radiative decay of excitons. Hence, the combination of TRMC and TRPL offers a full view on the generation and decay of excitons and charge carriers in MAPbBr₃. For our study, we selected MAPbBr₃ single crystals, to eliminate the effects of grain boundaries and have a well-defined surface instead.^{22,24–27} From temperature-dependent single crystal X-ray diffraction studies²⁸ it is inferred that the transition from orthorhombic to tetragonal occurs at 144.5 K and from tetragonal to cubic at 236.9 K.^{16,28} By combining information from TRPL and TRMC and additional modelling we conclude that the low energy emission in the cubic phase and in the orthorhombic phase originate from radiative recombination of charges trapped at surface defects with mobile counter charges. From this work it turns out that charges mainly decay via defect states, indicating that the wider band-gap of MAPbBr₃ contains far more states in the forbidden band-gap than MAPbI₃.

RESULTS AND DISCUSSION

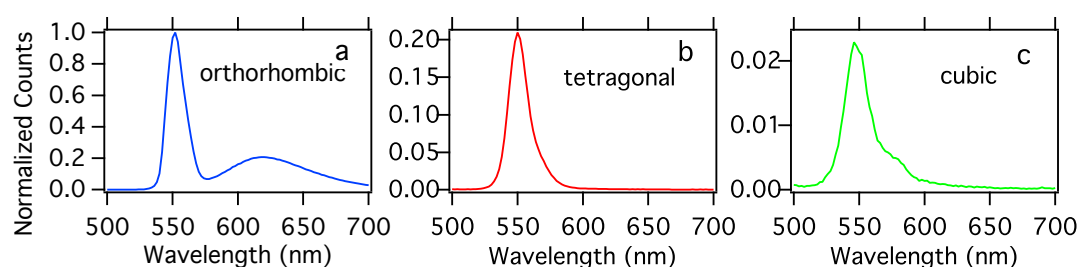


Figure 4. 1. PL emission spectra of MAPbBr₃ single crystal recorded at (a) 77 K, (b) 170 K and (c) 260 K. PL spectrum of the orthorhombic phase was normalized to unity; Other spectra are scaled by same factor.

Single crystals of MAPbBr₃ were synthesised according to previously reported methods.²⁴ A crystal of around 5×3×2 mm³ was mounted in a nitrogen-filled cryostat and illuminated using a pulsed excitation source at 405 nm. Emission spectra were recorded for different crystal phases at various indicated temperatures, see Figure 4. 1. In the cubic crystal phase, the main PL peak at 548 nm is accompanied with a shoulder located at 580 nm in line with previous reports.²⁹⁻³¹ However, even without the shoulder the PL emission is asymmetric indicating the presence of at least three components in the emission spectrum in agreement with Fang et al.³²⁻³⁴ This shoulder is not visible in the tetragonal phase. In the orthorhombic phase, two emission bands can be discerned: one at 550 nm and a second broad emission at about 620 nm. Note that even on multiple cycles of heating and cooling, this second emission peak at 620 nm only emerges in the orthorhombic phase, indicating that this feature is solely related to the orthorhombic phase. The position of the maximum of this second broad emission peak however, changes from 618 nm at 77 K to 632 nm at 110K. For thin MAPbBr₃ films similar features are observed, although relative intensities differ.(see SI, Fig S1) This low energy PL band has been observed before in metal halide perovskite films^{35,36} and single crystals,³¹ and surface defects are typically evoked to explain these type of PL peaks.^{31,35,37,38} It has been reported that the broader emission band was detected from a freshly cleaved single crystal and disappears after the crystal has been exposed to air³¹, and PL intensities and decay are subject to atmospheric conditions²⁷ We should note that in our experiments, the sample is measured and kept in N₂ atmosphere at all times.

To further investigate the origin of the photoluminescence, we measured the TRPL at the emission maximum of 550 nm, as shown in Figures 4.2a, b, and c for the orthorhombic, tetragonal and cubic crystal phases, respectively. The TRPL traces

Chapter 4

were measured at different indicated laser intensities. If the PL originates from second order band-to-band recombination, a higher density will lead to an initially faster decay. However, although the excitation densities vary by almost a factor 10, the decay traces are on top of each other in the orthorhombic and tetragonal phase. In the cubic phase, the decay becomes slower on increasing charge carrier densities, which is opposite to the trend expected for higher order recombination. Consequently, for all three phases, it seems unlikely that the TRPL originates from second order band-to-band recombination. Instead, we propose that the PL at 550 nm originates from first order radiative decay of excitons, in line with previous results.³⁹

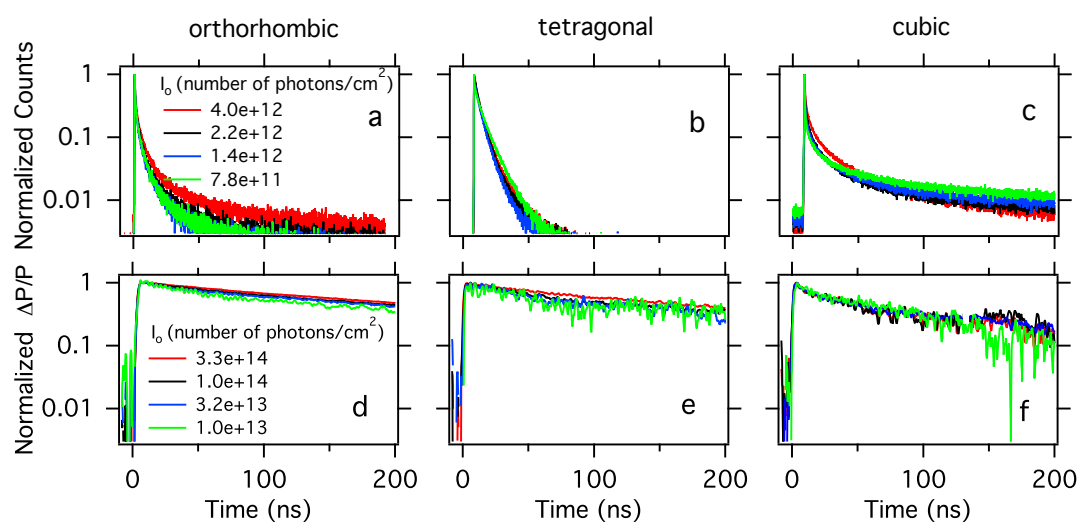


Figure 4. 2. Upper panels: Normalized TRPL of MAPbBr₃ single crystals at 550nm. Lower panels: To unity normalised photoconductance transients recorded at 500 nm. (a, d) Orthorhombic phase, T =90 K; (b, e) tetragonal phase, T =210 K; (c, f) cubic phase, T =300 K.

To unravel the degree of exciton versus mobile charge carrier formation, we performed complementary TRMC measurements on the MAPbBr₃ single crystal.

TRMC traces are recorded for the three different crystal phases on excitation at 500 nm, normalised to unity and shown in Figures 4.2d, 2e, and 2f. (See SI, Figure S4.2 for other temperatures) On laser excitation, free mobile charges are generated, leading to a fast rise of the signal. The decay of the TRMC signal represents the reduction in the concentration of free charges by recombination and/or by immobilisation in trap states. As can be observed for each phase, the TRPL decay is much faster than the TRMC decay. Besides, we see a large variation in PL decay kinetics throughout the three different phases, while this remains more or less identical in the TRMC signals. These observations suggest that the type of charge carriers responsible for the TRMC signal are not the same as those which give rise to the PL. Hence, this can be explained by assuming that part of the excitations yield excitons and only the remaining fraction is converted into free charges. To investigate how the charge carrier yield in this crystal is affected by temperature, we plotted the maximum of the photoconductance traces, which constitutes of mobility and yield of free charges (see SI Equation 2), as function of temperature and compare those to the trend of the mobility determined previously (see Figure 4. 3).⁴⁰ From here, we can conclude that the charge carrier yield gradually lowers by approximately a factor 4 in the orthorhombic phase at 140 K in comparison with the yield at room temperature. Exciton binding energies between 15 and 40 meV reported for MAPbBr₃ could well explain this fourfold reduction of the charge carrier yield. In addition, the increase in total PL yield with lowering temperatures as shown in Figure 4. 1 is in line with this. Finally, an increasing excitonic contribution in the absorption spectra of a thin film of MAPbBr₃ with lowering the temperature agrees with our findings. (See SI, Figure 4. S3)

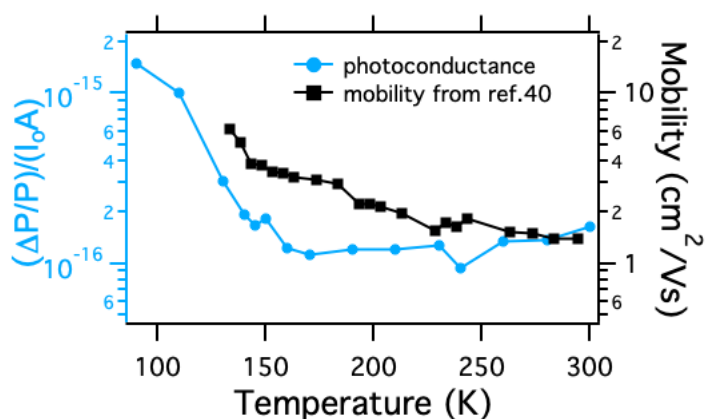


Figure 4. 3. Maximum observed values of the photoconductance corrected for the incident number of photons ($I_0 = 2.8 \times 10^{12}/\text{cm}^2$) and sample area versus temperature. Left and right axes cover both two orders of magnitude to allow comparison. The excitation wavelength is 500nm. The temperature-dependent mobility values measured by PR-TRMC are imported from the paper of Gélvez-Rueda et al.⁴⁰

On closer inspection of the TRMC data in Figure 4. 2, we notice that the normalised TRMC traces recorded with different laser intensities are on top of each other, from which it is inferred that the recombination of free charges is (pseudo-) first order. There are several explanations for this first order recombination: in case the crystal is unintentionally doped leading to a high concentration of background carriers, band-to-band recombination of excess carriers becomes pseudo-first order. This process could lead to fast PL (as shown in Figure 4.s 2a, 2b and 2c), but should then also lead to fast recombination of free charges. Since this is in contrast with the long-lived TRMC signals (Figures 4.2d, 2e and 2f), fast radiative band-to-band recombination with background carriers is unlikely. Alternatively, Shockley-Read-Hall recombination (SRH), enabled by states in the band-gap or recombination by surface defects might explain the first order decay behaviour. This is in contrast to previous research on MAPbI₃ single crystals, showing that light-induced carriers

exhibit typical band-to-band second order recombination.⁴¹ Those results indicate that single crystals of MAPbI₃ contain less defect states than their bromide counterparts.

As is shown in Figure 4. 1a, the two emission bands in the orthorhombic phase are visible having an energy difference of around 0.25 eV. The width of the emission at 622 nm suggests that it is not excitonic in nature, but originates from a manifold of energy levels within the band-gap. More specifically, in case the emission at 622 nm would be excitonic (with an exciton binding energy of 0.25 eV), this would imply that hardly any carriers would be generated on photo-excitation at low temperatures, which is not the case. Interestingly, the TRPL decay at 622 nm is much slower than that at 550 nm (see Figure 4. 4a). On combining the PL decay at 622 nm and the TRMC decay measured at corresponding excitation wavelengths and energies we observe a substantial overlap, except for the first 50 ns. This similarity on longer time scales implies that the decay of the carriers as measured by TRMC and the radiative decay as detected by PL at 622 nm have most probably the same origin. Moreover, as shown in the Figure 4. 4b, the emission at 622 nm rises relatively slowly, extending over about 40 ns. Interestingly, this rise is slower than the PL decay at 550 nm. Hence, the emission at 622 nm cannot be explained by e.g. direct reabsorption of the emission at 550 nm.

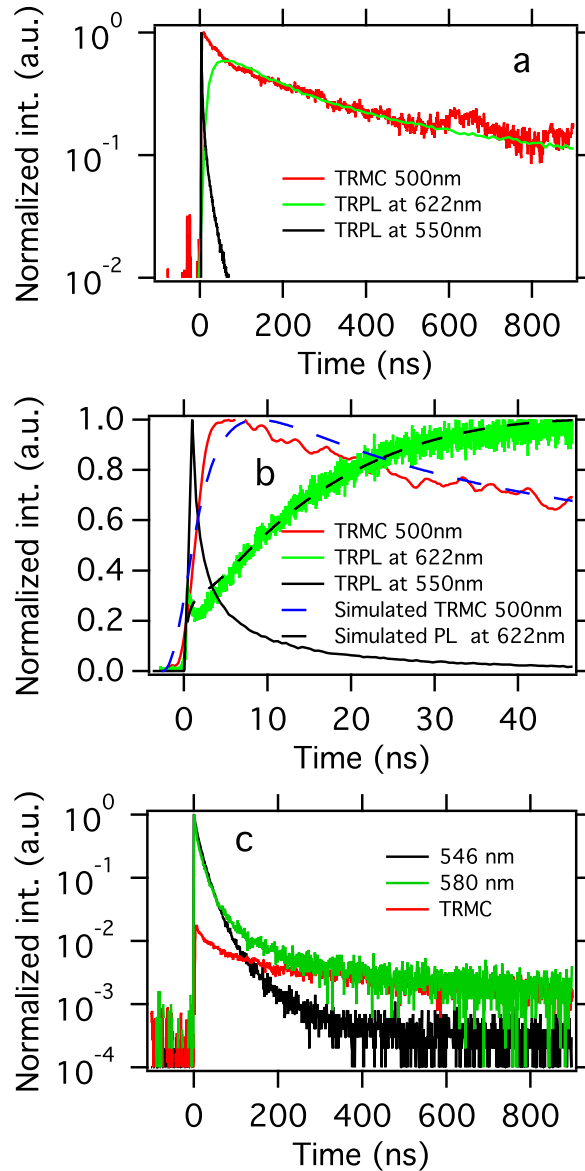


Figure 4.4. (a) Comparison of TRMC (red) and TRPL (green at 622 nm and black at 550 nm) signals at 90K, orthorhombic phase. The TRMC trace is recorded using an excitation wavelength of 500 nm, while the excitation wavelength for the TRPL is 405 nm; the incident number of photons is $10^{13}/\text{cm}^2$ and $4 \times 10^{12}/\text{cm}^2$, respectively. (b) Same traces as (a) on shorter timescales: note, the TRPL at 622 nm shows a slow 40 ns rise time. Dashed lines: calculated TRMC and TRPL by the model introduced in Scheme 4.1. (c) Comparison of TRMC (red) and TRPL (black at 546 nm and green at 580 nm) signals at 300K, cubic phase.

To explain the similarity of the TRPL signal at 622 nm and the TRMC signal at 90 K, we suggest the following model depicted in Scheme 4.1. On optical excitation, a fraction of the absorbed photons generates mobile carriers, which directly contribute to the TRMC signal. Given the relatively high absorption coefficient^{12,42} of the material at the excitation wavelengths used for both TRPL and TRMC, most of the charges are generated in proximity to the surface of the crystal. Surface states then act as a sink for conduction band electrons, which are rapidly trapped. We postulate that radiative recombination of these trapped electrons with mobile valence band holes leads to the broad 622 nm PL. We include in our model one-dimensional diffusion of charges.^{32,34} Initially, the concentration gradient causes the diffusion of charges towards the bulk of the crystal. Depletion of both mobile electrons and holes in the region close to the surface causes a local inversion of the concentration gradient, leading to diffusion of mobile charges from the bulk of the crystal towards the surface. The space and time-dependent concentrations of free electrons (n_e), free holes (n_h) and trapped electrons (n_T) are described by a set of coupled differential equations:

$$\frac{\partial n_e(x,t)}{\partial t} = D_e \frac{\partial^2 n_e(x,t)}{\partial x^2} + G(x,t) - k_{in}(x)n_e(x,t) \quad (1)$$

$$\frac{\partial n_h(x,t)}{\partial t} = D_h \frac{\partial^2 n_h(x,t)}{\partial x^2} + G(x,t) - k_{TE}(x)n_h(x,t)n_T(x,t) \quad (2)$$

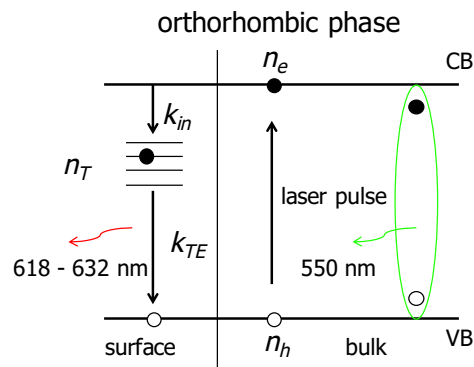
$$\frac{\partial n_T(x,t)}{\partial t} = k_{in}(x)n_e(x,t) - k_{TE}(x)n_h(x,t)n_T(x,t) \quad (3)$$

In this set of equations, x represents the distance from the surface. The generation rate of free charges, $G(x,t)$, is determined by the temporal profile and by

Chapter 4

the penetration depth of the laser pulse. As photo-recycling efficiency in MAPbBr₃ single crystals is negligible (less than 0.5%),³³ we do not take this process into account. D_e and D_h are the diffusivities of electrons and holes derived from reported mobility values,⁴³ respectively. The trapping of free electrons at the surface and the recombination of free holes with trapped electrons are governed by the rate constants $k_{in}(x)$ and $k_{TE}(x)$, respectively. Assuming that the concentration of trap states in the region close to the surface is always much larger than the concentration of free electrons, the trapping rates depends only on the concentration of free electrons; the trapping process is therefore (pseudo) first-order. On the contrary, the rate at which holes recombine with trapped electrons depends on the concentration of both species.

Based on the above kinetic model and using $k_{in} = 5 \times 10^9 \text{ s}^{-1}$ and $k_{TE} = 1 \times 10^{-11} \text{ cm}^{-3} \text{ s}^{-1}$ we simulate the TRMC and TRPL traces, as shown in Figure 4. 4b (see details in SI Simulation). The matching results suggest that due to the fast rate of trapping, excited electrons are immobilized within a few nanoseconds from the laser pulse, leading to the fast initial decay of the TRMC trace. The slow rise of the PL signal around 50 ns is the result of the slow recombination between holes and trapped electrons and the diffusion of charges towards the surface. Solving the system but neglecting the diffusional term does not yield such rise (see SI Fig. S4), suggesting that diffusion is critical for the slow ingrowth. Unfortunately, nor from our measurements nor from the modelling we can exclude that hole traps instead of electron traps lead to the observed radiation.



Scheme 4.1. Proposed kinetic model for the dynamics of charges in the orthorhombic phase. On pulsed excitation either excitons (green) or charges are formed. Electrons diffuse in all directions and are trapped at the surface with rate constant, k_{in} . Trapped electrons, n_T decay with rate constant, k_{TE} back to the valence band by emitting a photon at ca 622 nm. In principle, it is also possible that the reverse happens: Holes are trapped rapidly at the surface and decay with mobile conduction band electrons.

Next we could speculate if the shoulder of the emission band at 580 nm in the cubic phase is also due to radiative recombination of electrons trapped at the surface with valence band holes. Therefore, we measured the TRPL of the emission peak at 546 nm and at 580 nm shown in Figure 4. 4c at 300 K. Interestingly, the PL decay at 580 nm shows a long tail, which is absent in the decay taken at 546 nm in agreement with previous work.³⁹ On basis of the discussion above we might argue that the fast reducing PL is due the decaying excitons, while the tail might find its origin in luminescent decay of trapped electrons. On comparing the TRPL tail with the TRMC decay recorded in the cubic phase a striking similarity is visible, (see Figure 4. 4c) which indicates that the PL at 580 nm of the PL spectrum of the cubic phase indeed originates from radiative decay of trapped charges. Although we could not discern a slow rise of the PL at 580 nm due to the low PL intensity, a recent paper shows that

Chapter 4

also here the PL exhibits a slow rise.⁴⁴ Obviously, for the tetragonal phase there are no emissive surface defects, which could be ascribed to the fact that the trap states are above the conduction band edge or that the trapped electrons do not decay radiatively. From the results studied by density functional theory, along with photoemission and inverse photoemission spectroscopy⁴⁵, these surface states could be ascribed to bromide vacancies or lead excess, as a result of MABr termination at the surface of MAPbBr₃. In view of the similar PL spectra which we observe for thin films and single crystals we deduce that the same surface states are also present in thin MAPbBr₃ films and hence will also substantially affect the charge carrier dynamics. Since these states are related to the surface, passivation might be a viable route to improve the open circuit voltage.

In this work, we used complementary TRMC and TRPL to reveal the dynamics of photo-excited charges in the 3 crystal phases of a MAPbBr₃ single crystal. The conclusions are as follows: firstly, we find excitonic emission in each of the three phases explaining the main emission band of the PL spectra at about 550 nm. From the TRMC measurements we conclude that with lower temperature, the charge carrier yield decreases by approximately a factor of 4. In contrast to higher order band-to-band recombination observed in MAPbI₃ single crystals, in the present crystals we observe mainly first order decay, which occurs via defects. In the orthorhombic phase electrons get quickly trapped by surface defects with discrete energy levels located about 0.25 eV below the conduction band. Radiative decay of these electrons with valence band holes lead to similar TRMC and PL lifetimes. Furthermore, in the orthorhombic phase, the TRPL shows a slow rise, extending over several tens of nanoseconds. This can be explained and modelled by the period involved with transport and trapping of charges to the surface by diffusion. A similar

phenomenon could be present in the cubic phase, although the traps are much more shallow.

From this work it turns out that charges mainly decay via defect states located at the surface, indicating that the wider band-gap of MAPbBr₃ contains far more states in the forbidden band-gap than MAPbI₃. As in both MAPbBr₃ single crystals and films surface states are governing the charge carrier dynamics, these surface states are expected to also play a crucial role in devices. Passivation of these surface states is a promising method to reach higher open circuit voltages in MAPbBr₃ based cells.

REFERENCES

- (1) Kojima, A.; Teshima, K.; Shirai, Y.; Miyasaka, T. Organometal Halide Perovskites as Visible-Light Sensitizers for Photovoltaic Cells. *J. Am. Chem. Soc.* **2009**, *131*, 6050–6051.
- (2) National Renewable Energy Laboratory. Research Cell Record Efficiency Chart. <https://www.nrel.gov/pv/assets/images/efficiency-chart.png> (accessed Feb 20, 2017).
- (3) Edri, E.; Kirmayer, S.; Cahen, D.; Hodes, G. High Open-Circuit Voltage Solar Cells Based on Organic-Inorganic Lead Bromide Perovskite. *J. Phys. Chem. Lett.* **2013**, *4*, 897–902.
- (4) Polman, A.; Knight, M.; Garnett, E. C.; Ehrler, B.; Sinke, W. C. Photovoltaic Materials: Present Efficiencies and Future Challenges. *Science*. **2016**, *352*, aad4424-aad4424.

Chapter 4

- (5) Bush, K. A.; Palmstrom, A. F.; Yu, Z. J.; Boccard, M.; Cheacharoen, R.; Mailoa, J. P.; McMeekin, D. P.; Hoyer, R. L. Z.; Bailie, C. D.; Leijtens, T.; et al. 23.6%-Efficient Monolithic Perovskite/Silicon Tandem Solar Cells With Improved Stability. *Nat. Energy* **2017**, *2*, 17009.
- (6) Duong, T.; Wu, Y.; Shen, H.; Peng, J.; Fu, X.; Jacobs, D.; Wang, E. C.; Kho, T. C.; Fong, K. C.; Stocks, M.; et al. Rubidium Multication Perovskite with Optimized Bandgap for Perovskite-Silicon Tandem with over 26% Efficiency. *Adv. Energy Mater.* **2017**, *1700228*, 1–11.
- (7) Ryu, S.; Noh, J. H.; Jeon, N. J.; Chan Kim, Y.; Yang, W. S.; Seo, J.; Seok, S. II. Voltage Output of Efficient Perovskite Solar Cells with High Open-Circuit Voltage and Fill Factor. *Energy Environ. Sci.* **2014**, *7*, 2614.
- (8) Edri, E.; Kirmayer, S.; Kulbak, M.; Hodes, G.; Cahen, D. Chloride Inclusion and Hole Transport Material Doping to Improve Methyl Ammonium Lead Bromide Perovskite-Based High Open-Circuit Voltage Solar Cells. *J. Phys. Chem. Lett.* **2014**, *5*, 429–433.
- (9) Zheng, X.; Chen, B.; Yang, M.; Wu, C.; Orler, B.; Moore, R. B.; Zhu, K.; Priya, S. The Controlling Mechanism for Potential Loss in CH₃NH₃PbBr₃ Hybrid Solar Cells. *ACS Energy Lett.* **2016**, *1*, 424–430.
- (10) Mali, S. S.; Shim, C. S.; Hong, C. K. Highly Stable and Efficient Solid-State Solar Cells Based on Methylammonium Lead Bromide (CH₃NH₃PbBr₃) Perovskite Quantum Dots. *NPG Asia Mater.* **2015**, *7*, e208.
- (11) Heo, J. H.; Song, D. H.; Im, S. H. Planar CH₃NH₃PbBr₃ Hybrid Solar Cells with 10.4% Power Conversion Efficiency, Fabricated by Controlled Crystallization in the Spin-Coating Process. *Adv. Mater.* **2014**, *26*, 8179–8183.

- (12) Sheng, R.; Ho-Baillie, A.; Huang, S.; Chen, S.; Wen, X.; Hao, X.; Green, M. A. Methylammonium Lead Bromide Perovskite-Based Solar Cells by Vapor-Assisted Deposition. *J. Phys. Chem. C* **2015**, *119*, 3545–3549.
- (13) Zhang, M.; Lyu, M.; Yu, H.; Yun, J. H.; Wang, Q.; Wang, L. Stable and Low-Cost Mesoscopic CH₃NH₃PbI₂Br Perovskite Solar Cells by Using a Thin poly(3-Hexylthiophene) Layer as a Hole Transporter. *Chem. - A Eur. J.* **2015**, *21*, 434–439.
- (14) Chen, S.; Hou, Y.; Chen, H.; Richter, M.; Guo, F.; Kahmann, S.; Tang, X.; Stubhan, T.; Zhang, H.; Li, N.; et al. Exploring the Limiting Open-Circuit Voltage and the Voltage Loss Mechanism in Planar CH₃NH₃PbBr₃ Perovskite Solar Cells. *Adv. Energy Mater.* **2016**, *6*, 1–9.
- (15) Dymshits, A.; Rotem, A.; Etgar, L. High Voltage in Hole Conductor Free Organo Metal Halide Perovskite Solar Cells. *J. Mater. Chem. A* **2014**, *2*, 20776–20781.
- (16) Chen, Q.; De Marco, N.; Yang, Y.; Song, T. Bin; Chen, C. C.; Zhao, H.; Hong, Z.; Zhou, H.; Yang, Y. Under the Spotlight: The Organic-Inorganic Hybrid Halide Perovskite for Optoelectronic Applications. *Nano Today* **2015**, *10*, 355–396.
- (17) Soufiani, A. M.; Huang, F.; Reece, P.; Sheng, R.; Ho-Baillie, A.; Green, M. A. Polaronic Exciton Binding Energy in Iodide and Bromide Organic-Inorganic Lead Halide Perovskites. *Appl. Phys. Lett.* **2015**, *107*, 0–5.
- (18) Tilchin, J.; Dirin, D. N.; Maikov, G. I.; Sashchiuk, A.; Kovalenko, M. V.; Lifshitz, E. Hydrogen-like Wannier-Mott Excitons in Single Crystal of Methylammonium Lead Bromide Perovskite. *ACS Nano* **2016**, *10*, 6363–6371.
- (19) Tanaka, K.; Takahashi, T.; Ban, T.; Kondo, T.; Uchida, K.; Miura, N. Comparative Study on the Excitons in Lead-Halide-Based Perovskite-Type Crystals CH₃NH₃PbBr₃ CH₃NH₃PbI₃. *Solid State Commun.* **2003**, *127*, 619–623.

Chapter 4

- (20) Galkowski, K.; Mitioglu, A.; Miyata, A.; Plochocka, P.; Portugall, O.; Eperon, G. E.; Wang, J. T.-W.; Stergiopoulos, T.; Stranks, S. D.; Snaith, H. J.; et al. Determination of the Exciton Binding Energy and Effective Masses for the Methylammonium and Formamidinium Lead Tri-Halide Perovskite Family. *Energy Environ. Sci.* **2015**, *9*, 962–970.
- (21) Sun, S.; Salim, T.; Mathews, N.; Duchamp, M.; Boothroyd, C.; Xing, G.; Sum, T. C.; Lam, Y. M. The Origin of High Efficiency in Low-Temperature Solution-Processable Bilayer Organometal Halide Hybrid Solar Cells. *Energy Environ. Sci.* **2014**, *7*, 399–407.
- (22) Yang, Y.; Yan, Y.; Yang, M.; Choi, S.; Zhu, K.; Luther, J. M.; Beard, M. C. Low Surface Recombination Velocity in Solution-Grown CH₃NH₃PbBr₃ Perovskite Single Crystal. *Nat. Commun.* **2015**, *6*, 7961.
- (23) Yang, Y.; Yang, M.; Li, Z.; Crisp, R.; Zhu, K.; Beard, M. C. Comparison of Recombination Dynamics in CH₃NH₃PbBr₃ and CH₃NH₃PbI₃ Perovskite Films: Influence of Exciton Binding Energy. *J. Phys. Chem. Lett.* **2015**, *6*, 4688–4692.
- (24) Fang, Y.; Dong, Q.; Shao, Y.; Yuan, Y.; Huang, J. Highly Narrowband Perovskite Single-Crystal Photodetectors Enabled by Surface-Charge Recombination. *Nat. Photonics* **2015**, *9*, 679–686.
- (25) Shi, D.; Adinolfi, V.; Comin, R.; Yuan, M.; Alarousu, E.; Buin, A.; Chen, Y.; Hoogland, S.; Rothenberger, A.; Katsiev, K.; et al. Low Trap-State Density and Long Carrier Diffusion in Organolead Trihalide Perovskite Single Crystals. *Science*. **2015**, *347*, 519–522.
- (26) Saidaminov, M. I.; Abdelhady, A. L.; Murali, B.; Alarousu, E.; Burlakov, V. M.; Peng, W.; Dursun, I.; Wang, L.; He, Y.; Maculan, G.; et al. High-Quality Bulk

Hybrid Perovskite Single Crystals within Minutes by Inverse Temperature

Crystallization. *Nat. Commun.* **2015**, *6*, 7586.

(27) Fang, H.-H.; Adjokatse, S.; Wei, H.; Yang, J.; Blake, G. R.; Huang, J.; Even, J.; Loi, M. A. Ultrahigh Sensitivity of Methylammonium Lead Tribromide Perovskite Single Crystals to Environmental Gases. *Sci. Adv.* **2016**, *2*, e1600534–e1600534.

(28) Stoumpos, C. C.; Malliakas, C. D.; Kanatzidis, M. G. Semiconducting Tin and Lead Iodide Perovskites with Organic Cations: Phase Transitions, High Mobilities, and near-Infrared Photoluminescent Properties. *Inorg. Chem.* **2013**, *52*, 9019–9038.

(29) Rao, H.-S.; Chen, B.-X.; Wang, X.-D.; Kuang, D.-B.; Su, C.-Y. Micron-Scale Laminar MAPbBr₃ Single Crystal for Efficient and Stable Perovskite Solar Cell. *Chem. Commun.* **2017**, 1–4.

(30) Kanemitsu, Y. Luminescence Spectroscopy of Lead-Halide Perovskites: Materials Properties and Application as Photovoltaic Devices. *J. Mater. Chem. C* **2017**, *5*, 3427–3437.

(31) Niesner, D.; Schuster, O.; Wilhelm, M.; Levchuk, I.; Osvet, A.; Shrestha, S.; Batentschuk, M.; Brabec, C.; Fauster, T. Temperature-Dependent Optical Spectra of Single-Crystal (CH₃NH₃)PbBr₃ Cleaved in Ultrahigh Vacuum. *Phys. Rev. B* **2017**, *95*, 1–6.

(32) Yamada, T.; Yamada, Y.; Nishimura, H.; Nakaike, Y.; Wakamiya, A.; Murata, Y.; Kanemitsu, Y. Fast Free-Carrier Diffusion in CH₃NH₃PbBr₃ Single Crystals Revealed by Time-Resolved One- and Two-Photon Excitation Photoluminescence Spectroscopy. *Adv. Electron. Mater.* **2016**, *2*, 1500290.

(33) Fang, Y.; Wei, H.; Dong, Q.; Huang, J. Quantification of Re-Absorption and Re-Emission Processes to Determine Photon Recycling Efficiency in Perovskite Single Crystals. *Nat. Commun.* **2017**, *8*, 14417.

Chapter 4

- (34) Yamada, T.; Yamada, Y.; Nakaike, Y.; Wakamiya, A.; Kanemitsu, Y. Photon Emission and Reabsorption Processes in CH₃NH₃PbBr₃ Single Crystals Revealed by Time-Resolved Two-Photon-Excitation Photoluminescence Microscopy. *Phys. Rev. Appl.* **2017**, *7*, 1–8.
- (35) Priante, D.; Dursun, I.; Alias, M. S.; Shi, D.; Melnikov, V. A.; Ng, T. K.; Mohammed, O. F.; Bakr, O. M.; Ooi, B. S. The Recombination Mechanisms Leading to Amplified Spontaneous Emission at the True-Green Wavelength in CH₃NH₃PbBr₃ Perovskites. *Appl. Phys. Lett.* **2015**, *106*, 1–5.
- (36) Motti, S. G.; Gandini, M.; Barker, A. J.; Ball, J. M.; Srimath Kandada, A. R.; Petrozza, A. Photoinduced Emissive Trap States in Lead Halide Perovskite Semiconductors. *ACS Energy Lett.* **2016**, *1*, 726–730.
- (37) Dar, M. I.; Jacopin, G.; Meloni, S.; Mattoni, A.; Arora, N.; Boziki, A.; Zakeeruddin, S. M.; Rothlisberger, U.; Graetzel, M. Origin of Unusual Bandgap Shift and Dual Emission in Organic-Inorganic Lead Halide Perovskites. *Sci. Adv.* **2016**, *2*, e1601156–e1601156.
- (38) Fang, X.; Zhang, K.; Li, Y.; Yao, L.; Zhang, Y.; Wang, Y.; Zhai, W.; Tao, L.; Du, H.; Ran, G. Effect of Excess PbBr₂ on Photoluminescence Spectra of CH₃NH₃PbBr₃ Perovskite Particles at Room Temperature. *Appl. Phys. Lett.* **2016**, *108*, 1–5.
- (39) He, H.; Yu, Q.; Li, H.; Li, J.; Si, J.; Jin, Y.; Wang, N.; Wang, J.; He, J.; Wang, X.; et al. Exciton Localization in Solution-Processed Organolead Trihalide Perovskites. *Nat. Commun.* **2016**, *7*, 10896.
- (40) Gélvez-Rueda, M.; Cao, D. H.; Patwardhan, S.; Renaud, N.; Stoumpos, C. C.; Schatz, G. C.; Hupp, J. T.; Farha, O. K.; Savenije, T. J.; Kanatzidis, M. G.; et al.

Effect of Cation Rotation on Charge Dynamics in Hybrid Lead Halide Perovskites. *J. Phys. Chem. C* **2016**, *120*, 16577–16585.

(41) Bi, Y.; Hutter, E. M.; Fang, Y.; Dong, Q.; Huang, J.; Savenije, T. J. Charge Carrier Lifetimes Exceeding 15 Ms in Methylammonium Lead Iodide Single Crystals. *J. Phys. Chem. Lett.* **2016**, *7*, 923–928.

(42) Hoke, E. T.; Slotcavage, D. J.; Dohner, E. R.; Bowring, A. R.; Karunadasa, H. I.; McGehee, M. D. Reversible Photo-Induced Trap Formation in Mixed-Halide Hybrid Perovskites for Photovoltaics. *Chem. Sci.* **2015**, *6*, 613–617.

(43) Shi, D.; Adinolfi, V.; Comin, R.; Yuan, M.; Alarousu, E.; Buin, A.; Chen, Y.; Hoogland, S.; Rothenberger, A.; Katsiev, K.; et al. Low Trap-State Density and Long Carrier Diffusion in Organolead Trihalide Perovskite Single Crystals. *Science*. **2015**, *347*, 519–522.

(44) Diab, H.; Arnold, C.; Lédée, F.; Trippé-Allard, G.; Delport, G.; Vilar, C.; Bretenaker, F.; Barjon, J.; Lauret, J.-S.; Deleporte, E.; et al. Impact of Reabsorption on the Emission Spectra and Recombination Dynamics of Hybrid Perovskite Single Crystals. *J. Phys. Chem. Lett.* **2017**, 2977–2983.

(45) Komesu, T.; Huang, X.; Paudel, T. R.; Losovyj, Y. B.; Zhang, X.; Schwier, E. F.; Kojima, Y.; Zheng, M.; Iwasawa, H.; Shimada, K.; et al. Surface Electronic Structure of Hybrid Organo Lead Bromide Perovskite Single Crystals. *J. Phys. Chem. C* **2016**, *120*, 21710–21715.

Appendices

Time-Resolved Microwave Conductivity (TRMC)

In TRMC we use laser pulses to excite a sample, a crystal in this study. The laser system is able to generate light of wavelengths from 240 nm to 2200 nm, and the light intensity can be tuned over 4 orders of magnitude. When microwaves pass through a sample containing mobile charges, the power of the microwaves decrease. The relationship between the normalized change in microwave power $\Delta P(t)/P$, the photoconductance ΔG , the mobility μ and the yield of free charges φ is given by equations (1) and (2):

$$\frac{\Delta P(t)}{P} = -K\Delta G(t) \quad (1)$$

$$\frac{\Delta G_{\max}}{I_0\beta eF_A} = \varphi(\mu_h + \mu_e) \quad (2)$$

where K is the so-called sensitivity factor, I_0 is the intensity of the laser in photons/pulse/unit area, F_A is the fraction of light absorbed at the excitation wavelength, β is a constant related to the inner dimensions of the waveguide. For crystals it is not straightforward to determine the K accurately. Therefore, in this study TRMC data are expressed in $\Delta P(t)/(PI_0A)$, which is still proportional to the product of the yield of free charges, φ and the mobility, μ .

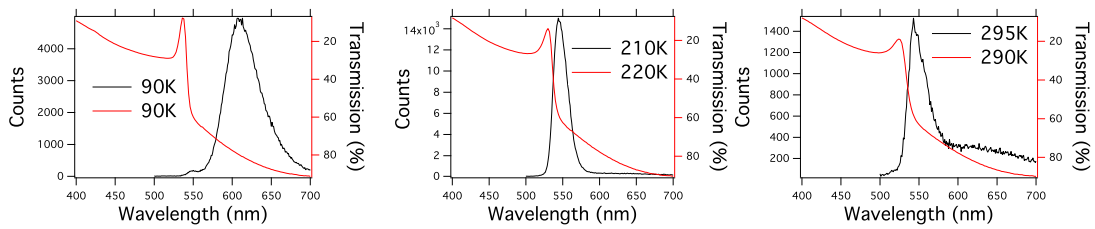


Fig. S4.4.1. PL and transmission spectra of the MAPbBr₃ thin films recorded at different temperatures. The films are made by methods shown below in Experimental methods.

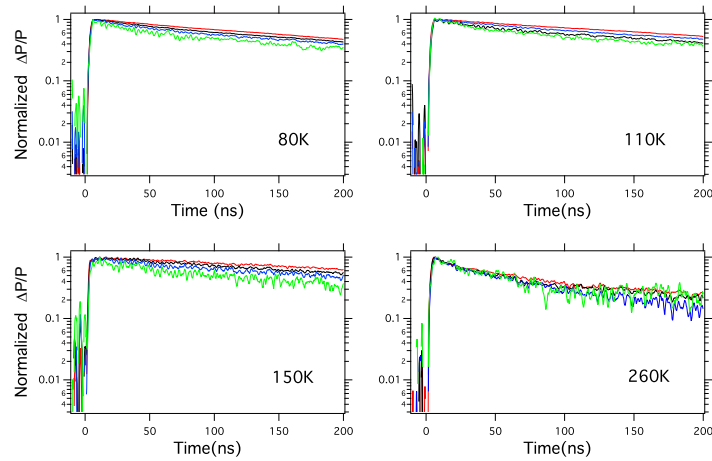


Fig. S4.2. TRMC traces recorded at 500 nm at other temperatures.

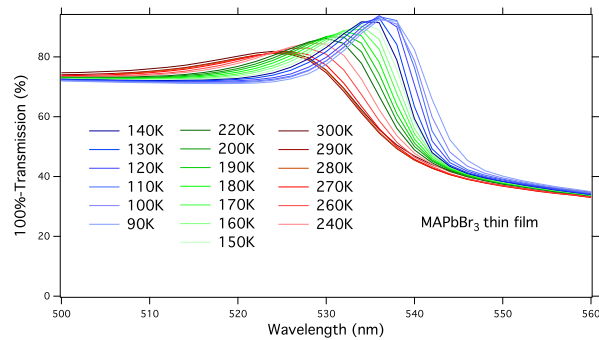


Fig. S4.3. The temperature dependent transmission spectra of MAPbBr₃ thin film. The three colour series represent the three phases: red is for cubic phase, green is for tetragonal phase, and blue is for orthorhombic phase.

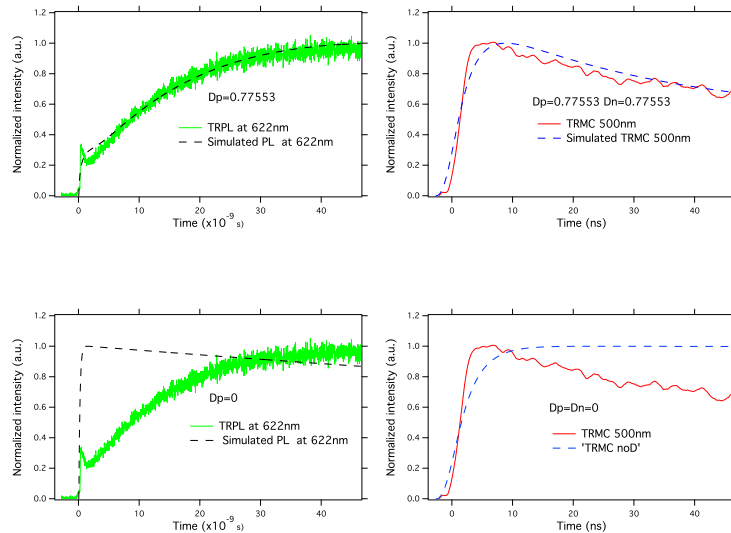


Fig. S4.4. Upper panels: Red: calculated, Black: experiments. The experimental PL data was smooth fitted before normalizing them. Lower panels: The simulation results from $D = 0$.

Chapter 4 Appendices

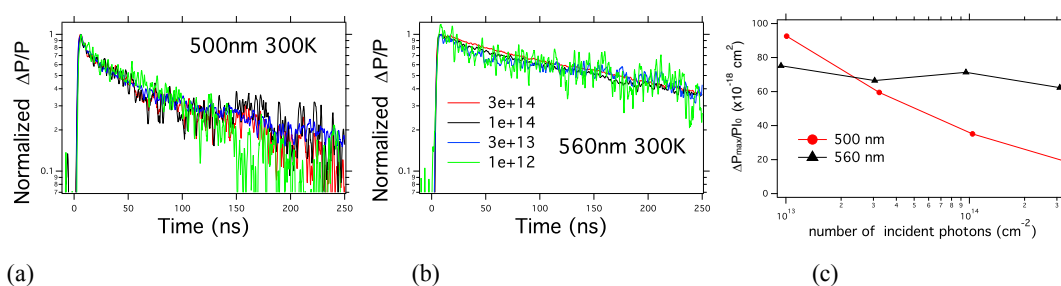


Fig. S4.5 Normalized $\Delta P/P$, recorded at 300k illuminated at 500 nm laser (a) and 560 nm laser (b) of different intensities, distinguished by colours. (c) Maxima of $\Delta P/P$ divided by incident number of photons per sample area.

In Fig. S4.5c the maxima of $\Delta P/P$ divided by incident number of photons per sample area are plotted versus the incident number of photons. As shown the maximum values at 560 nm are almost constant, while those at 500 nm decrease with increasing intensities. An obvious explanation would be the presence of second order band-to-band recombination occurring at high densities. However, this seems in conflict with the fact that the TRMC traces follow first order kinetics as presented above. Obviously, at short timescales faster than we can resolve using the present technique, other processes occur which lower the charge carrier concentration yield on higher intensities. We suggest that apart from charges also excitons might be formed on optical excitation of MAPbBr_3 . According to the Saha equation the ratio of free charges, x reduces as the concentration of excitations, n in the MAPbBr_3 single crystal significantly increases, while at the same time the yield of excitons increases. At 560 nm the excitation density is always over 1000 times lower than at 500 nm, leading at all intensities to a yield of charge carriers close to 1.

Experimental methods

Materials. Lead bromide (PbBr_2) (>98%, Sigma-Aldrich), Methylamine (CH_3NH_2) (40% w/w aq. soln., Alfa Aesar), Hydrobromic acid (HBr) (48% w/w aq. soln., Alfa Aesar), *N,N*-Dimethylformamide (DMF) (>99.8%, Alfa Aesar), Dichloromethane (DCM) (99.7%, Alfa Aesar), Dimethyl sulfoxide (DMSO) (>99.9%, Sigma-Aldrich).

Synthesis of Methylammonium bromide (MABr). MABr was prepared by slowly mixing methylamine with HBr in 1:1 molar ratio under continuous stirring at 0 °C for

2 h. MABr was then crystallized by removing the solvent from an evaporator, washing three times in diethyl ether, and filtering the precipitate. The white crystal was obtained by recrystallization with ethanol, then dried in vacuum for 24 h, and kept in a dark and dry environment for further use.

Growth of MAPbBr₃ single crystal (SC). 1.5 M PbBr₂ and 1.5 M MABr were dissolved into DMF solution in a vial to keep the molar ratio of PbBr₂ to MABr is 1. Then the solution was heated on a hot plate. Finally, MAPbBr₃ SC can slowly grow by gradually increasing the temperature of the hot plate.

Fabrication of MAPbBr₃ thin film. The MAPbBr₃ thin film was spun coated on a quartz substrate by the anti-solvent method, and the spin coating process was conducted in glovebox with oxygen level lower than 100 particles per million. The perovskite precursor solution composed of PbBr₂ and MABr (1:1, in molar) was dissolved in mixed solvent (DMF: DMSO = 9:1, v/v). Then 80 μL precursor solution was spun onto substrate at 2000 rpm for 2 s and 4000 rpm for 60 s, the sample was quickly washed with 120 μL toluene at the 20th second of the 4000 rpm spin-coating. Subsequently, the sample was annealed at 70 °C for 10 min and 100 °C for 10 min.

Photoluminescence (PL) measurements of MAPbBr₃ single crystal. We used an Edinburgh LifeSpec spectrometer equipped with a single photon counter to measure PL spectra and lifetimes. An Oxford cryostat was installed in the LifeSpec measuring chamber, and the sample was kept all the time in the inner chamber of the cryostat.

Simulation

The differential equations proposed by the model in Scheme 1 are:

$$\frac{\partial n_e(x,t)}{\partial t} = D_e \frac{\partial^2 n_e(x,t)}{\partial x^2} + G(x,t) - k_{in}(x)n_e(x,t) \quad (1)$$

$$\frac{\partial n_h(x,t)}{\partial t} = D_h \frac{\partial^2 n_h(x,t)}{\partial x^2} + G(x,t) - k_{TE}(x)n_h(x,t)n_T(x,t) \quad (2)$$

$$\frac{\partial n_T(x,t)}{\partial t} = k_{in}(x)n_e(x,t) - k_{TE}(x)n_h(x,t)n_T(x,t) \quad (3)$$

In order to consider only trapping and recombination at the surface, the rate constants $k_{in}(x)$ and $k_{TE}(x)$ are defined as step functions:

Chapter 4 Appendices

$$k_{in}(x) = \begin{cases} k_{in} & \text{for } x < x_s \\ 0 & \text{for } x > x_s \end{cases} \quad (4)$$

and

$$k_{TE}(x) = \begin{cases} k_{TE} & \text{for } x < x_s \\ 0 & \text{for } x > x_s \end{cases} \quad (5),$$

where x_s is the thickness of the region where the surface states are located.

We solved the system of equations 1 – 3 by numerical methods ¹ n_e , n_h and n_T as a function of space and time. The PL trace is calculated as

$$PL(t) = \frac{k_{TE} \int_0^{x_s} p(x,t) n_T(x,t) dx}{I_0} \quad (6).$$

The same set of equations was used for the TRMC experiment, using a different $G(x,t)$ term because of the different laser source. The change in photoconductance as a function of time is proportional to the charge carrier concentration and the charge mobilities, according to

$$\Delta G(t) \propto \int_0^L (n_e(x,t)\mu_e + n_h(x,t)\mu_h) dx \quad (7),$$

where L is the thickness of the sample and $\mu_{e(h)}$ is the mobility of electrons (holes), which is constant in time and space. After calculating ΔG , a convolution is applied to take into account the response time of the system (3 ns).²

In order to solve the system, we assumed that the mobilities of electrons and holes are equal and have a value of $100 \text{ cm}^2 \text{ V}^{-1} \text{ s}^{-1}$, similar to what reported in the literature.³ We calculated D_e and D_h from μ_e and μ_h using the Einstein relation. For both TRPL and TRMC, the generation term has a Gaussian profile in time, with 43 ps and 3.5 ns fwhm, respectively. The spatial distribution of the charge generation has an exponential shape with a penetration depth of 180 nm. We simulated a sample with thickness $L = 1 \text{ }\mu\text{m}$, considering the concentration of charges deeper in the bulk of the crystal to be negligible. The defect states are assumed to be distributed in a region with thickness $x_s = 10 \text{ nm}$. The only free parameters of the model are k_{in} and k_{TE} . Equation 6 and 7 reproduce well the experimental data for $k_{in} = 5 \times 10^9 \text{ s}^{-1}$ and $k_{TE} = 1 \times 10^{-11} \text{ cm}^{-3} \text{ s}^{-1}$ (Figure 4.4b)

REFERENCES

- (1) Crank, J.; Nicolson, P. A Practical Method for Numerical Evaluation of Solutions of Partial Differential Equations of the Heat-Conduction Type. *Math. Proc. Cambridge Philos. Soc.* **1947**, *43*, 50–67.
- (2) Savenije, T. J.; Ferguson, A. J.; Kopidakis, N.; Rumbles, G. Revealing the Dynamics of Charge Carriers in Polymer:fullerene Blends Using Photoinduced Time-Resolved Microwave Conductivity. *J. Phys. Chem. C* **2013**, *117*, 24085–24103.
- (3) Shi, D.; Adinolfi, V.; Comin, R.; Yuan, M.; Alarousu, E.; Buin, A.; Chen, Y.; Hoogland, S.; Rothenberger, A.; Katsiev, K.; et al. Low Trap-State Density and Long Carrier Diffusion in Organolead Trihalide Perovskite Single Crystals. *Science*. **2015**, *347*, 519–522.

Chapter 4 Appendices

Chapter 5 Multi Bandgap Transitions

Revealed by Two-Photon Absorption Spectra in Metal Halide Perovskites

This part is based on:

Wei, Z; **Guo, D.**; Thieme, J; Caselli, V.; Even, j.; Savenije, T. J. Multi Bandgap Transitions Revealed by Two-Photon Absorption Spectra in Metal Halide Perovskites. Submitted, **2019**

Chapter 5

ABSTRACT

Metal halide perovskites (MHPs) have emerged as a promising family of materials for optoelectronic devices including solar cells, reaching now efficiencies exceeding 24%. Although there has been intense research into the optoelectronic properties, the sub-bandgap absorption in MHPs remains largely unexplored. Here we recorded two photon absorption (2PA) spectra of polycrystalline MHP thin films using the time-resolved microwave conductivity (TRMC) technique over a broad wavelength regime varying from $0.49E_g < \hbar\omega < E_g$. The 2PA coefficients, β were obtained by considering the quadratic relationship between the number of induced charge carriers and the incident light intensity. A two-step upward trend is observed in the 2PA spectrum for $\text{CH}_3\text{NH}_3\text{PbI}_3$, and its bromide analogue ($\text{CH}_3\text{NH}_3\text{PbBr}_3$), which indicates that the commonly used scaling law is not directly applicable to MHPs. We interpret the two-step behavior as being due to multi-bandgap transitions. The present work shows that valuable insight can be obtained in the opto-electronic properties of MHPs by sub band gap spectroscopy.

INTRODUCTION

Over the past few years, metal halide perovskites (MHPs) have attracted immense attention due to their extraordinary performance as the light absorbing layer in solar cells.^{1,2} This exciting family of semiconductors exhibits large carrier mobilities,^{3,4} long charge carrier lifetimes,^{5,6} and a linear absorption coefficient over 10^5 cm^{-1} above the bandgap.¹ Recently, appreciable nonlinear absorption coefficients (and refractive indices) have been reported rendering these materials of interest for nonlinear photonics,⁷ including two-photon-pumped lasers,^{8,9} and saturable absorption based ultrafast pulsed lasers.¹⁰ As a typical nonlinear process, two-photon absorption (2PA) features long penetration depths and a quadratic dependence on the intensity providing opportunities for bio-imaging,^{11,12} photodynamic therapy,¹³ three-dimensional optical data storage,¹⁴ and up-conversion lasing and

amplification.¹⁵ In addition, quantifying the wavelength-dependence of the 2PA process is of fundamental interest, since the 2PA can yield detailed information of the energy-band structure in crystalline solids, which may not be accessible by ordinary optical absorption spectroscopy. For example, when 1PA is forbidden by selection rules, 2PA may be allowed.

In a semiconductor the simultaneous absorption of two photons can lead to an excitation of an electron from the valence band (VB) to conduction band (CB) via a virtual state by 2PA. The generation rate of charge carriers, n_0 for the 2PA process is given by

$$\frac{dn_0}{dt} = \frac{\beta I^2}{2\hbar\omega} \quad (1)$$

Where β (cm/W) is the 2PA coefficient, I (W/cm²) the light intensity entering the sample and $\hbar\omega$ (J) the incident photon energy. Since the absorption cross section of 2PA is typically low, high intensities are required.

Despite the importance of revealing the 2PA spectrum,¹⁶ only a few studies have been devoted to the 2PA properties in MHPs performed by the Z-scan or optimized Z-scan technique yielding β differing by several orders of magnitude between different MHPs or even between the same perovskites.^{17,18,19} Furthermore, all Z-scan based measurements were performed at a single fixed wavelength. Wavelength dependent characterization was achieved by photoluminescence excitation spectroscopy, however, only up to $\hbar\omega/E_g = 0.524$.²⁰

In this work, we record the 2PA spectrum of methylammonium lead iodide perovskite (CH₃NH₃PbI₃) polycrystalline thin films using the time-resolved microwave photoconductivity (TRMC) technique. From the photoconductance induced by a nanosecond laser pulse, the initial number of photogenerated charge carriers is obtained for wavelengths ranging between 0.49 and 1 times the bandgap energy ($0.49E_g < \hbar\omega < E_g$). It has been postulated that the z scan technique is prone to overestimate the value of β ,⁷ since free carrier absorption can lead to an additional reduction of the transmitted light.²¹ Since with the TRMC technique excess charges are probed by microwaves instead of light, this problem is surmounted. A two-step upward trend for the 2PA spectrum is observed for CH₃NH₃PbI₃, which is explained by a combination of multiple bandgap transitions: a primary bandgap of 1.59 eV and a second transition of 2.27 eV. Apart from 2PA we identify sub-bandgap linear absorption (SLA) at photon energies close to the band edge. Furthermore, we investigated the impact of the

Chapter 5

tetragonal-to-orthorhombic phase transition on the 2PA coefficient, β by changing the temperature. Hence, we report, for the first time, the 2PA spectrum including its temperature-dependence of a perovskite polycrystalline film.

RESULTS AND DISCUSSION

Thin films of $\text{CH}_3\text{NH}_3\text{PbI}_3$ (~200 nm thickness) were spin-coated on quartz. The X-ray diffraction pattern (see **Figure S5.1**) of the $\text{CH}_3\text{NH}_3\text{PbI}_3$ film displays strong reflections for the $\langle 110 \rangle$ and $\langle 220 \rangle$ planes confirming the formation of highly crystalline $\text{CH}_3\text{NH}_3\text{PbI}_3$. The absorption spectrum (see **Figure S5.2**) shows a cut-off wavelength of 785 nm indicating a bandgap energy of 1.58 eV. To probe 2PA in the $\text{CH}_3\text{NH}_3\text{PbI}_3$ film, the sample was measured by the TRMC technique^{22,23} for a wide range of photon energies varying from 0.775 eV to 1.55 eV. The light intensity was attenuated by an array of neutral density filters yielding light intensities varying from $I_{N0} : 2 \times 10^{11}$ to 2×10^{15} photons/cm²/pulse. To avoid direct photoexcitation by co-generated visible light in the optical parametric oscillator (OPO), two additional high pass filters of 665nm and 630nm were used. All TRMC traces were averaged at least 200 times to minimize the inaccuracy induced by the power meter reading and variations in the laser pulses.

In **Figure S5.3** the photoconductance traces, normalized for the incident intensity, $\frac{\Delta G}{e\beta_0 I_{N0}}$ are shown for different laser intensities at a photon energy of 1.43 eV (867nm). On laser excitation the conductance increases rapidly followed by a slow decay due to recombination or immobilization of charges in trap states⁵. Interestingly, for the lower intensities the traces overlap, while at higher intensities the signal heights become substantially larger, which is opposite to those measured above the bandgap. Next, we plotted the intensity normalized maximum photoconductance values $\frac{\Delta G_{max}}{e\beta_0 I_{N0}}$ versus the incident intensity (I_{N0}) for three different photon energies in Figure 5.1a. At 1.45 eV the values of $\frac{\Delta G_{max}}{e\beta_0 I_{N0}}$ are almost constant with intensity suggesting a first order excitation process. This process is explained by the optically induced electronic transitions of electrons from the VB to sub-bandgap levels, or from the latter to the CB, as depicted in **Figure 5.1b** and denoted by sub-bandgap linear absorption (SLA). On the contrary, at 1.3 eV a clear linear dependence between $\frac{\Delta G_{max}}{e\beta_0 I_{N0}}$ and I_{N0} is observed

which implies that the conductance is proportional to I_{N0}^2 agreeing with the 2PA process. In **Figure 5.1c**, the mechanism is illustrated showing the generation of a charge carrier pair on absorbing two photons. At 1.43 eV an intermediate regime is visible: at low intensities ($I_{N0} < 2 \times 10^{14}$ photons/pulse/cm²), $\frac{\Delta G_{max}}{e\beta_0 I_{N0}}$ is almost constant. On increasing I_{N0} the signal gradually increases, demonstrating the transition from predominantly SLA to the 2PA process. The lowest detectable photon energy is found to be 0.8 eV in agreement with the energy threshold of 0.79 eV for the 2PA process. In short, the optical absorption below the bandgap by the CH₃NH₃PbI₃ film is explained as follows: in the far below-bandgap regime (0.8 - 1.4 eV), photoinduced charge carriers are predominantly generated by the 2PA process; a transition regime is found between 1.4 eV and 1.45 eV, where both SLA and 2PA are contributing to the signal; In the near band-edge regime (1.45 - 1.55 eV) only SLA was detected due to much higher densities of sub-bandgap levels compared to that in the far below-bandgap regime.

To come to the 2PA coefficient, β the concentration of initially photogenerated charge carriers (n_0) can be obtained from the maximum photoconductance (ΔG_{max}) by

$$n_0 = \frac{\Delta G_{max}}{e\Sigma\mu\beta_0 L} \quad (2)$$

Where $\Sigma\mu$ is the sum of the electron and hole mobilities, β_0 the dimensionless constant of the microwave cell and L the sample thickness. Since $\Sigma\mu$ is an intrinsic property of the sample, we have deduced this value from a TRMC measurement above the bandgap. (see **Figure S5.4**)^{23,24} Next, we calculated the 2PA coefficient, β according to

$$\beta = \frac{n_0 2\Delta t}{I_{N0}^2 \hbar\omega} \quad (3)$$

Here, Δt is the full width at half-maximum (FWHM) laser pulse. To acquire the accurate laser pulse width, a sub nanosecond photodetector was used to record the pulse duration. (See **Figure S5.5**) To obtain the actual intensity entering the sample, the light intensity measured by the power meter was corrected for reflection at the air/film interface (see **Figure S5.6**). Basically, the values of β (cm/W) can be derived from the slope of $\frac{\Delta G_{max}}{e\beta_0 I_{N0}}$ versus I_{N0} in Figure 5.1a.

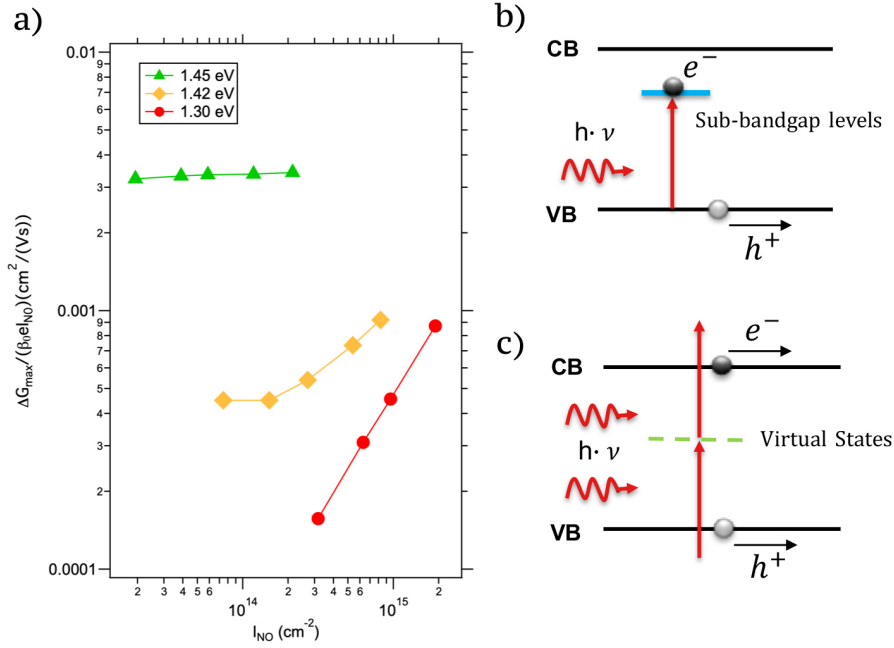


Figure 5.1. (a) Intensity normalized maximum photoconductance as a function of incident intensity for a $\text{CH}_3\text{NH}_3\text{PbI}_3$ film measured at incident photo energies of 1.45 eV, 1.42 eV and 1.30 eV. Schematics showing generation process of charge carriers by (b) optical excitation from or to sub-bandgap levels and (c) by two-photon absorption. Note that in the case of sub-bandgap linear absorption, this model also holds for the situation that mobile electrons are excited to the CB from filled sub-bandgap levels.

Figure 5.2a displays β as a function of photon energy, showing a rise by about two orders of magnitude on increasing photon energy. Considering that the reported β measured at 1064 nm for $\text{CH}_3\text{NH}_3\text{PbX}_3$ ($X = \text{Cl}, \text{Br}, \text{I}$) varies from 2.5×10^{-4} ($\hbar\omega/E_g = 0.524$) to 272 cm/MW ($\hbar\omega/E_g \sim 0.76$)^{20,17} excluding the negative values¹⁹, we can state that our values ranging from 0.18 ($\hbar\omega/E_g = 0.506$) to 15.8 cm/MW ($\hbar\omega/E_g = 0.886$) are plausible. The most commonly used theory for explaining the wavelength dependence of β is the scaling law²¹, which is given by:

$$\beta = a \frac{\left(\frac{2\hbar\omega}{E_g} - 1\right)^3}{\left(\frac{2\hbar\omega}{E_g}\right)^5} \quad (4)$$

Where a (cm/MW) is a product of several constants. To further clarify the frequency dependence of β , we first compare the wavelength-dependent function $f(\hbar\omega/E_g)$ given by the

scaling law (Eq 4) with our data. The bandgap energy, E_g of 1.58 eV obtained from the 1PA absorption spectrum was used for the fitting. As shown by the blue curve in **Figure 5.2a**, the large deviation mostly stems from the high energy regime. In our data, the wavelength-dependence of β shows a sharp rise at excitation energies close to $0.5 E_g$ followed by a second upward trend. Interestingly, this is opposite to the trend predicted by the scaling law. According to the scaling law, the maximum value of β is found at $0.7E_g$, which means the value of β should decrease for excitation energies approaching E_g .

Obviously, the scaling law is not directly applicable to perovskite materials, which might be explained by the following reasons. First, the scaling law was derived to calculate β in direct zinc blende semiconductors^{25,26}. It might be expected that the fundamental difference in the crystal structure may give rise to the different wavelength dependence. Second, the scaling law is based on a parabolic three-band model located at the Γ -point ($k = (0, 0, 0)$), which is comprised of a 2-fold VB and a single CB²¹. However, the electronic band structure close to the bandgap has been found to be rather different for $\text{CH}_3\text{NH}_3\text{PbI}_3$, where the CB is degenerated instead of the VB.²⁷ The spin-orbit coupling effects leads to spin-orbit split-off bands at the bottom of the CB.²⁸ Moreover, the lowest energetic transition occurs at the R-point ($k = (1/2, 1/2, 1/2)$) for both the cubic and the tetragonal phase for $\text{CH}_3\text{NH}_3\text{PbI}_3$. Furthermore, although the parabolic approximation usually holds for k values close to the high symmetry points, it has been reported that non-parabolicity of the CB and VB should be considered for photon energies away from the band edge.²⁹ Thus, non-parabolicity of the band structures may also account for the discrepancy in wavelength-dependence of β for $\hbar\omega/E_g \rightarrow 1$. Unfortunately, apart from a discussion on the matrix elements,²⁶ the origin of the downward trend as $\hbar\omega/E_g \rightarrow 1$ has been rarely addressed in Literature.

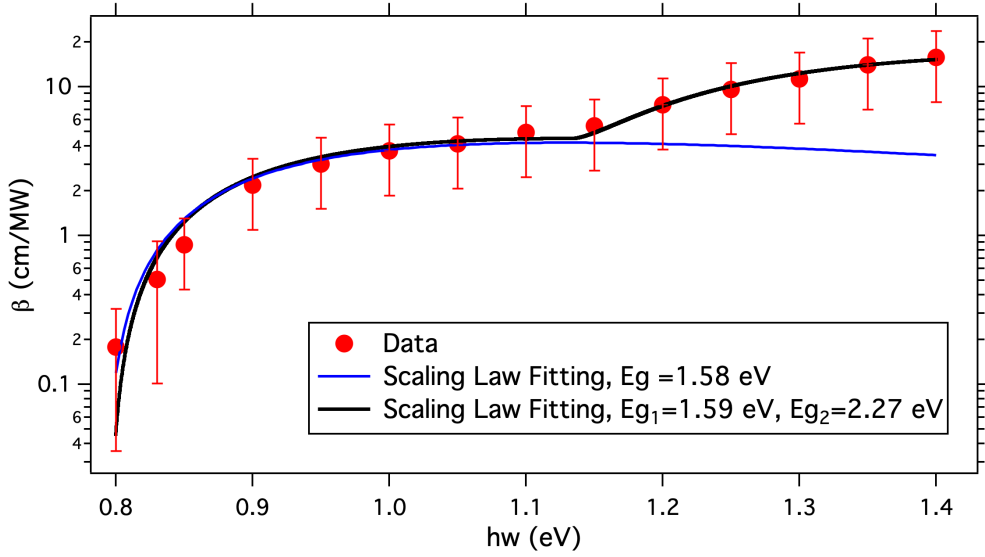


Figure 5.2. (a) Experimental 2PA spectrum for $\text{CH}_3\text{NH}_3\text{PbI}_3$ compared to the theoretical trend, where 50 % error bars arise from the uncertainty in laser pulses and the overestimated reflection. 80 % error bars were introduced at 0.8 eV and 0.83 eV due to the limited data available.

Then, we apply a summation of two-bandgap scaling laws for the 2PA coefficient β :

$$\beta = a_1 \frac{\left(\frac{2\hbar\omega}{E_{g1}} - 1\right)^3}{\left(\frac{2\hbar\omega}{E_{g1}}\right)^5} + a_2 \frac{\left(\frac{2\hbar\omega}{E_{g2}} - 1\right)^3}{\left(\frac{2\hbar\omega}{E_{g2}}\right)^5} \quad (5)$$

A bandgap E_{g1} of 1.59 eV and a second bandgap of E_{g2} of 2.27 eV have been found to agree well with our experimental data, as depicted in **Figure 5.2a** (black curve). The values of two coefficients in **Eq 5** have been determined as $a_1 = 95(\text{cm/MW})$ and $a_2 = 290(\text{cm/MW})$. The first bandgap E_{g1} of 1.59 eV is in good agreement with the one deduced from the 1PA spectrum. The second bandgap can be associated with the transitions at another symmetry point or between the higher levels of CB and VB, respectively. These unusual larger values of β observed at wider bandgaps may be the result of the larger matrix element and/or higher density of states. Interestingly, a computational study of band structure in cubic $\text{CH}_3\text{NH}_3\text{PbI}_3$ has shown that the bandgap at the M-point possesses an optical matrix element 3 times larger than that at the R-point³⁰(**Figure 5.2b**), which is in good accordance with the ratio of a_2 to a_1 . Since optical transitions are determined by both matrix element and density of states, a detailed

calculation on the band structure is required to verify whether the secondary transition is indeed at M-point or an overall result from both M-point and R-point.

It has been seen from the temperature-dependent X-ray powder diffraction that the crystal structure of $\text{CH}_3\text{NH}_3\text{PbI}_3$ gradually transforms from the cubic phase into the tetragonal phase³¹. Hence, it is reasonable to infer that the band structure of tetragonal $\text{CH}_3\text{NH}_3\text{PbI}_3$ at room temperature is comparable to that of cubic $\text{CH}_3\text{NH}_3\text{PbI}_3$. The secondary bandgap at the M-point in the cubic phase has been calculated to be ~ 2.7 or 2.5 eV with or without the spin orbit coupling³⁰, and a second peak near 2.6 eV has been observed in the 1PA spectrum of $\text{CH}_3\text{NH}_3\text{PbI}_3$ ³². A small difference of ~ 0.3 eV from TRMC results can be explained by that different energy levels may be involved in the 2PA transition than that in the 1PA process. This small difference also implies that the higher energy level at R-point may also be involved.

Furthermore, we investigated the effect of the phase transition on β using the temperature-dependent TRMC technique. Upon cooling down from the room temperature ($\sim 295\text{K}$), the absorption below the bandgap was recorded at different temperatures varying from 220K to 100K . The value of E_g at each temperature was determined by the cut-off wavelength from the temperature-dependent linear absorption spectra (see **Figure S5.7**). The absolute values of β at 1.2 eV calculated from the temperature-dependent TRMC measurements are slightly lower than those shown above, which can be explained by a different laser pulse shape used in the temperature-dependent TRMC. However, this does not affect the calculated trend for β .

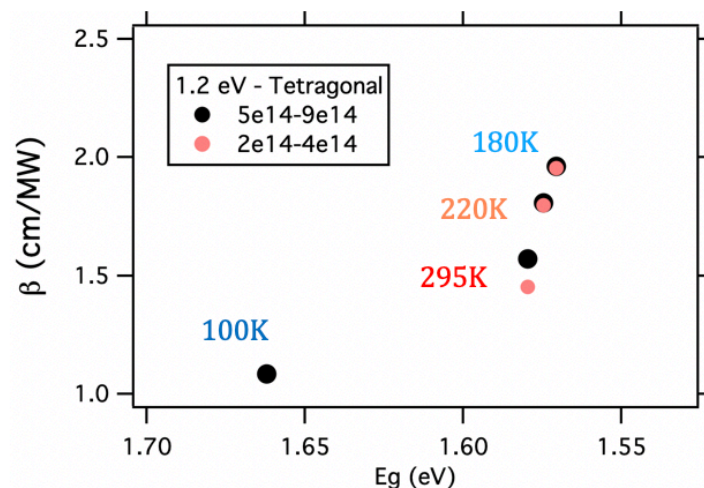


Figure 5.3. 2PA coefficient β versus the bandgap energy E_g at incident photon energy of 1.2 eV determined at different incident light intensities expressed in photons/cm².

Chapter 5

Since the bandgap energy of the $\text{CH}_3\text{NH}_3\text{PbI}_3$ thin film is known to change with temperature^{29,33}, β characterized at a specific excitation wavelength is expected to vary accordingly. As depicted in **Figure 5.3**, in the tetragonal phase, β measured at 1.2 eV slightly increases as the bandgap energy becomes smaller with decreasing temperature, which is consistent with **Eq 4** and the reported smaller 2PA transition rates observed at wider bandgap energies in $\text{CH}_3\text{NH}_3\text{PbI}_3$ powder³⁴ as well as CsPbBr_3 quantum dots.³⁵

For orthorhombic $\text{CH}_3\text{NH}_3\text{PbI}_3$ the values of β are smaller than those calculated for the tetragonal phase, which can be associated with the wider bandgap in the orthorhombic phase. It has been reported that both the M-point and R-point electronic states are folded to the Γ -point in the orthorhombic phase due to a reduction of the Brillouin zone volume³². Hence, we expect that the 2PA in the orthorhombic phase should correspond to the transitions at the Γ -point. It is important to note that the matrix element, the density of states as well as the allowed transitions regarding the 2PA could be different in the orthorhombic phase. Therefore, the smaller values of β could also be a result of the changes in several elements introduced by the phase transition.

CONCLUSION

In conclusion, with TRMC we record the 2PA spectrum of the $\text{CH}_3\text{NH}_3\text{PbI}_3$ polycrystalline film, which demonstrates a two-step upward trend. The data fit to the 2PA spectrum suggests a primary bandgap of 1.59 eV in correspondence with the 1PA bandgap and a second bandgap of 2.27 eV possibly stemming from the M-point (maybe R-point is also involved) in the first Brillouin zone. The sub-bandgap linear absorption is found to be the dominant process for the photon energy close to the bandgap edge ($\hbar\omega > 0.9E_g$) due to high density of trap states. Temperature-dependent TRMC shows negative correlation between the values of β at a specific wavelength and the bandgap associated with temperature and structural phase. A computational study on the 2PA coefficient of $\text{CH}_3\text{NH}_3\text{PbI}_3$ using its band structure in different phases may help to further clarify the role of phase transition with respect to the 2PA spectrum.

REFERENCES

- (1) Green, M. A.; Ho-Baillie, A.; Snaith, H. J. The Emergence of Perovskite Solar Cells. *Nat. Photonics* **2014**, *8*, 506–514.
- (2) Hodes, G. Perovskite-Based Solar Cells. *Science*. 2013.
- (3) Ponseca, C. S.; Savenije, T. J.; Abdellah, M.; Zheng, K.; Yartsev, A.; Pascher, T.; Harlang, T.; Chabera, P.; Pullerits, T.; Stepanov, A.; et al. Organometal Halide Perovskite Solar Cell Materials Rationalized: Ultrafast Charge Generation, High and Microsecond-Long Balanced Mobilities, and Slow Recombination. *J. Am. Chem. Soc.* **2014**, *136*, 5189–5192.
- (4) Oga, H.; Saeki, A.; Ogomi, Y.; Hayase, S.; Seki, S. Improved Understanding of the Electronic and Energetic Landscapes of Perovskite Solar Cells: High Local Charge Carrier Mobility, Reduced Recombination, and Extremely Shallow Traps. *J. Am. Chem. Soc.* **2014**.
- (5) Bi, Y.; Hutter, E. M.; Fang, Y.; Dong, Q.; Huang, J.; Savenije, T. J. Charge Carrier Lifetimes Exceeding 15 Ms in Methylammonium Lead Iodide Single Crystals. *J. Phys. Chem. Lett.* **2016**, *7*, 923–928.
- (6) Brenes, R.; Guo, D.; Osherov, A.; Noel, N. K.; Eames, C.; Hutter, E. M.; Pathak, S. K.; Niroui, F.; Friend, R. H.; Islam, M. S.; et al. Metal Halide Perovskite Polycrystalline Films Exhibiting Properties of Single Crystals. *Joule* **2017**, *1*, 155–167.
- (7) Ferrando, A.; Martínez Pastor, J. P.; Suárez, I. Toward Metal Halide Perovskite Nonlinear Photonics. *J. Phys. Chem. Lett.* **2018**, *9*, 5612–5623.

Chapter 5

- (8) Gu, Z.; Wang, K.; Sun, W.; Li, J.; Liu, S.; Song, Q.; Xiao, S. Two-Photon Pumped CH₃NH₃PbBr₃ Perovskite Microwire Lasers. *Adv. Opt. Mater.* **2016**, *4*, 472–479.
- (9) Xu, Y.; Chen, Q.; Zhang, C.; Wang, R.; Wu, H.; Zhang, X.; Xing, G.; Yu, W. W.; Wang, X.; Zhang, Y.; et al. Two-Photon-Pumped Perovskite Semiconductor Nanocrystal Lasers. *J. Am. Chem. Soc.* **2016**, *138*, 3761–3768.
- (10) Li, P.; Chen, Y.; Yang, T.; Wang, Z.; Lin, H.; Xu, Y.; Li, L.; Mu, H.; Shivananju, B. N.; Zhang, Y.; et al. Two-Dimensional CH₃NH₃PbI₃ Perovskite Nanosheets for Ultrafast Pulsed Fiber Lasers. *ACS Appl. Mater. Interfaces* **2017**, *9*, 12759–12765.
- (11) Dong, N.-N.; Pedroni, M.; Piccinelli, F.; Conti, G.; Sbarbati, A.; Ramirez-Hernández, J. E.; Maestro, L. M.; la Cruz, M. C.; Sanz-Rodríguez, F.; Juarranz, A.; et al. NIR-to-NIR Two-Photon Excited CaF₂: Tm³⁺, Yb³⁺ Nanoparticles: Multifunctional Nanoprobes for Highly Penetrating Fluorescence Bio-Imaging. *ACS Nano* **2011**, *5*, 8665–8671.
- (12) Bharali, D. J.; Lucey, D. W.; Jayakumar, H.; Pudavar, H. E.; Prasad, P. N. Folate-Receptor-Mediated Delivery of InP Quantum Dots for Bioimaging Using Confocal and Two-Photon Microscopy. *J. Am. Chem. Soc.* **2005**.
- (13) Shen, Y.; Shuhendler, A. J.; Ye, D.; Xu, J.-J.; Chen, H.-Y. Two-Photon Excitation Nanoparticles for Photodynamic Therapy. *Chem. Soc. Rev.* **2016**, *45*, 6725–6741.
- (14) Cumpston, B. H.; Ananthavel, S. P.; Barlow, S.; Dyer, D. L.; Ehrlich, J. E.; Erskine, L. L.; Heikal, A. A.; Kuebler, S. M.; Lee, I.-Y. S.; McCord-Maughon, D.; et al. Two-Photon Polymerization Initiators for Three-Dimensional Optical Data Storage and Microfabrication. *Nature* **1999**, *398*, 51.
- (15) Xing, G.; Liao, Y.; Wu, X.; Chakraborty, S.; Liu, X.; Yeow, E. K. L.; Chan, Y.; Sum, T. C. Ultralow-Threshold Two-Photon Pumped Amplified Spontaneous Emission and

- Lasing from Seeded CdSe/CdS Nanorod Heterostructures. *ACS Nano* **2012**, *6*, 10835–10844.
- (16) Walters, G.; Sutherland, B. R.; Hoogland, S.; Shi, D.; Comin, R.; Sellan, D. P.; Bakr, O. M.; Sargent, E. H. Two-Photon Absorption in Organometallic Bromide Perovskites. *ACS Nano* **2015**, *9*, 9340–9346.
- (17) Kalanoor, B. S.; Gouda, L.; Gottesman, R.; Tirosh, S.; Haltzi, E.; Zaban, A.; Tischler, Y. R. Third-Order Optical Nonlinearities in Organometallic Methylammonium Lead Iodide Perovskite Thin Films. *Acs Photonics* **2016**, *3*, 361–370.
- (18) Saouma, F. O.; Park, D. Y.; Kim, S. H.; Jeong, M. S.; Jang, J. I. Multiphoton Absorption Coefficients of Organic–Inorganic Lead Halide Perovskites CH₃NH₃PbX₃ (X= Cl, Br, I) Single Crystals. *Chem. Mater.* **2017**, *29*, 6876–6882.
- (19) Zhang, R.; Fan, J.; Zhang, X.; Yu, H.; Zhang, H.; Mai, Y.; Xu, T.; Wang, J.; Snaith, H. J. Nonlinear Optical Response of Organic–Inorganic Halide Perovskites. *ACS Photonics* **2016**, *3*, 371–377.
- (20) Yamada, T.; Aharen, T.; Kanemitsu, Y. Near-Band-Edge Optical Responses of CH₃NH₃PbCl₃ Single Crystals: Photon Recycling of Excitonic Luminescence. *Phys. Rev. Lett.* **2018**, *120*, 57404.
- (21) Van Stryland, E. W.; Vanherzeele, H.; Woodall, M. A.; Soileau, M. J.; Smirl, A. L.; Guha, S.; Boggess, T. F. Two Photon Absorption, Nonlinear Refraction, and Optical Limiting in Semiconductors. *Opt. Eng.* **1985**, *24*, 244613.
- (22) Savenije, T. J.; Ferguson, A. J.; Kopidakis, N.; Rumbles, G. Revealing the Dynamics of Charge Carriers in Polymer:Fullerene Blends Using Photoinduced Time-Resolved Microwave Conductivity. *J. Phys. Chem. C* **2013**, *117*, 24085–24103.
- (23) Hutter, E. M.; Eperon, G. E.; Stranks, S. D.; Savenije, T. J. Charge Carriers in Planar and Meso-Structured Organic-Inorganic Perovskites: Mobilities, Lifetimes, and

Chapter 5

- Concentrations of Trap States. *J. Phys. Chem. Lett.* **2015**, *6*, 3082–3090.
- (24) Dicker, G.; De Haas, M. P.; Siebbeles, L. D. A.; Warman, J. M. Electrodeless Time-Resolved Microwave Conductivity Study of Charge-Carrier Photogeneration in Regioregular Poly(3-Hexylthiophene) Thin Films. *Phys. Rev. B - Condens. Matter Mater. Phys.* **2004**.
- (25) Pidgeon, C. R.; Wherrett, B. S.; Johnston, A. M.; Dempsey, J.; Miller, A. Two-Photon Absorption in Zinc-Blende Semiconductors. *Phys. Rev. Lett.* **1979**, *42*, 1785.
- (26) Weiler, M. H. Nonparabolicity and Exciton Effects in Two-Photon Absorption in Zincblende Semiconductors. *Solid State Commun.* **1981**, *39*, 937–940.
- (27) Umabayashi, T.; Asai, K.; Kondo, T.; Nakao, A. Electronic Structures of Lead Iodide Based Low-Dimensional Crystals. *Phys. Rev. B* **2003**, *67*, 155405.
- (28) Even, J.; Pedesseau, L.; Jancu, J. M.; Katan, C. Importance of Spin-Orbit Coupling in Hybrid Organic/Inorganic Perovskites for Photovoltaic Applications. *J. Phys. Chem. Lett.* **2013**, *4*, 2999–3005.
- (29) Davies, C. L.; Filip, M. R.; Patel, J. B.; Crothers, T. W.; Verdi, C.; Wright, A. D.; Milot, R. L.; Giustino, F.; Johnston, M. B.; Herz, L. M. Bimolecular Recombination in Methylammonium Lead Triiodide Perovskite Is an Inverse Absorption Process. *Nat. Commun.* **2018**, *9*, 1–9.
- (30) Even, J.; Pedesseau, L.; Katan, C. Analysis of Multivalley and Multibandgap Absorption and Enhancement of Free Carriers Related to Exciton Screening in Hybrid Perovskites. **2014**.
- (31) Whitfield, P. S.; Herron, N.; Guise, W. E.; Page, K.; Cheng, Y. Q.; Milas, I.; Crawford, M. K. Structures, Phase Transitions and Tricritical Behavior of the Hybrid Perovskite Methyl Ammonium Lead Iodide. *Sci. Rep.* **2016**, *6*, 35685.

- (32) Appavoo, K.; Nie, W.; Blancon, J.-C.; Even, J.; Mohite, A. D.; Sfeir, M. Y. Ultrafast Optical Snapshots of Hybrid Perovskites Reveal the Origin of Multiband Electronic Transitions. *Phys. Rev. B* **2017**, *96*, 195308.
- (33) Milot, R. L.; Eperon, G. E.; Snaith, H. J.; Johnston, M. B.; Herz, L. M. Temperature-Dependent Charge-Carrier Dynamics in CH₃NH₃PbI₃ Perovskite Thin Films. *Adv. Funct. Mater.* **2015**, *25*, 6218–6227.
- (34) Saouma, F. O.; Stoumpos, C. C.; Wong, J.; Kanatzidis, M. G.; Jang, J. I. Selective Enhancement of Optical Nonlinearity in Two-Dimensional Organic-Inorganic Lead Iodide Perovskites. *Nat. Commun.* **2017**, *8*, 1–7.
- (35) Chen, J.; Zidek, K.; Chábera, P.; Liu, D.; Cheng, P.; Nuuttila, L.; Al-Marri, M. J.; Lehtivuori, H.; Messing, M. E.; Han, K.; et al. Size-and Wavelength-Dependent Two-Photon Absorption Cross-Section of CsPbBr₃ Perovskite Quantum Dots. *J. Phys. Chem. Lett.* **2017**, *8*, 2316–2321.

Appendices

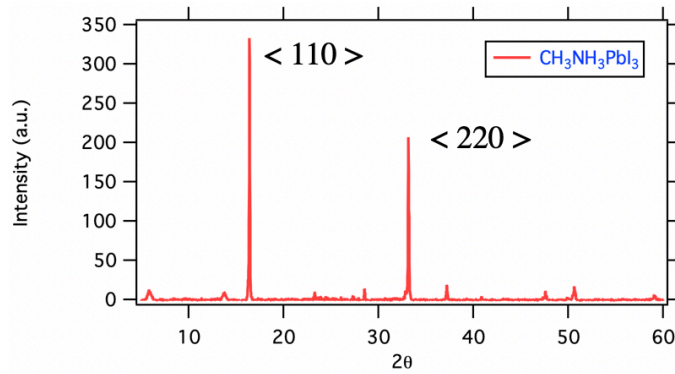


Figure S5.1: XRD pattern for $\text{CH}_3\text{NH}_3\text{PbI}_3$ thin film (Co $\kappa\alpha$ radiation, $\lambda = 1.78 \text{ \AA}$)

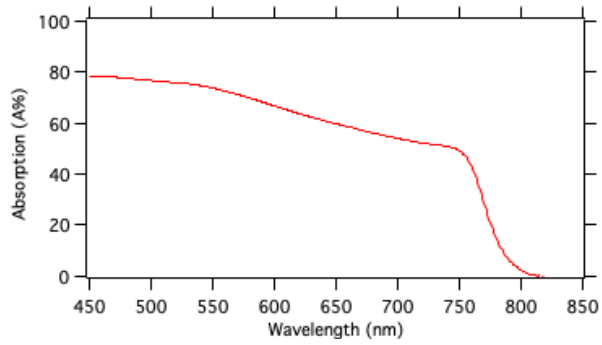


Figure S5.2: The absorption spectrum of $\text{CH}_3\text{NH}_3\text{PbI}_3$ thin film

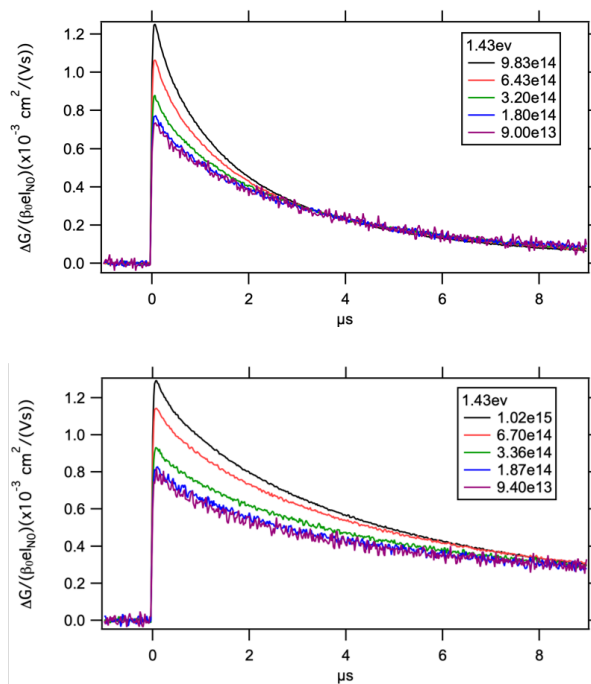


Figure S5.3: TRMC traces for a $\text{CH}_3\text{NH}_3\text{PbI}_3$ thin film measured before (left) and after (right) the light soaking treatment at excitation photo energy of 1.43 eV (867nm). The legend in each graph shows incident light intensity in photons/cm².

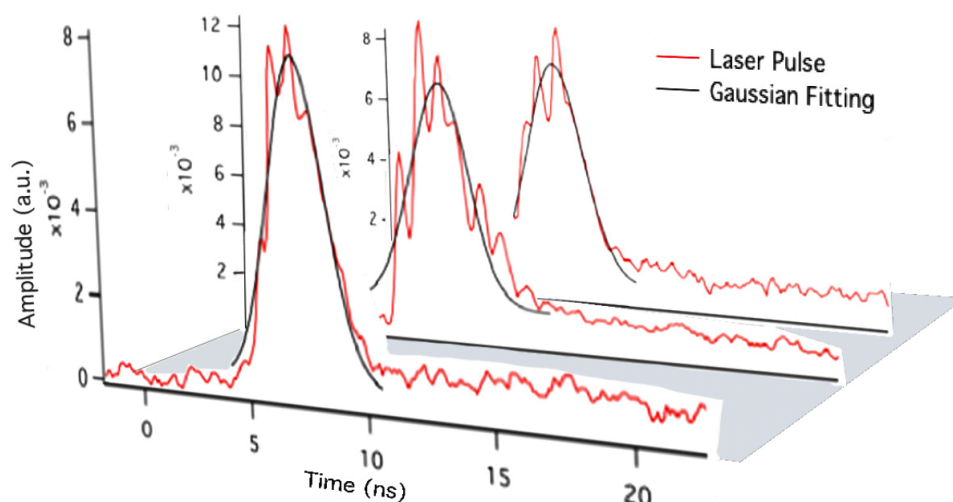


Figure S5.4: Laser pulse traces recorded at 900 nm and corresponding Gaussian fitting.

A silicon photodetector was used to record the pulse signals as a function of time. For each wavelength, ten shots were measured and fitted by a Gaussian function. The measurements can hold for different intensities, because the filters used to vary the laser intensity will not change the pulse shape. **Figure S5.4** shows three examples of laser pulse traces measured at 900 nm and the corresponding Gaussian fitting. Results show that the average pulse duration is around 3.0 ± 0.2 ns for the wavelengths of interest. Although only wavelengths less than 1100 nm can be well characterized due to the limitation of the photodetector, it is reasonable to assume that a laser pulse of a longer wavelength has the similar pulse profile as its co-generated counterpart in the visible regime.

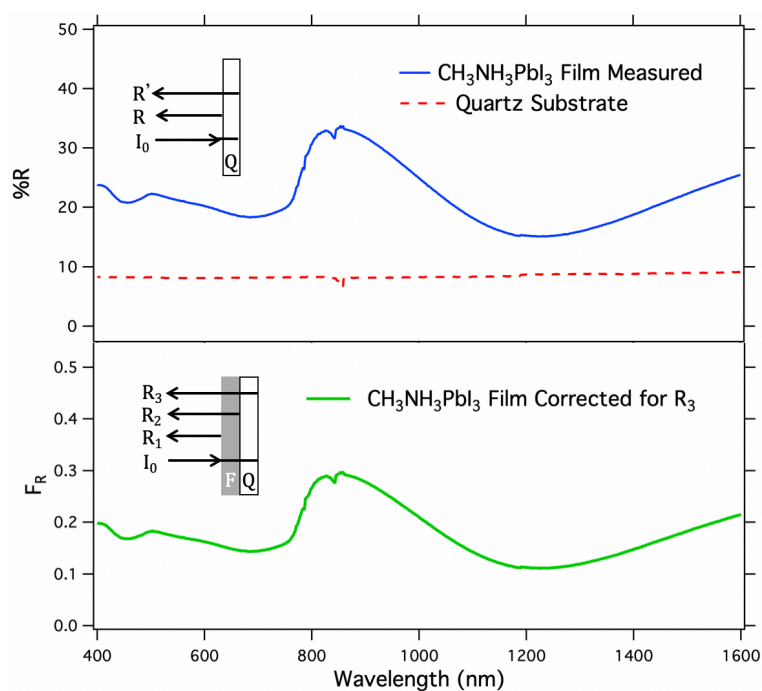


Figure S5.5: The reflectance for a $\text{CH}_3\text{NH}_3\text{PbI}_3$ thin film deposited on the substrate (blue curve) and a quartz substrate (dashed line) and the fraction of reflected light for the thin film (green curve).

The reflectance of the sample and the quartz substrate in the NIR regime was measured by the UV/Vis/NIR spectrometer (See in **Figure S5.5**). As light travels through a quartz substrate in the air, reflections will occur at the two interfaces of the refractive index change. For the case of normal incidence (See in the upper inset), both surfaces of the non-absorbing quartz substrate should contribute equally to the reflectance according to the Fresnel's equation:

$$R = \frac{(n_1 - n_2)^2}{(n_1 + n_2)^2} \quad (1)$$

Where the reflection is determined by the refractive index of the first and the second medium (n_1, n_2). For a thin film deposited on a quartz substrate (See in the lower inset), the total reflection is approximately to be comprised of three parts, the reflection at the interface between air and thin film, R_1 , thin film and the substrate, R_2 , and the substrate and air, R_3 . The refractive index of air and quartz are known to be around 1.0¹ and 1.5², respectively. Typically, a $\text{CH}_3\text{NH}_3\text{PbI}_3$ thin film has a refractive index of $\sim 2.5^3$ in the NIR regime. Hence, the reflection mainly stems from the interface between air and film, while R_2 and R_3 have comparable smaller contributions to the total reflection. **Figure S5.5** shows that the total

reflectance from both surfaces of the substrate is almost a constant of 8%, while the reflectance of the sample varies with the excitation wavelengths. Since most of light is not absorbed by the film in this regime, R_3 is estimated to be 4%. R_1 and R_2 are associated with the wavelength-dependent refractive index of the $\text{CH}_3\text{NH}_3\text{PbI}_3$ film, which is difficult to be measured separately. Therefore, the fraction of reflected light, F_R in the sample was only corrected for the rear surface of the quartz substrate. In conjunction with the laser power measured by the power meter, the incident light intensity I_{N0} entering the sample can be obtained.

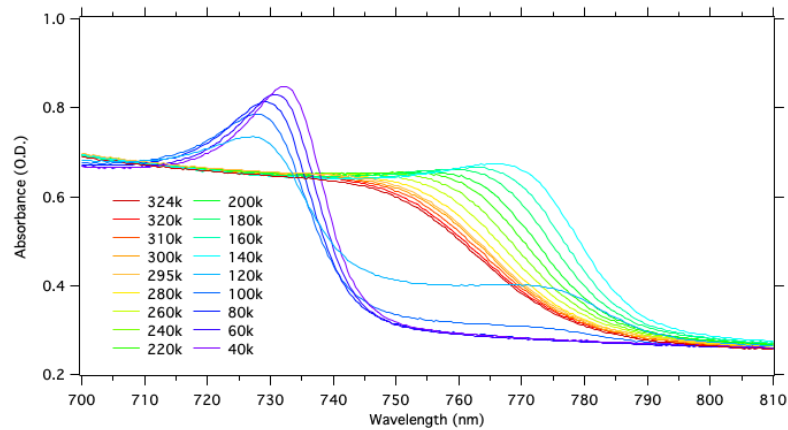


Figure S5.6: Temperature-dependent absorbance for $\text{CH}_3\text{NH}_3\text{PbI}_3$ thin film

REFERENCES

- (1) Ciddor, P. E. Refractive Index of Air: New Equations for the Visible and near Infrared. *Appl. Opt.* **2008**. <https://doi.org/10.1364/ao.35.001566>.
- (2) Rodríguez-de Marcos, L. V.; Larruquert, J. I.; Méndez, J. A.; Aznárez, J. A. Self-Consistent Optical Constants of SiO₂ and Ta₂O₅ Films. *Opt. Mater. Express* **2016**. <https://doi.org/10.1364/OME.6.003622>.
- (3) Phillips, L. J.; Rashed, A. M.; Treharne, R. E.; Kay, J.; Yates, P.; Mitrovic, I. Z.; Weerakkody, A.; Hall, S.; Durose, K. Dispersion Relation Data for Methylammonium Lead Triiodide Perovskite Deposited on a (100) Silicon Wafer Using a Two-Step Vapour-Phase Reaction Process. *Data Br.* **2015**. <https://doi.org/10.1016/j.dib.2015.10.026>.

Summary

Metal halide perovskites (MHPs) are interesting candidates for application in photovoltaic devices. During the past decade the efficiency of perovskite solar cells has improved enormously exceeding now values over 24%. In an MHP absorber layer, charge carriers are generated on optical excitation, and decay by band-to-band recombination or by other undesired loss mechanisms. In this thesis, the relationship between material properties, including constituents and morphology of the MHP layer and these processes is studied. The charge carrier dynamics describing these light-induced processes are studied by the time-resolved microwave photoconductivity (TRMC) technique, in combination with standard optical techniques such as time-resolved photoluminescence (TRPL).

Chapter 2 shows that reducing the non-radiative recombination is a necessary step to approach the maximal achievable efficiency, the so-called Shockley-Queisser limit. In this chapter, various MHPs with different compositions and post-production treatments are studied by TRMC. From the same kind of layers also devices are prepared and photovoltaic properties are determined. From the rate constants describing the charge carrier dynamics of the TRMC traces, the Fermi-level splitting, μ_F under 1 sun illumination is calculated. The Fermi-level splitting sets the limit for their achievable open circuit voltage V_{oc} . Interestingly, we find that for vacuum-evaporated MAPbI₃ and K⁺-doped (MA,FA,Cs)Pb(I/Br)₃, the μ_F/e values are close to the reported V_{oc} values. This implies that for an improvement of the V_{oc} , charge carrier recombination within the bare MHPs has to be reduced. On the other hand, for MHPs with Cs⁺ and/or Rb⁺ addition, the experimental V_{oc} is still below μ_F/e , suggesting that higher voltages are feasible by optimizing the transport layers. The presented approach will help to select which techniques and transport layers are beneficial to improve the efficiency of MHP solar cells.

So far, the highest reported efficiencies of MHP solar cells are all based on mixed cation, mixed halide perovskites, such as (FA,MA,Cs)Pb(I_{1-x}Br_x)₃ with $x = 0 - 1$. Although it has been recently demonstrated that light soaking induces halide segregation in these mixed perovskites, it is unclear how the charge carrier dynamics are affected across the entire material family. In **Chapter 3**, various (FA,MA,Cs)Pb(I_{1-x}Br_x)₃ perovskite films are light-soaked in nitrogen and the change in properties is investigated through TRMC, optical and structural techniques. To explain the TRMC decay kinetics for pristine (FA,MA,Cs)Pb(I_{1-x}Br_x)₃, apart from band-to-band recombination, and trap mediated decay, additional shallow

states have to be included, which are not required to describe the dynamics of mixed cations samples with $x = 0$ or $x = 1$ nor for single cation MHPs. These shallow states can, independently of x , be removed by light soaking, although after a prolonged period in the dark these shallow states reappear. We interpret the shallow states as being due to initially well-intermixed halide distributions but after light soaking the halides segregate leading to domains with smaller bandgaps. For these mixed MHPs, the removal of shallow states leads to a reduction in the imbalance between diffusional motion of electrons and holes.

By changing the bromide/halide ratio of MHPs the bandgap can be manipulated which makes this material interesting for application in tandem solar cells. In view of its bandgap of 2.2 eV MAPbBr₃ is a possible candidate as absorber layer in a top cell of a tandem solar cell. In **Chapter 4**, using complementary temperature-dependent TRMC and TRPL measurements, we demonstrate that the exciton yield increases with lower temperatures at the expense of the charge carrier generation yield. By comparison of the TRMC and TRPL traces we conclude that in the orthorhombic phase the second broad emission peak at 622 nm and in the cubic phase the emission at around 580 nm originate from radiative recombination of charges trapped in surface defects. We present a kinetic model describing both the decay in photo-conductance as well as the slow ingrowth of the TRPL. Knowledge of defect states at the surface of various crystal phases is of interest to reach higher open circuit voltages in MAPbBr₃ based solar cells.

Although there has been intense research into the optoelectronic properties, the sub-bandgap absorption in MHPs remains largely unexplored. In **Chapter 5**, two photon absorption (2PA) spectra of polycrystalline MHP thin films are recorded using the TRMC over a broad wavelength regime varying from $0.49E_g < \hbar\omega < E_g$. The 2PA coefficients, β were obtained by taking into account the quadratic relationship between the number of induced charge carriers and the incident light intensity. A two-step upward trend is observed in the 2PA spectrum for MAPbI₃, and its bromide analogue (MAPbBr₃), which indicates that the commonly used scaling law is not directly applicable to MHPs. We interpret the two-step behavior as being due to multi-bandgap transitions. The present work shows that valuable insight can be obtained in the opto-electronic properties of MHPs by sub bandgap spectroscopy.

Samenvatting

Metaalhalide perovskieten (MHPs) zijn interessante materialen voor toepassing in zonnecellen. Gedurende het afgelopen decennium is de efficiëntie van perovskiet-zonnecellen enorm verbeterd en bedraagt nu meer dan 24%. In een MHP absorberende laag worden ladingsdragers gegenereerd door optische excitatie. Vervolgens kunnen deze ladingsdragers vervallen door band-naar-band recombinatie of door alternatieve ongewenste verlies mechanismen zoals via een defect toestand. In dit proefschrift wordt de relatie tussen materiaaleigenschappen, inclusief bestanddelen en morfologie van de MHP laag en deze processen bestudeerd. De dynamica van de licht geïnduceerde ladingsdragers wordt bestudeerd met behulp van tijd-opgeloste microgolf fotogeleiding (TRMC), in combinatie met standaard optische technieken zoals tijd-opgeloste fotoluminescentie (TRPL).

Hoofdstuk 2 laat zien dat het verminderen van niet-stralende recombinatie een noodzakelijke stap is om de maximaal haalbare efficiëntie te benaderen, de zogenaamde Shockley-Queisser-limiet. In dit hoofdstuk worden dunne lagen van verschillende MHPs bestudeerd met de TRMC techniek. Van dezelfde type lagen worden ook zonnecellen gemaakt en worden de fotonvoltaïsche eigenschappen bepaald. Uit de snelheidsconstanten die de dynamica van de ladingsdragers beschrijven, kunnen de pseudo Fermi-niveaus voor elektronen en gaten worden berekend onder belichting. De energetische splitsing van deze pseudo Fermi-niveaus, μ_F bepaalt de limiet voor de haalbare open klem spanning, V_{oc} . We vinden dat voor vacuüm opgedampte MAPbI₃ en K⁺ gedoteerde (MA,FA,Cs)Pb(I/Br)₃ de μ_F/e waarden dicht bij de gerapporteerde V_{oc} waarden liggen. Dit impliceert dat voor een verbetering van de V_{oc} de recombinatie van ladingdragers in de kale MHP lagen moet worden verminderd. Aan de andere kant voor MHPs gemengd met kleine hoeveelheden Cs⁺ en/of Rb⁺, is de experimentele V_{oc} lager dan μ_F/e , wat suggereert dat hogere spanningen haalbaar zijn door de transportlagen te optimaliseren. De gepresenteerde aanpak helpt bij het selecteren welke technieken en transportlagen gunstig zijn voor het verbeteren van de efficiëntie van MHP-zonnecellen.

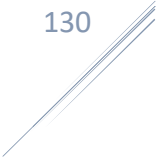
Tot dusverre zijn de hoogst gerapporteerde efficiënties van MHP zonnecellen allemaal gemaakt van perovskieten die gebaseerd zijn op een mengsel van meerdere kationen en haliden, zoals (FA,MA,Cs)Pb(I_{1-x}Br_x)₃ met x variërend tussen 0 en 1. Hoewel recentelijk is aangetoond dat belichten leidt tot segregatie van de halides in deze gemengde perovskieten,

is het onduidelijk hoe de dynamica van de ladingsdragers wordt beïnvloed. In hoofdstuk 3 worden verschillende MHP lagen in stikstof belicht en de veranderingen in eigenschappen onderzocht m.b.v. TRMC, optische en structurele technieken. Om de TRMC vervalkinetiek voor een niet behandelde (FA,MA,Cs)Pb(I_{1-x}Br_x)₃ laag, te verklaren, moeten er afgezien van band-naar-band recombinatie en verval via diepe defecten extra, ondiepe toestanden in de band-gap worden aangenomen. Opmerkelijk genoeg zijn deze toestanden niet vereist om de dynamica van (FA,MA,Cs)Pb(I_{1-x}Br_x)₃ met $x = 0$ of $x = 1$ te beschrijven, noch voor MHPs gebaseerd op een enkel kation. Deze ondiepe toestanden kunnen, onafhankelijk van x worden verwijderd door te belichten met zichtbaar licht, hoewel na een lange periode in het donker deze ondiepe toestanden weer verschijnen. Wij schrijven deze ondiepe toestanden toe aan lokale inhomogene distributies van de halides, die na belichten resulteren in domeinen met een smallere bandgap. Het verwijderen van deze ondiepe toestanden leidt tot een vermindering van de onbalans tussen de diffuse beweging van elektronen en gaten.

Door de bromide / halide verhouding in MHPs te wijzigen, kan de bandgap worden gemanipuleerd waardoor dit materiaal interessant is voor toepassing in tandemzonnecellen. Met het oog op de bandgap van 2,2 eV is MAPbBr₃ een mogelijke kandidaat als absorberende laag in een bovenste subcel van een tandem-zonnecel. In Hoofdstuk 4 laten we zien dat, door complementaire temperatuurafhankelijke TRMC- en TRPL-metingen, de excitonopbrengst toeneemt met lagere temperaturen ten koste van de opbrengst van de ladingsdragers. Door vergelijking van de TRMC- en TRPL-verval kinetiek concluderen we dat in de orthorhombische fase de tweede brede emissiepiek bij 622 nm en in de kubische fase de emissie bij ongeveer 580 nm afkomstig zijn van stralende recombinatie van ladingen uit oppervlakte defecten. We presenteren een kinetisch model dat zowel het verval in fotogeleiding als de langzame ingroei van de TRPL beschrijft. Kennis van defecttoestanden aan het oppervlak van verschillende kristalfasen is van belang om hogere open klem spanningen in MAPbBr₃ gebaseerde cellen te bereiken.

Hoewel er intensief onderzoek is gedaan naar de opto-elektronische eigenschappen van MHPs, blijft de absorptie van fotonen met minder energie dan de band-gap grotendeels onbekend. In Hoofdstuk 5 worden twee foton-absorptie (2PA) spectra van polykristallijne dunne MHP lagen gemeten met behulp van de TRMC techniek over een breed golflengte gebied variërend van $0.49E_g < \hbar\omega < E_g$. De 2PA coëfficiënten, β werden verkregen door rekening te houden met de kwadratische relatie tussen het aantal geïnduceerde ladingdragers en de invallende lichtintensiteit. Een tweetraps opwaartse trend wordt waargenomen in het

2PA-spectrum voor MAPbI_3 en de bromide-analoog (MAPbBr_3), wat aangeeft dat de algemeen gebruikte methode voor het interpreteren van deze spectra niet direct van toepassing is op MHPs. We verklaren het spectrum dan ook als het gevolg van meerdere 2 foton overgangen. Het huidige werk laat zien dat waardevol inzicht kan worden verkregen in de band structuur van MHPs door deze zogenaamde sub band-gap spectroscopie toe te passen.



Acknowledgement

As a start, I would like to say I really enjoy the four years in Delft. This downtown is cosy and not crowded at all. Everyone in the university is friendly, from pedestrians in the streets to the lecturers in the classrooms. I do value such a nice environment, which is important for research. Even the rains here turn out to be cute, although I am personally not a fan of rains.

First, I would like to thank **Dr Ir Tom J. Savenije** who accepted my PhD application and supports me all the time. He is always very patient and never shows annoyed by frequent questions from students including me. His door is always open for students, and I believe our conversation per week is far more frequent than the average that students could get generally. I also appreciate his time in revising my English writing, which I suppose cost much more time than average too. He recommended me the summer schools, which all turned out to be super nice, and courses out of the long list from the graduate school, which were all helpful for my own case. I even got one-to-one help on presentation. I am also thankful that I could discuss with him what I really think for either research or personal career goals.

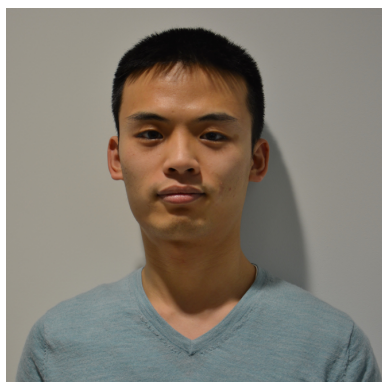
I also enjoy the awesome experience in the OM group. We had so many happy moments together, not only group meeting per week, but also the group activities such as the group excursions. I appreciate the comfortable conversations with **Prof dr Laurens D.A. Siebbeles**, **Dr Ferdinand Grozema** and **Dr AJ (Arjan) Houtepen**. I never felt hierarchy while talking with them. Either suggestions and comments are all from sincere opinions. This is perfect group for students coming for research. I would suggest younger students to try best to apply for the positions in this group.

The colleagues in our group are also super nice, even though we might have very different research directions, everyone is willing to help others for either sharing knowledge and how to operate the apparatus. Here, many thanks to **Gianluca**, **Sólrún**, and **Ryan**. I have had a very pleasant time with the perovskite team **Eline**, **Davide**, **Sudeep**, **Valentina** and **Maria**. We not only share the understanding of the research, the great time in conferences abroad but also spoil free time together in zoos or regularly in the Chinese restaurants in Rotterdam. I also thank our other colleagues, **Kevin**, **Cansel** and **Damla** for their hospitality to invite me to their parties. My students, **Zimu**, **Kevin**, and **Jasper** were all working with enthusiasm and independency. I'm proud to be their daily supervisor.

It is my luck and honour to collaborate with researchers all around the world, introduced by my supervisor Tom. Many thanks for the numerous talks and Skype meetings with **Dr Sam Stranks** and **Zahra** from Cambridge University. I am also thankful for the samples and feedbacks from **Prof Dr Jinsong Huang**, **Dr Yuze Lin**, and **Dr Haotong Wei** from the University of North Carolina, Chapel Hill. Same thanks to **Igal** and **Prof Dr David Cahen** from Weizmann Institute of Science.

Finally, I would like to thank my family. My **dad** is always supporting me without any reasons. My **mom** used to push me hard since I had memories. She established my basic understanding of maths and stimulated my strong willing for freedom and independence. Thanks to my best friends in China, we have been supporting and caring for each other in a group named Schrodinger's cats since high school. I am grateful to my first supervisor **Prof Dr Chongxin Shan** who gave me the chance to start research in the Chinese Academy of Sciences and introduced me into the research world. I appreciate the luck that I met my girlfriend, **Shan Yang**. I'm thankful for her trust and support even though we are 7984 km away from each other.

Curriculum Vitae



Dengyang Guo (郭澄阳) was born in WenShui, ShanXi, China on August 24, 1989. He graduated from Central South University, China with a bachelor degree in Material Science and Engineering, and then received a master degree in Condensed Matter Physics from the State Key Laboratory of Luminescence and Applications, Chinese Academy of Sciences.

In 2015 he started his PhD project under supervision of Dr Ir Tom J. Savenije at Delft University of Technology. His PhD work focuses on charge carrier dynamics in organometal metal perovskites of interest for photovoltaic applications. The main methods are complementary photo-induced microwave conductance (TRMC) and photoluminescence (PL). In addition, he supervised one master student and three bachelor students, and three LO2 projects for undergraduate students.

List of publications

Peer-refereed Journal Articles

1. **Guo, D.**; Caselli, V.; Hutter, E. M.; Savenije, T. J. Comparing the Calculated Fermi Level Splitting with the Open Circuit Voltage in Various Perovskite Cells. *ACS Energy Lett.* **2019**, *4*, 855–860.
(Cover of the issue;
Highlighted by the editors in “Energy Selects”;
One of the most read articles in ACS Energy Lett. for April 2019)
2. **Guo, D.**; Garmaroudi, Z. A.; Abdi-jalebi, M.; Stranks, S. D.; Savenije, T. J. Reversible Removal of Intermixed Shallow States by Light Soaking Multi- Cation Mixed Halide Perovskite Films. *ACS Energy Lett.* **2019**, *4*, 2360–2367.
3. **Guo, D.**; Bartesaghi, D.; Wei, H.; Hutter, E. M.; Huang, J.; Savenije, T. J. Photoluminescence from Radiative Surface States and Excitons in Methylammonium Lead Bromide Perovskites. *J. Phys. Chem. Lett.* **2017**, *8*, 4258–4263.
4. **Guo, D.**; Shan, C.; Liu, K.; Lou, Q.; Shen, D. Surface Plasmon Effect of Carbon Nanodots. *Nanoscale* **2015**, *7*, 18908–18913.
5. **Guo, D.**; Shan, C.; Qu, S.; Shen, D. Highly Sensitive Ultraviolet Photodetectors Fabricated from ZnO Quantum Dots/Carbon Nanodots Hybrid Films. *Sci. Rep.* **2014**, *4*, 7469.
6. Wei, Z; **Guo, D.**; Caselli, V.; Savenije, T. J. Multi Bandgap Transitions Revealed by Two-Photon Absorption Spectra in Metal Halide Perovskites. Proceeding to *Nat. Commun.* **2019**
(Paper of the supervised master project)
7. Brenes, R.; **Guo, D.**; Osherov, A.; Noel, N. K.; Eames, C.; Hutter, E. M.; Pathak, S. K.; Niroui, F.; Friend, R. H.; Islam, M. S.; et al. Metal Halide Perovskite Polycrystalline Films Exhibiting Properties of Single Crystals. *Joule* **2017**, *1*, 155–167.
(Cover of the inaugural issue of Joule)
8. Wei, H.; Desantis, D.; Wei, W.; Deng, Y.; **Guo, D.**; Savenije, T. J.; Cao, L.; Huang, J. Dopant Compensation in Alloyed $\text{CH}_3\text{NH}_3\text{PbBr}_{3-x}\text{Cl}_x$ Perovskite Single Crystals for Gamma-Ray Spectroscopy. *Nat. Mater.* **2017**, *16*, 826–833.
9. Levine, I.; Gupta, S.; Bera, A.; Ceratti, D.; Hodes, G.; Cahen, D.; **Guo, D.**; Savenije,

- T. J.; Ávila, J.; Bolink, H. J.; et al. Can We Use Time-Resolved Measurements to Get Steady-State Transport Data for Halide Perovskites? *J. Appl. Phys.* **2018**, *124*.
10. Lin, Y.; Liu, Y.; Li, t.; Dai, J.; **Guo, D.**; Fang, Y.; Gruverman, A.; Zeng, X.; Savenije, T. J.; Huang, J. Lateral Homojunction Perovskite Solar Cells via Metal Ion Doping. Submitted. **2019**

Conference papers

1. Predicting the Maximum Open Circuit Voltage of Perovskite Solar Cells from Time-Resolved Measurements. *HOPV, May 12-15, 2019 Rome, Italy*. Poster presentation.
2. How Charge Dynamics Change in Mixed Halide Perovskites on Light Soaking. *ABXPV, February 27-28, 2018 Rennes, France*. Oral presentation.
3. How the Dynamics of Charge-Carriers Change on Light Soaking in Mixed Halide Perovskites. *Chains, December 3-5, 2018 Veldhoven, the Netherlands*. Poster presentation. Poster presentation.
4. Reduction of non-Radiative Decay in Metal Halide Perovskites by light Soaking in Humid Air. *FOM, January 23-24, 2018 Veldhoven, the Netherlands*. Poster presentation.
5. Light-Induced Charge Carrier Dynamics in CH₃NH₃PbBr₃ Single Crystals. *FOM, December 17-18, 2017 Veldhoven, the Netherlands*. Poster presentation.
6. Structure Dependent Charge Carrier Dynamics in CH₃NH₃PbBr₃ Single Crystals. *ABXPV, March 1-2, 2017 Valencia, Spain*. Poster presentation.
7. Orientation Dependent Carrier Mobility in Perovskite Single Crystals. *HOPV, June 29 - July 1, 2016 Swansea, United Kingdom*. Poster presentation.